

**Optical Absorption and Photovoltaic Properties of CdSe
Quantum Dots on TiO₂ Electrodes with Different
Morphology**

WITON YINDEESUK

**DEPARTMENT OF ENGINEERING SCIENCE
THE UNIVERSITY OF ELECTRO-COMMUNICATIONS
MARCH 2014**

**Optical Absorption and Photovoltaic Properties of CdSe
Quantum Dots on TiO₂ Electrodes with Different
Morphology**

by

WITON YINDEESUK

**A Dissertation Submitted in Partial Fulfillment of the
Requirements for the Degree of
DOCTOR OF ENGINEERING**

at

**THE UNIVERSITY OF ELECTRO-COMMUNICATIONS
MARCH 2014**

**Optical Absorption and Photovoltaic Properties of CdSe
Quantum Dots on TiO₂ Electrodes with Different
Morphology**

APPROVED BY THE SUPERVISORY COMMITTEE:

CHAIRPERSON: ASSOC. PROF. Qing Shen

MEMBER: PROF. Taro Toyoda

MEMBER: PROF. Shigeo Hayashi

MEMBER: PROF. Kohji Abe

MEMBER: PROF. Tsuyoshi Okuno

Copyright

By

WITON YINDEESUK

2014

表面形態が異なる TiO₂ 電極に吸着した CdSe 量子ドットの 光 吸収と光電変換特性

近年半導体量子ドット (semiconductor quantum dot, 略して QD) は、大きな光吸収係数と双極子モーメントを有し、さらに多重励起子生成効果を示すため、次世代の太陽電池における高効率増感剤の一つとして注目されている。増感剤はナノ粒子酸化物(今回は TiO₂ を適用)電極に吸着され、太陽電池の作用電極基板として使用される。ここで、ナノ粒子酸化物電極には種々のモルフォロジーを持つものが適用されている。本研究では、数 10 ナノメートルの粒径を有する TiO₂ ナノ粒子集合体電極基板と、フォトニック特性を示す逆オパール (蜂の巣) 構造を有する TiO₂ 電極基板を対象とし、CdSe QD を吸着した 2 つの電極基板系の光吸収スペクトル特性評価、光電流量子効率スペクトル特性評価、さらに太陽電池デバイスを形成し光電変換特性評価を行った。CdSe QD の吸着には Cd⁺ と Se⁻ イオンを交互に吸着する successive ionic layer adsorption and reaction (略して SILAR) 法を適用した。この手法は従来のイオン系が混合した溶液中で行う吸着法 (CBD 法) に比べて、良質で粒径均一性の良い QD が形成出来ることで知られている。ここで、対象とする基板電極系は半透明・不透明であるため、光吸収測定にはこれらに有効な光音響法を適用した。光電流量子効率は短絡電流の波長分散から、光電変換は疑似太陽光を適用する既存のソーラーシミュレータにより評価を行った。

光吸収評価から、CdSe QD の成長と量子閉じ込め効果の出現が判明した。光吸収結果に対して有効質量近似を適用し、交互のイオン吸着回数(3-14 回)に対する CdSe QD の粒径変化を求めた。その結果、ナノ粒子集合体電極基板と逆オパール構造電極基板では粒径の大きさと変化は一致し、5nm から 12nm まで単調に増加し、結晶成長は電極基板のモルフォロジーには依存しないという結果が得られた。一方光透過率の測定を行った結果、ナノ粒子集合体電極基板では逆オパール電極に比べて 3 倍ほど CdSe QD の吸着速度が速いことが判明した。一つの可能性として、ナノ粒子集合体電極基板と逆オパール構造電極基板における TiO₂ の結晶面方位が異なり、QD 吸着速度が異なることが考えられ、今後は基板における各結晶面方位の状態密度の評価が重要となる。続いて光吸収におけるバンドギャップ以下の光吸収領域の評価から、ナノ粒子集合体電極基板吸着に

比べ逆オパール構造電極基板吸着ではより格子乱れが多いことが判明した。逆オパール構造電極基板作製における、より一層の詳細な条件の検討が必要となる。

光電流量子効率測定から、 TiO_2 の光吸収端下の領域（可視領域）で光電流が観測された。この結果から、CdSe QD の分光増感機能の発現が判明した。CdSe QD の粒径の増加に伴い、極大値は次第に低エネルギー側にシフトした。ナノ粒子集合体電極基板吸着に比べ逆オパール構造電極基板吸着では光電流量子効率の大きさはおよそ 1/2 で、吸着表面積の違いと吸着条件の違いが要因の一つと考えられる。

光電変換特性評価から、いずれの系でも短絡電流は CdSe QD の成長に伴い増加する。しかし、ナノ粒子集合体電極基板吸着に比べ逆オパール構造電極基板吸着では、短絡電流の大きさはおよそ 1/2 で、光電流量子効率の違いに対応している。一方開放電圧の値は両系とも CdSe QD の成長には依存せずほぼ一定値であるが、逆オパール構造電極基板吸着系ではナノ粒子集合体電極基板吸着系に比べて、およそ 0.1V ほど高いことが判明した。この事実は、逆オパール構造電極の価電子帯の頂上が、ナノ粒子集合体電極に比べてエネルギー的に高い位置にあることを示唆している。今後は光電子分光法等を適用しナノ粒子酸化物基板の電子構造の検討が必要となる。形状因子に関しては、ナノ粒子集合体電極基板吸着と逆オパール構造電極基板吸着では大きな違いは見られなかった。以上の光電変換特性評価から、逆オパール構造電極基板吸着系での最大光電変換効率は 1.3%、ナノ粒子集合体電極基板吸着系では 2.7% が得られた。さらに、光電変換効率はデバイスの直列抵抗成分と並列抵抗成分が大きく関与するため、これらの抵抗成分の検討を行った。その結果、逆オパール構造電極基板吸着系ではナノ粒子集合体電極基板吸着系に比べ、直列抵抗成分はおよそ 3 倍大きく、並列抵抗成分はおよそ 1.5 倍程度大きいことが判明した。光電変換特性では直列抵抗成分の減少と並列抵抗成分の増大を図ることが光電変換効率の向上につながるため、電極基板、特に逆オパール構造電極基板吸着系における CdSe QD との間の界面準位の評価を行い、界面準位の減少を図り直列抵抗成分の減少と並列抵抗成分の増大につなげることが重要となる。

Optical Absorption and Photovoltaic properties of CdSe Quantum Dots on TiO₂ Electrodes with Different Morphology

ABSTRACT

Semiconductor quantum dots (QDs) have attracted significant interest in sensitized solar cells. The semiconductor QDs exploit as a sensitizer and have several advantages such as quantum confinement, large extinction coefficient, and multiple exciton generation. A successive ionic layer adsorption and reaction (SILAR) method is an ion-by-ion growth of thin films and provides high coverage of the electrode. Therefore, the SILAR method is a fascinating process for preparation of CdSe QDs. In addition, an inverse opal TiO₂ (IO-TiO₂) film have a honeycomb structure with large interconnected pores that lead to a better infiltration of electrolyte in a photoelectrochemical cell.

To investigate the effect of the electrode morphology, we have studied the optical absorption properties of CdSe QDs adsorbed on IO-TiO₂ and nanoparticulate TiO₂ (NP-TiO₂) electrodes for comparison, including the photovoltaic properties of CdSe QDs sensitized solar cells (QDSSCs). CdSe QDs were grown on an IO-TiO₂ and NP-TiO₂ surface by a SILAR method for different cycles. A sandwich structure solar cell was consisted of Cu₂S on brass as a counter electrode and a polysulfide (S/S²⁻) redox system as the electrolyte.

The average diameter of the QDs was estimated by applying an effective mass approximation to the optical absorption spectra. Linear dependence of the size of the QDs with increasing number of cycles was confirmed by a redshift in the optical absorption spectrum. The average diameter of the CdSe QDs on the IO-TiO₂ electrodes was similar to that on the NP-TiO₂ ones, indicating that growth is independent of morphology. However, there were more CdSe QDs on the NP-TiO₂ electrodes than on the IO-TiO₂ ones, indicating that there were different amounts of active sites on each type of electrode. In addition, the

Urbach parameter (as a guide of disordered states) of the exponential optical absorption tail was also estimated from the optical absorption spectrum. The Urbach parameter of CdSe QDs on IO-TiO₂ electrodes was higher than that on NP-TiO₂ ones, indicating that CdSe QDs on IO-TiO₂ electrodes are more disordered states than those on NP-TiO₂ electrodes. The Urbach parameter decreases in both cases with the increase of SILAR cycles, and it tended to move toward a constant value. The incident photon-to-current conversion efficiency (IPCE) and photovoltaic properties of sandwich structure solar cells were studied under an illumination of air mass (AM) 1.5 using Cu₂S on brass as a counter electrode and a polysulfide (S/S²⁻) redox system. The photosensitization of CdSe QDs on TiO₂ electrodes in the visible region could be observed in both electrode morphologies. The IPCE spectra of both IO-TiO₂ and NP-TiO₂ cells were shifted to low photon energy region because a size of CdSe QDs on TiO₂ grows with increasing SILAR cycle. The lower IPCE in IO-TiO₂ cell comparison with NP-TiO₂ cell could be because of a fewer adsorption of Cd²⁺ ions, and smaller surface area. The maximum photovoltaic conversion efficiency (η) of CdSe QDs on IO-TiO₂ was 1.3% and that of CdSe QDs on NP-TiO₂ was 2.7%, prepared with 9 cycles. Lower η of CdSe QDs on IO-TiO₂ than that on NP-TiO₂ was possibly because of the lower adsorption of Cd²⁺ ions, a larger amount of surface states, and lower TiO₂ surface area. In this study, the series resistance (R_s) could assume that depends on the charge transfer resistance in TiO₂ film adsorbed with CdSe QDs. The estimated R_s of IO-TiO₂ cell is larger than NP-TiO₂ one. A possible reason for the different R_s , the QDs on IO-TiO₂ has fewer amounts than the QDs on NP-TiO₂, which result in the QDs on IO-TiO₂ has fewer injected electrons than the QDs on NP-TiO₂. These results indicate that the CdSe SILAR cycle is the important condition that affects the photovoltaic properties of CdSe QDSSCs.

Contents

Japanese abstract	i
Abstract	iii
Contents	v
List of figures	vii
List of tables	x
1 Introduction	1
1.1 Introduction	1
1.1.1 Background	1
1.1.2 Purposes	7
1.1.3 Brief outline of the thesis	8
1.2 Basics of TiO ₂	9
1.2.1 Crystal Structural of TiO ₂	9
1.2.2 Applications of TiO ₂	10
1.2.3 TiO ₂ nanomaterials	12
1.2.4 Template-based synthesis	13
1.3 Semiconductor quantum dots as solar cell sensitizers	15
1.3.1 Cadmium selenide	19
1.3.2 Quantum confinement effect	20
1.3.3 Hot carrier and multiple exciton generation	23
2 Experimental procedures	30
2.1 Sample preparation	30
2.1.1 Inverse opal titanium dioxide	30
2.1.2 Adsorption of CdSe QDs on inverse opal TiO ₂	32
2.2 Characterization	34
2.2.1 Scanning electron microscopy	34
2.2.2 X-ray diffraction spectrometry	35
2.2.3 Photoacoustic spectroscopy	37

2.2.4 Incident photon to current efficiency spectroscopy	43
2.2.5 Power conversion efficiency measurement	45
3 Optical absorption characterization of CdSe QD on TiO₂	49
3.1 Introduction	49
3.2 Experimental	51
3.3 Results and discussion	54
3.4 Conclusions	60
4 Photovoltaic properties of CdSe QD on TiO₂	64
4.1 Introduction	64
4.2 Experimental	66
4.3 Results and discussion	68
4.4 Conclusions	75
5 Summary	78
Appendix 1 PbS/CdS quantum dot sensitized solar cell	80
Publications and conference visits	88
Acknowledgments	90
Biography	91

List of figures

Figure 1.1	Basic operation of solar cells.	3
Figure 1.2	Classification of solar cells.	5
Figure 1.3	Crystal structures of rutile, anatase and brookite polymorphs of TiO ₂ .	10
Figure 1.4	Summary of synthesis methods of TiO ₂ nanomaterials.	13
Figure 1.5	Artistic depiction of the materials which make up a quantum dot sensitized solar cell.	16
Figure 1.6	A diagram of the energetics which drive electron and hole transport in a quantum dot sensitized solar cell.	17
Figure 1.7	Band edges position of several semiconductors in contact with aqueous electrolyte at pH 1. The energy scale is indicated in electron volts using either the normal hydrogen electrode (NHE) or the vacuum level as a reference.	18
Figure 1.8	Solid state structure of CdSe. (a) Wurtzite structure (b) hexagonal structure.	21
Figure 1.9	Quantum confinement effect on electron energy levels.	22
Figure 1.10	Representation of multiple exciton generation (E_1 relating to first excitation energy in quantum dot, likewise E_g relating to energy band gap of bulk semiconductor).	25
Figure 2.1	Schematic procedure of the fabrication inverse opal TiO ₂ (a) template preparation, (b) filling the template with TiO ₂ (c) calcination of template and annealing of TiO ₂ .	31
Figure 2.2	Flowchart of chemical solution preparation for CdSe adsorption.	33
Figure 2.3	Drawing of SILAR deposition for CdSe.	34
Figure 2.4	Schematic of the SEM column which focuses the electrons emitted from a heated tungsten filament into a small nanometer sized spot.	35
Figure 2.5	Bragg diffraction.	36

Figure 2.6	Idealized photoacoustic cell.	39
Figure 2.7	Schematic diagram of photoacoustic spectroscopy.	42
Figure 2.8	Typical PA spectrum of carbon black.	43
Figure 2.9	Incident photon to current efficiency measurement setup.	45
Figure 2.10	Typical Current-Voltage characteristic curve of solar.	46
Figure 2.11	Air mass (a) optical path length of sunlight through Earth's atmosphere (b) solar irradiance spectrum.	47
Figure 3.1	Scanning electron microscopy (SEM) image of (a) IO-TiO ₂ and (b) NP-TiO ₂ .	52
Figure 3.2	PA spectra of CdSe QDs adsorbed on (a) IO-TiO ₂ and (b) NP-TiO ₂ electrodes with different numbers of CdSe SILAR cycles.	53
Figure 3.3	Tauc plots of CdSe QDs adsorbed on (a) IO-TiO ₂ and (b) NP-TiO ₂ .	55
Figure 3.4	Dependence of the average diameter of CdSe QDs adsorbed on IO-TiO ₂ and NP-TiO ₂ electrodes on the number of CdSe SILAR cycles.	56
Figure 3.5	Dependence of width of the exponential tail of CdSe QDs adsorbed on IO-TiO ₂ and NP-TiO ₂ electrodes on the number of SILAR cycles.	58
Figure 4.1	IPCE spectra of CdSe QDs adsorbed on IO-TiO ₂ (a) and NP-TiO ₂ (b) electrodes with different CdSe SILAR cycles.	69
Figure 4.2	J-V curves of CdSe QDSSCs with different CdSe SILAR cycles (a) IO-TiO ₂ (b) NP-TiO ₂ .	70
Figure 4.3	Equivalent circuit of a solar cell.	72
Figure 4.4	Dependence of the R _{sh} (a) and R _s (b) on CdSe SILAR cycle.	74
Figure A.1	Photoacoustic spectroscopy of PbS and CdS quantum dot on TiO ₂ .	81

Figure A.2	Dependence of the energy gap and the average diameter of PbS and CdS QDs adsorbed on TiO ₂ electrodes on the number of SILAR cycles.	81
Figure A.3	Incident photon current efficiency spectra of PbS/CdS sensitized solar cell.	82
Figure A.4	Current density and voltage curve of PbS/CdS sensitized solar cell.	83
Figure A.5	Photovoltaic properties of PbS/CdS sensitized solar cell (a) Efficiency (b) Short circuit current density (c) Open circuit voltage (d) Fill factor	85

List of tables

Table 1.1	List of some properties of CdSe (Wurtzite structure).	19
Table 2.1	Rosencwaig-Gersho special case for thermally thick samples.	42
Table 4.1	Photovoltaic properties of CdSe QDs adsorbed on TiO ₂ electrodes with different CdSe SILAR cycles.	75
Table A.1	Photovoltaic properties of PbS and CdS QDs adsorbed on TiO ₂ electrodes with different SILAR cycles.	86



Introduction

1.1 Introduction

1.1.1 Background

At the present time, most of the world's consumption of energy is based on coal, oil and natural gas. However, the use of this fossil fuel could result in pollution. Burning coal produces sulphur dioxide, an acidic gas that contributes to the formation of acid rain and burning any fossil fuel produces carbon dioxide, which leads to the "greenhouse effect", warming the Earth. Greenhouse effects melt glaciers at the arctic regions and will cause not only an increase of sea level but also other atmospheric phenomena that could ultimately result in significant ecological problems for the earth. There has been an enormous increase in the demand for energy since the middle of the last century as a result of industrial development and population growth. In the 1970s, "Middle east oil crisis" panicked world due to petroleum shortage and high gasoline prices. The supply shortage and environmental problems have attracted our interest to find another energy source beyond fossil fuel. While there are already alternative energy sources, there are tradeoffs in the use of many of these sources. For example, nuclear power is a powerful and long-term alternative energy source but radioactive materials from nuclear power plants are extremely hazardous, and the disposal of the nuclear waste after power generation is a complicated environmental issue. These concerns became even more visible after the recent earthquake in Japan and the resulting tsunami crippled the nuclear

INTRODUCTION

power plants. Radioactive materials from the reactor chambers contaminated not only the soil and sea water but also the Earth's atmosphere. Nuclear energy, which was considered to be one of the best candidates as an alternative energy source, is now being reconsidered as a safe and stable energy source. Therefore, renewable energy sources which are generated from natural resources such as sunlight, wind, water, and so forth have emerged as clean alternative energy sources for the future. Solar energy is an alternative renewable energy without any environmental damage. The following is several advantages of solar energy,

- Inexhaustible fuel source

- No pollution (environmentally friendly)

- Readily availability (in a sunny enough climate)

- Often an excellent supplement to other renewable sources

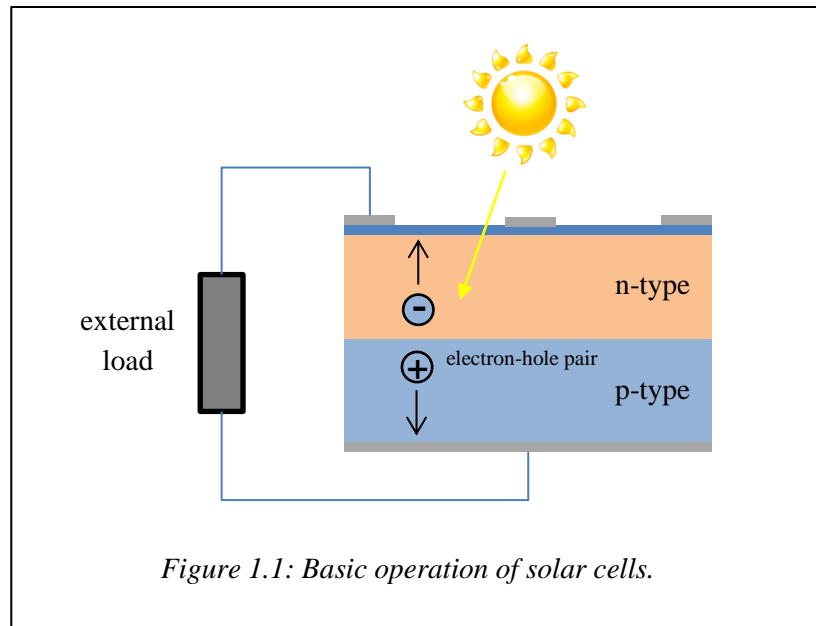
- Versatile, is used for powering items as diverse as solar cars and satellites

Therefore, a significant number of researchers have been focused on developing high efficiency, stable and low cost solar cells using various materials for a long time.

Photovoltaic effect

Photovoltaic effect is the basic process through which a solar cell converts solar radiation into electricity, which was first observed by Henri Becquerel [1] in 1839. He generated electricity between two electrodes attached to a liquid system upon irradiating light onto this system. The next significant photovoltaic development arose from the first demonstration of photovoltaic effects in selenium (solid-state system) by Adam and Day [2] in 1876. They observed the photovoltaic effect by illuminating a junction between the platinum and selenium. The next significant step forward came with the work of Fritts [3] in 1883. He was able to prepare a selenium solar cell, the first "thin-film" photovoltaic

INTRODUCTION



devices, consisted of thin selenium films which adhered to one metal plate (e.g. brass) and gold leaf.

Fundamentally, there are three basic requirements for the photovoltaic effect (shown in Fig. 1.1). First, upon irradiation, light or photon should be absorbed creating electron-hole pairs. Then these electron-hole pairs should be separated so that their recombination is inhibited. In the end, these electrons and holes should be collected separately by each of collecting electrodes. Anode is the electrode collecting electrons and cathode is electrode collecting holes. Thus, current can be induced to flow in an external circuit.

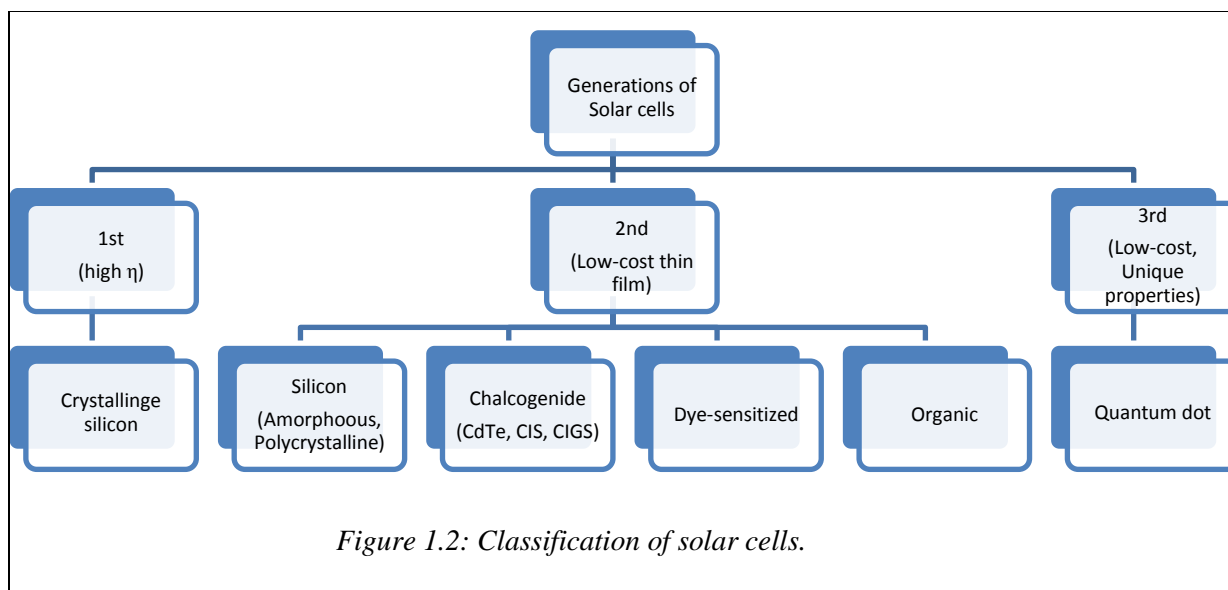
Classification of solar cells

Generally, solar cell technologies are classified into three generation (shown in Fig. 1.2) according to Martin Green from University of New South Wales (UNSW). The first generation solar cells is aimed to obtain high efficiency and mainly based on crystalline silicon, which is currently used worldwide with the best laboratory energy

INTRODUCTION

conversion efficiency achieved ~ 25%. The theoretical limit of the solar cell using single junction is calculated by Shockley and Queisser [4] to be about 31%, limited to the thermalization loss of hot carriers (heat loss of the excess kinetic energy of hot photogenerated carriers created by the absorption of photon with high energy) and no absorption of photon with energy less than band gap. In fact to synthesis such high purity silicon, it requires high cost, energy-intensive high-temperature (more than 1000 °C) and high-vacuum processes. The cost of silicon solar cell may be reduced by thin film technology (known as second generation solar cells), in which thin film silicon solar cells are mainly deposited by chemical vapour deposition (CVD) from silane gas (SiH_4) and hydrogen in 200 °C. This process produces amorphous silicon (no crystalline orientation) with lower conversion efficiency. The best laboratory efficiencies could be achieved ~20% for polycrystalline silicon and ~15% for amorphous silicon. The other second generation solar cells include the chalcogenide material, such as cadmium telluride (CdTe), copper indium sulfide (CIS) and copper indium gallium selenide (CIGS). These materials are applied in a thin film to a supporting substrate such as glass or ceramics reducing material mass and therefore costs. These technologies, particularly CIGS-CIS, DSC and CdTe offer significantly cheaper production costs. Dye-sensitized solar cells (DSSCs) and organic solar cells are the advanced thin film photovoltaic with low cost and simple production based on photoelectrochemical method. So far, the energy conversion efficiency of DSSCs could exceed 11% [5]. Third generation solar cells aim to enhance the performance of second generation (thin-film technologies) while maintaining very low production costs. Current research purposes to obtain the energy conversion efficiencies of 30-60% while retaining low cost materials and manufacturing techniques. This may be achieved by exploiting the

INTRODUCTION



hot photogenerated carriers in quantum dots (QD) to produce higher photovoltages or higher photocurrents. The former is based on miniband transport and collection of hot carriers in QD array photoelectrodes before their relaxation to the band edges through photon emission and heat loss consequently. The latter is based on generation and collection additional electron-hole pairs by utilizing hot carriers in QD solar cells through enhanced impact ionization processes. Further, the scope in this study concentrates on the DSSCs and the application of semiconductor QD (i.e. CdSe QD) as photosensitizer replacing dye.

Dye-sensitized solar cells (DSSCs)

Dye Sensitized TiO₂ Nanocrystalline solar cells (DSSCs) has attracted much attention because they are generally made from inexpensive and nontoxic components, and can be designed in a diversity of colors and transparencies. Since the pioneering work of dye-sensitized nanocrystalline TiO₂ by Grätzel and co-workers in 1991 [6], efforts have been made to improve the performance of DSSCs. However, the development of DSSCs has been slow over the last ten years, with the highest record of 12% ever

INTRODUCTION

reported [7]. In this cell, the use of dye molecules as photosensitizers, nanostructured TiO_2 as the electron transport layer and I^-/I_3^- redox couple as hole transport layer dramatically improve light harvesting efficiency. Based on the DSSC's structure, quantum dot (QDs) was introduced as a replacement of dye to its excellent optoelectronic properties [8]. Quantum dot-sensitized solar cells (QDSSCs) are interesting photovoltaic devices because quantum dots show some benefits, such as quantum high extinction coefficient, quantum confinement effect and so on. Particularly, the multiple exciton generation (MEG) of QD solar cells can theoretically give about 44% of conversion efficiency, higher than Shockley–Queisser efficiency limit. Due to the quantum confinement effect, the bandgap of semiconductor nanoparticles and, hence its optical absorption, can be modulated over a wide spectral range by controlling their size to match the distribution of solar light. Moreover, semiconductor nanocrystals have robust inorganic nature so these particles are more stable against photodegradation than the usual organic dyes. With these advances, researchers were able to fabricate solar cell devices achieving efficiency up to 7% in QD related solar cells [9].

The relatively low efficiency obtained in DSSC is assigned to the poor penetration of material into the thick TiO_2 film, and the detachment of hole transport layer from TiO_2 electrode [10]. In order to address the penetration of both sensitizers and redox couples, a novel approach has been proposed using mesoporous inverse opal titania starting from self-organizing systems, such as opal of polystyrene latex, as template. This inverse opal (volumetric inverse of opal) titania has large interconnected pores lead to better infiltration. In addition, it also exhibits photonic band gap (frequency range that will not allow the propagation of particular wavelengths because of multiple Bragg reflection), which depends on the filling fraction of TiO_2 in the inverse opal structure. On the red-edge of the photonic band gap, the photon will be localized in high refractive index layer of sensitized inverse opal TiO_2 thus could significantly enhance the sensitizer absorption,

INTRODUCTION

especially in the edge of optical absorption where the sensitizer absorbs weakly solar light [2].

Quantum dot-sensitized solar cells (QDSSCs) may improve the efficiency by both materials development and the progress in understanding the cell mechanisms. Materials development involves (1) the emergence of absorber such as CdSe, CdS, PbS and Sb₂S₃, which extend the light absorption range from the visible to the near-infrared region [11], (2) the improvement of QD synthesis and loading using successive ionic layer adsorption and reaction (SILAR) [12], chemical bath deposition (CBD) [13], monodisperse QDs with molecular linkers [14], and direct adsorption (DA) [15], (3) different morphology of wide metal oxide semiconductors [16], (4) new counter electrode [17], and (5) the improvement of redox couple electrolyte [18]. In addition, the basic understanding of the cell mechanisms includes (1) the existence of several electron injection paths [19], (2) fast hole extraction relative to electron recombination [20], (3) charge accumulation in QDs layer [21], (4) the effect of surface modifications of both the QDs and the metal oxide [22].

1.1.2 Purposes

Based on the background mentioned above, this study mainly focuses on the study and application of inverse opal structured electrode and CdSe QD replacing nanocrystalline electrode and dye sensitizer, respectively. CdSe is selected among the other semiconductors due to the possible electron injection from CdSe to TiO₂ and its well-known properties. The purposes of this study are as follows:

1. Synthesis of three dimensional inverse opal TiO₂ and characterize its physical properties.
2. Adsorbing of CdSe quantum dots on inverse opal TiO₂ and characterize the photosensitization of inverse opal TiO₂ with CdSe QDs

INTRODUCTION

3. Investigation on the photovoltaic properties of CdSe QD-adsorbed inverse opal TiO₂ and introduce suggestions for better solar cells.

1.1.3 Brief outline of the thesis

This thesis consists of a total of 5 chapters. The first chapter shows the introduction to this field, purpose and outline of this thesis. Moreover, it provides a general overview of some of the concepts that are needed for reading this thesis, such as background of TiO₂ and related theories of semiconductor quantum dots. It is by no means a complete overview, thus many references are necessary to provide the comprehensive background to this field.

Chapter 2 explains the experimental procedures, i.e. sample preparations and used characterization techniques. The former includes the inverse opal TiO₂ preparation and the method to adsorb the CdSe QD in situ on inverse opal TiO₂. The latter includes the used technique to characterize its structure, morphology, optical absorption, photocurrent, photovoltaic properties.

Chapter 3 shows the adsorption of CdSe in situ on inverse opal TiO₂ and its effect on the morphology. Photoabsorption of inverse opal TiO₂ with CdSe QDs is studied by characterizing its optical absorption by photoacoustic spectroscopy as a function of SILAR cycles. Moreover, size of semiconductor nanoparticle is calculated from the effective mass approximation. Urbach parameter is determined from the optical absorption band edge to consider defects of TiO₂ adsorbed with CdSe QDs.

Chapter 4 contains characterization of the photovoltaic properties of CdSe QD-sensitized inverse opal TiO₂ in solar cell application. The typical photovoltaic properties will be compared with those of CdSe QD-sensitized nanoparticulate TiO₂ solar cells. Metal sulfide electrode is then used as active counter electrode against the polysulfide

INTRODUCTION

electrolyte, usually used as redox couple in QD-sensitized solar cells. Further improvements are suggested resulting in efficient QD-sensitized solar cells.

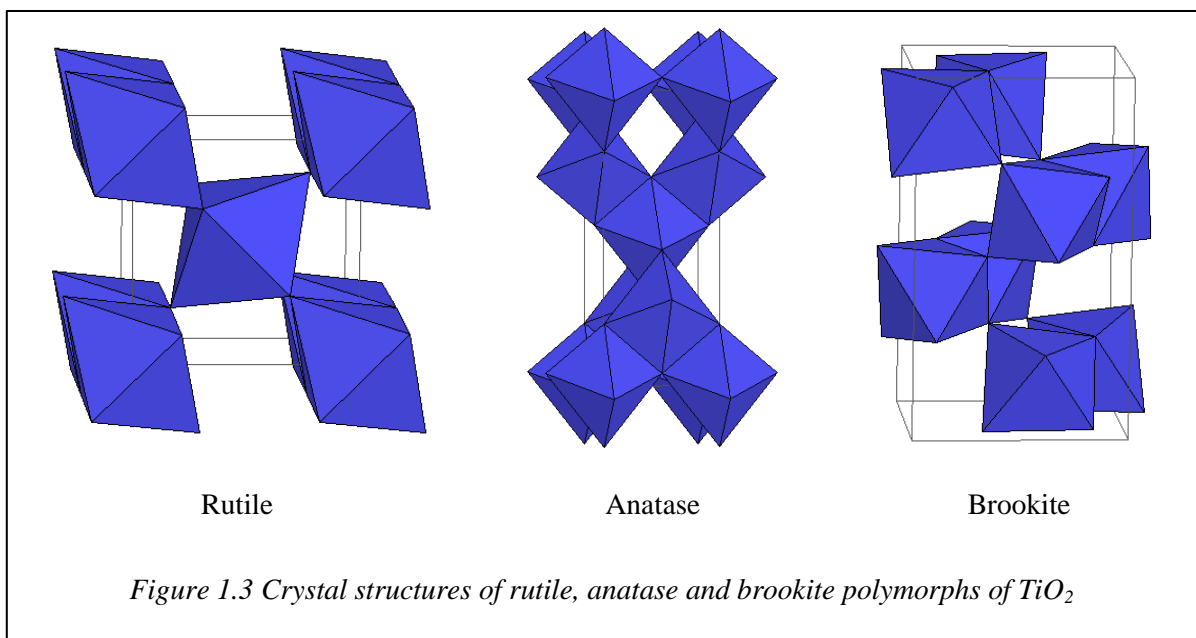
Finally, chapter 5 summarizes the whole results in this study. In addition, an appendix is added in this thesis, which investigates co-sensitized solar cell. PbS/CdS quantum dot sensitized solar cell was studied by measuring optical absorption, photocurrent, and photovoltaic properties. The co-sensitized solar cell can have more conversion efficiency than solar cells with only single sensitizer.

1.2 Basics of TiO₂

1.2.1 Crystal Structural of TiO₂

Titanium dioxide occurs in nature in three mineral forms: rutile, anatase and brookite, additionally two high pressure forms, the monoclinic baddeleyite form and the orthorhombic α -PbO₂ form have been found at the Ries crater in Bavaria [23]. Rutile is the most common form in nature and the most stable polymorph among the three modifications. Anatase and brookite both convert to rutile upon heating. Rutile, anatase and brookite all contain six coordinated titanium in the form of TiO₆ octahedral, but with different stacking-up topology. The crystal structures of the three polymorphs were illustrated in Fig. 1.3. Both rutile and anatase crystallize in tetragonal system. The two crystal structures differ in the distortion of each octahedron and by the assembly pattern of the octahedra chains. In rutile, the octahedron shows a slight orthorhombic distortion, while the octahedron of anatase is significantly distorted so that its symmetry is lower than orthorhombic. The name of anatase roots from the Greek “anatisis” which means

INTRODUCTION



"extension", indicating the vertical axis of the crystals being longer than that in rutile [24]. Brookite crystallizes in the orthorhombic system. Brookite occurs rarely compared to the anatase and rutile forms of titanium dioxide. Because brookite shows no photocatalytic activity, it attracts the least research interest. These differences in lattice structures cause difference mass densities and electronic structures as well as other chemical and physical properties.

1.2.2 Applications of TiO₂

TiO₂ is one of the top fifty chemicals produced worldwide. Since its commercial production in the early twentieth century, titanium dioxide has been widely used as a pigment in sunscreens, paints, ointments, toothpaste, etc. It provides for maximum whiteness and opacity [25]. It does so more effectively than any other white pigment. These unique properties are derived from the refractive index of titanium dioxide which is the highest among any material known to man, even greater than diamond.

INTRODUCTION

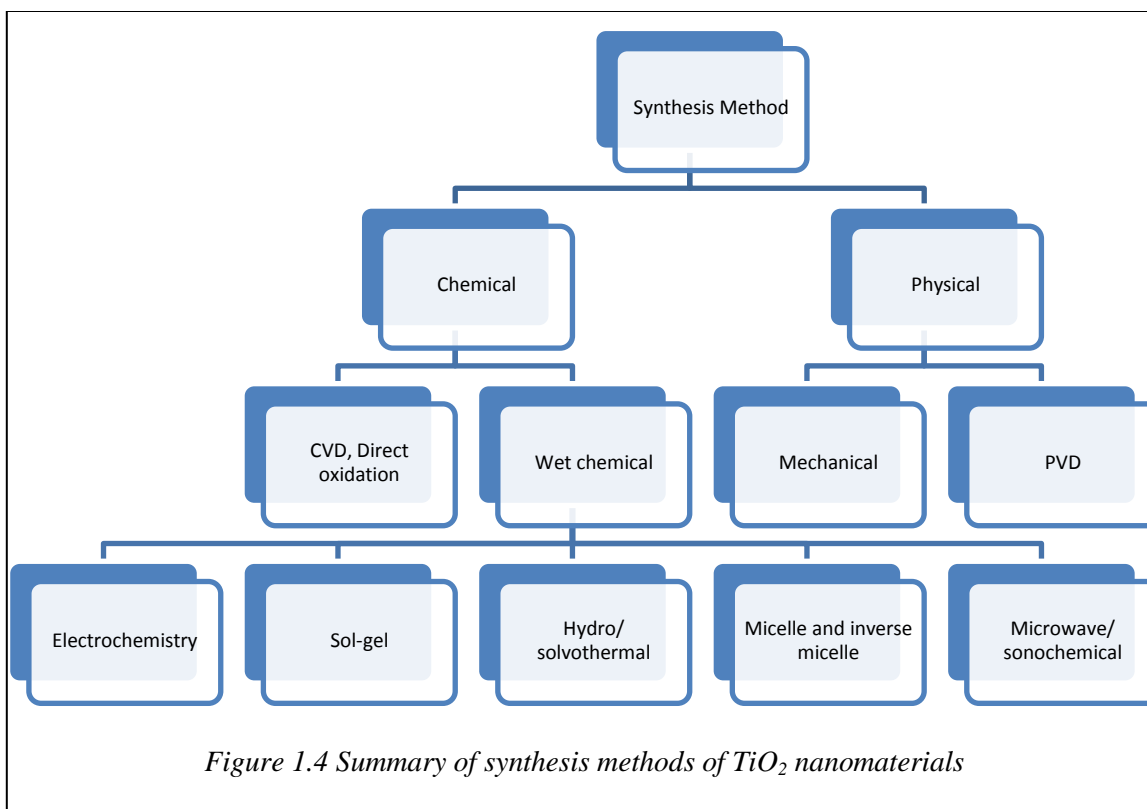
TiO₂ is also a potent photocatalyst that can break down almost any organic compound when exposed to sunlight [26]. A wide range of environmentally beneficial products utilizing TiO₂'s reactivity are being developed including self-cleaning fabrics, auto body finishes, and ceramic tiles. Also in development is a paving stone that uses the catalytic properties of TiO₂ to remove nitrogen oxide from the air, breaking it down into more environmentally benign substances that can then be washed away by rainfall. It remains to be seen, however, whether the formation of undesirable intermediate products during these processes outweighs the benefits offered by TiO₂'s photocatalytic properties.

As the most promising photocatalyst, TiO₂ materials are expected to play an important role in helping solve many serious environmental and pollution challenges. The general scheme for the photocatalytic destruction of organic compounds involves the excitation of the semiconductor by irradiation with suprabandgap photons, and continues through surface redox reactions. One of the applications is photovoltaic application. Photovoltaics based on TiO₂ nanocrystalline electrodes have been widely studied [27]. At the heart of the system is a nanocrystalline mesoporous TiO₂ film with a monolayer of the charge transfer dye attached to its surface. The film is placed in contact with a redox electrolyte or an organic hole conductor. Photoexcitation of the dye injects an electron into the conduction band of TiO₂. The electron can be conducted to the outer circuit to drive the load and make electric power. The original state of the dye is subsequently restored by electron donation from the electrolyte, usually an organic solvent containing a redox system, such as the iodide/triiodide couple. The regeneration of the sensitizer by iodide prevents the recapture of the conduction band electron by the oxidized dye. The iodide is regenerated in turn by the reduction of triiodide at the counter electrode, with the circuit being completed via electron migration through the external load. The voltage generated under illumination corresponds to the difference between the Fermi level of TiO₂ and the redox potential of the electrolyte. Overall, the device generates electric power from light without suffering any permanent chemical transformation.

INTRODUCTION

1.2.3 TiO₂ nanomaterials

When the dimension of matter is brought down to nanometer scale, many of its features would easily change and have many unique features both different from macro-matters and single atoms due to the quantum effect, regional confinement of matter, and ultra-high surface area or interface effects [28]. The final objective of nanotechnology is to produce products of special functions with new physical and chemical features by making atoms, molecules and matters presenting their features directly in the length of a nanometer such as: the strength of ten times of iron could be very light, all the information in a library could be stored in a chip the size of a sugar cube, and tumors the sizes of only several cells can be detected. Titanium dioxide's photocatalytic characteristics are greatly enhanced due to the advent of nanotechnology [29]. At the nano-scale, not only the surface area of titanium dioxide particle increases dramatically but also it exhibits other effects on optical properties and size quantization. An enhanced rate in photocatalytic reaction is observed as the redox potential increases and the size decreases [30]. The same effect also applies to the photovoltaic application, which also utilizes the photo-generated charge carriers. Due to its potent performance in photocatalysis and photovoltaic application, tremendous interests and efforts have been devoted to research on TiO₂ nanomaterials in terms of synthesis and modification, property characterization, fundamental mechanism investigation, theoretical calculation, and application. The TiO₂ nanomaterials synthesis methods are summarized as a chart in Fig. 1.4. The physical methods mainly include mechanical milling and physical vapor deposition. The chemical routes especially wet-chemical routes are extensively used to synthesize TiO₂ materials. It can be further categorized into sol-gel,



hydrothermal/solvothermal, micelle/inverse micelle, sonochemical/microwave, and electrochemical techniques. These techniques are mainly based on the hydrolysis or solvolysis between titanium-containing precursors and the solvent or chelating agents with or without external assistance such as elevated temperature and pressure in hydrothermal reactor, surfactant in micelle method, microwave or sonar energy to facilitate or direct the crystal growth.

1.2.4 Template-based synthesis

In a general way, “template” is defined as a central structure within which a network forms in such a way that removal of the template creates a filled cavity with morphological and/or stereochemical features related to those of template. A method termed “template synthesis” entails the preparation of a variety of micro- and

INTRODUCTION

nanomaterials of a desired morphology and, therefore, provides a route for enhancing nanostructure order. Various porous “templates” are employed and the nanostructures are synthesized within the pores. If the templates used have spherical pores of uniform diameter, monodisperse nanospheres of the desired material are obtained within the voids of the template material. Depending on the operating parameters, these nanospheres may be solid (forms opals) or hollow (forms inverse opals). The nanostructures can remain inside the pores of the templates or they can be freed and collected by removing the templates. The most frequently used templates are polystyrene film. Two essential steps are needed. First step is to deposit the desired materials to fill the pores inside the membrane. Various deposition techniques could be utilized such as sol-gel, polymerization, atomic layer deposition (ALD), pulsed laser deposition (PLD), etc [31]. The second step is to remove the template to release and collect the nanostructures. Polystyrene can be removed by high temperature firing. Depending on the specific technology used, the process might have some additional steps involved. Various deposition techniques have been used to create titania 3-D structure inside the pores of template. Sol-gel is frequently used. The formula and recipe of sol-gel is not different from traditional sol-gel to produce nanoparticles or bulk materials. One just has to dip the template into the sol before the gelation happens to fill the pores with the sol under the drive of capillary force and gravity. Additional assistances could be taken to help the sol penetrate into the pores, such as centrifuge [32], vacuum pump [33], etc. One can also pre-treat the template surface to enhance the hydrophobicity or hydrophilicity depending on the sol formula to improve the filling efficiency. After filling, the sol-filled template will go through the same gelation-drycalcination process to form the desired crystal structure. It commonly occurs that thin films form on the top and bottom surfaces of membrane. Thus it is necessary to wipe away excessive sol on the surfaces or use mechanical polishing to thinning the calcined films after calcination. Then the template is removed to release the titania nanostructures. The morphology of the obtained materials

INTRODUCTION

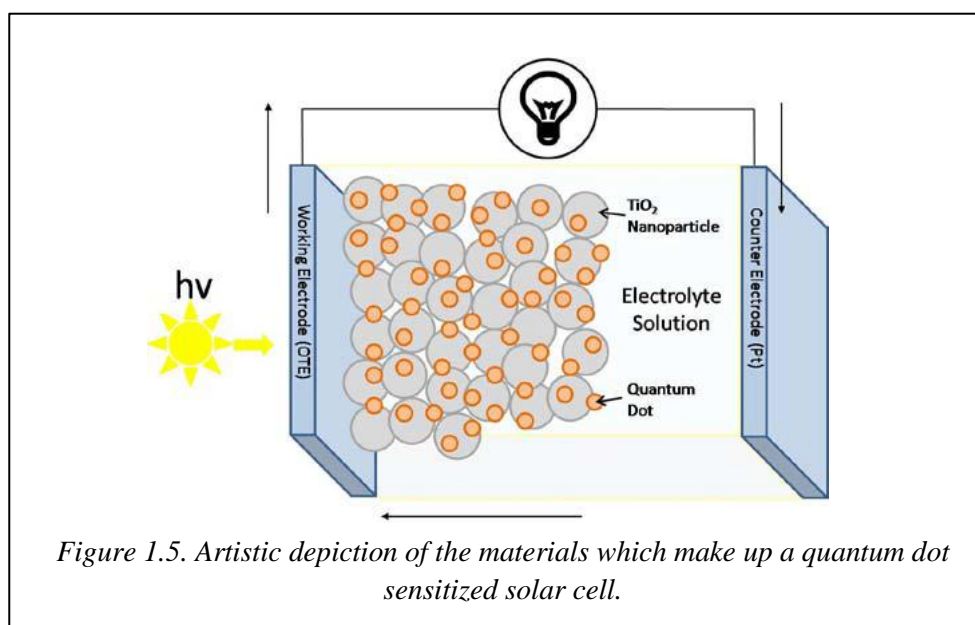
closely associated with the network geometry of the template used, and clusters or bundles of opals are normally seen. Sol-gel is the most accessible and economical method to produce nanomaterials. One can also use other techniques to do the deposition step such as electrophoresis deposition, atomic layer deposition, etc, depending on the available instruments and experimental conditions. Utilizing different deposition steps one has also to slightly adjust the specific steps in pre-deposition and template-removal processes.

1.3 Semiconductor quantum dots as solar cell sensitizers

Quantum dots are semiconducting materials which are synthesized in such a way that they are spherical in shape and have diameters at or below the materials' characteristic exciton Bohr radius. The Bohr radius of a material, which is linearly dependent on the materials' relative dielectric permittivity and inversely dependent on the materials' reduced effective mass has units of length and is a physical representation of the natural separation between a Coulombically bound electron and hole (exciton) within a material, such as what is generated immediately after the absorption of a photon. In bulk (large crystal lattice) materials, the crystal lattice is much larger than the size of the exciton, allowing free and independent movement of the exciton about the lattice. However, in a quantum dot, the size of the lattice is at or below the materials' exciton Bohr radius, which translates to a confinement of the electron-hole pair to a volume less than what it naturally wants to occupy. This "confinement effect" results in discrete energy levels (as opposed to a continuum of energy levels in a bulk sample) which exhibit particle-in-a-box like behavior [34]. Specifically, the stronger the confinement—the smaller the diameter of the quantum dot—the larger the bandgap of the material. In terms of implementation into solar cells as next generation sensitizers, quantum dots offer the use of multiple bandgaps from a single material simply by changing the size of that material.

INTRODUCTION

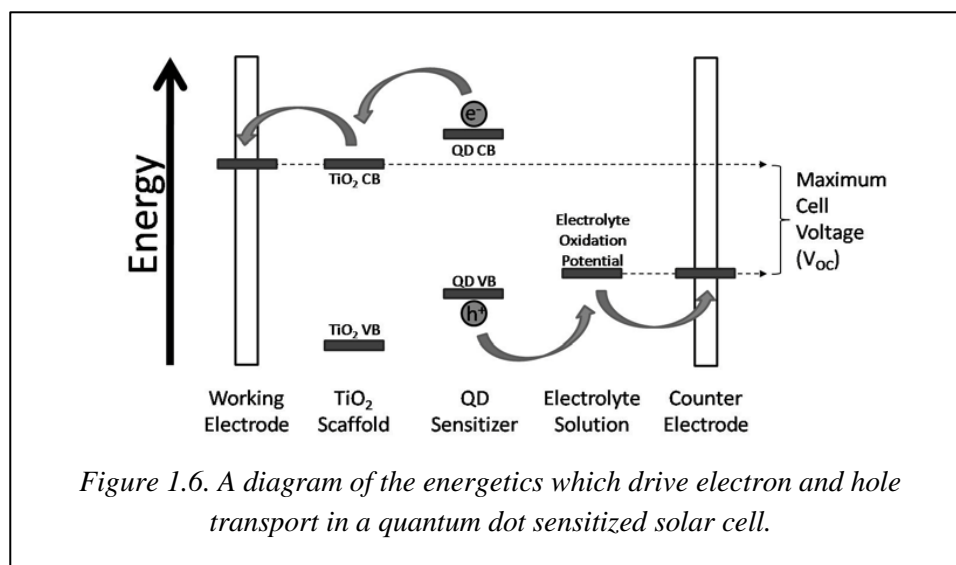
Therefore, to achieve maximum efficiency, one simply needs to optimize the performance of a single quantum dot material, which would efficiently convert one region of the solar spectrum due to the use of a single bandgap. Once this is achieved, one could then efficiently capture another region of the spectrum by changing the bandgap of the material, which in quantum dots means only changing the materials' size. Another advantage to using QDs as sensitizers in next generation solar cells is the wealth of attention which has been paid to popular QD materials in their non-quantized forms. For example, because of their absorption characteristics within the visible region of the solar spectrum, single crystal cadmium chalcogenides (CdX , $\text{X} = \text{S}, \text{Se}, \text{Te}$) were identified by many as an alternative to silicon in single crystal devices. As a result, much work was done by Bard [35], Hodes [36], and Wrighton [37], among others, in the 1970s and 1980s regarding morphological and electrolyte effects on performance and stability of CdS [38], CdSe [39], and CdTe [40] bulk photoanodes. As quantization effects became better understood and techniques were developed to synthesize and characterize cadmium chalcogenide materials which exhibit quantum confinement in the 1990s and beyond, the focus of these materials as sensitizers for next generation photovoltaics shifted sharply



INTRODUCTION

from bulk macroscopic samples to ordered nanostructured crystallites [41].

Quantum Dot Sensitized Solar Cell Design. Figure 1.5 shows an artistic depiction of the basic design of a quantum dot sensitized solar cell (QDSSC). The fundamental difference between a QDSSC and a dye sensitized solar cell is the material used to harvest the visible portion of the solar spectrum. The following paragraph discusses the necessary energetic considerations needed to assemble a functioning QDSSC. In order to successfully substitute the sensitizer in Grätzel cell (the dye) with a semiconducting quantum dot, one needs to consider the characteristic energetics of each cell component. It is easiest to understand the effect of energetics on cell voltage through an energy diagram. Figure 1.6 shows the energetics of the QD sensitizer, the TiO_2 scaffold, the electrolyte solution, along with the working and counter electrodes. Note that the position of the QDs' and TiO_2 's conduction and valence bands, along with the position of the electrolyte oxidation potential are shown as relative as opposed to absolute positions which are arranged in a way that promotes cell operation. The phrase “electrons sink and holes float” can be an aid in diagrams such as Figure 1.6, which literally means that electrons are energetically drawn to change energy level as low (more negative, vacuum



INTRODUCTION

scale) as possible, and holes to energy level as high (more positive, vacuum scale) as possible. In order for all of the reactions to take place as described above the two relative energy requirements must be met: the QD conduction band must lie above the TiO_2 conduction band, and the electrolyte potential must lie between the QD valence band and the TiO_2 conduction band. The maximum voltage is then defined as the energetic difference between the TiO_2 conduction band and the electrolyte oxidation potential, Figure 1.6 [42].

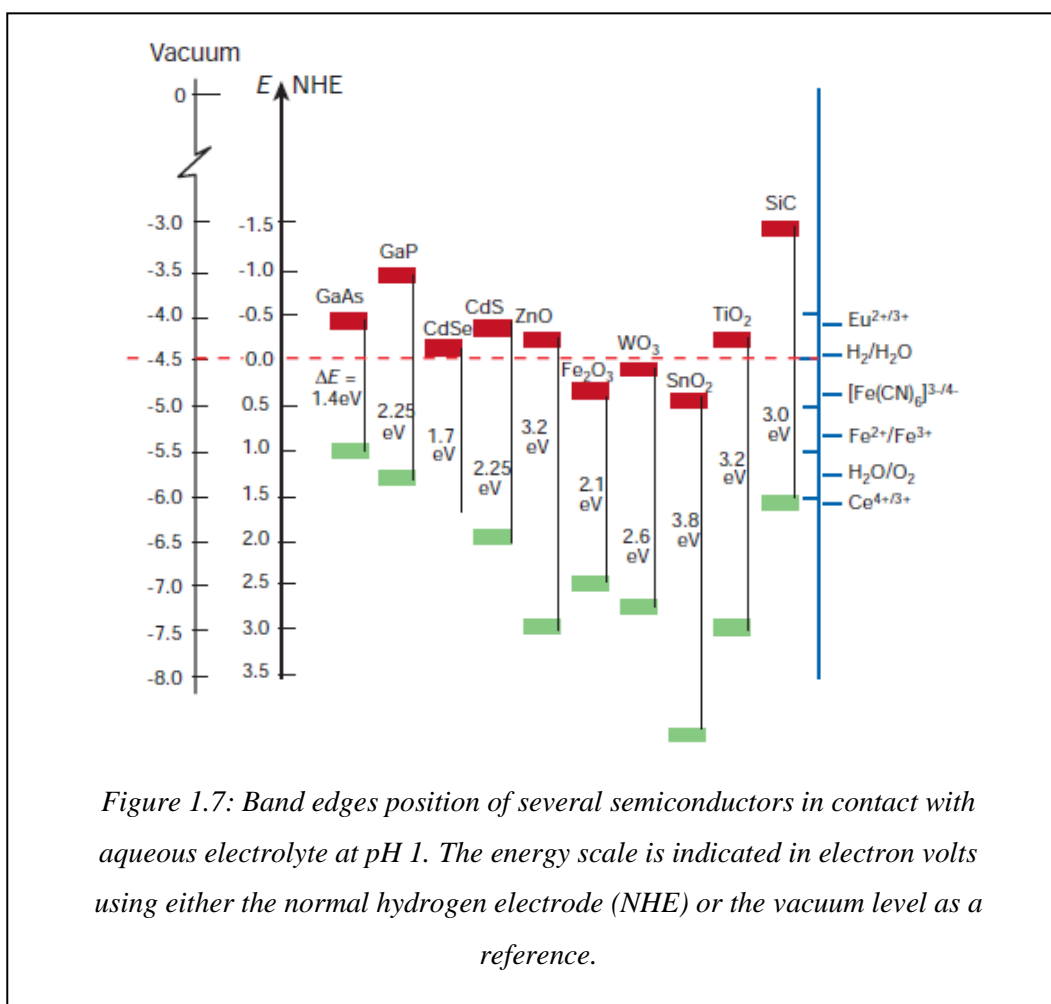


Figure 1.7: Band edges position of several semiconductors in contact with aqueous electrolyte at pH 1. The energy scale is indicated in electron volts using either the normal hydrogen electrode (NHE) or the vacuum level as a reference.

INTRODUCTION

1.3.1 Cadmium selenide

Cadmium selenide or cadmium (II) selenide, sometimes written as the chemical formula of CdSe, belongs to the class of II-IV semiconductors. CdSe is selected as the photosensitizer of TiO₂ due to its smaller band gap of CdSe relative to TiO₂ extending the optical absorption to visible region as well as its well-known properties (shown in Table 1.1). Moreover, the more negative energetic bottom level in conduction band of CdSe

Table 1.1 List of some properties of CdSe (Wurtzite structure).

Density:	5.81 g/cm ³
Lattice parameter	a = 4.2985 Å c = 7.0150 Å
Dielectric constant	10.2
Young's Modulus	5×10 ¹¹ dyne/cm ²
Electron mobility (300 K)	< 650 cm ² V ⁻¹ s ⁻¹
Coefficient of thermal expansion (500 K)	α ₁ =6.26×10 ⁻⁶ /K α ₃ =4.28×10 ⁻⁶ /K
Specific Heat	0.49 J/gK
Thermal conductivity (at 25 °C)	0.04 W/cmK
Max. Transmittance (λ =2.5-15 μm)	≥ 71 %
Absorption coefficient (λ =10.6 μm)	≤ 0.0015 cm ⁻¹ (including 2 surfaces)
Refractive index (λ =10.6 μm)	2.4
Solubility in water	Insoluble

INTRODUCTION

than that of TiO_2 and the more positive energetic top level in valence band of CdSe than that of TiO_2 (shown in Fig. 1.7 [43]) indicate the possible injection of photoexcited electrons from CdSe to TiO_2 conduction band and no injection of photoexcited holes from CdSe to TiO_2 valence band making the charge separation upon photoexcitation in CdSe feasible.

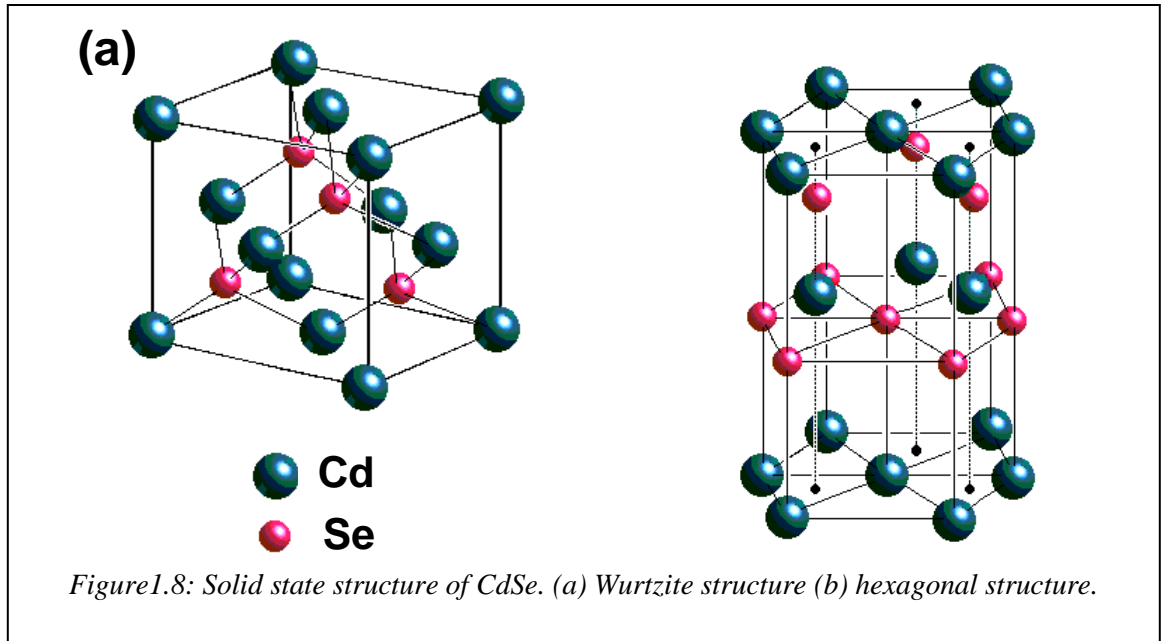
CdSe is generally yellow to red crystalline solid with melting point at 1268°C . This material can be crystallized in either the wurtzite or hexagonal structure, as shown in Fig. 1.8. The formula weight is 191.37 g/mol. It is an intrinsic semiconductor with a band gap of 1.70 eV at 300 K. Some characteristics of CdSe in wurtzite structure are presented in Table 1.1.

In nano size, CdSe exhibits the quantum confinement effect where CdSe nanocrystals of different sizes exhibit different colors. With decreasing crystal size the band gap of the crystal increases and the dot emits more energetic or bluer photons. CdSe QDs which is grown by using method of colloidal chemistry, (core-shell) CdSe/ZnS with trioctylphosphine oxide (TOPO) as surface stabilizing molecule has high luminescence efficiency (65 %) at room temperature. Recently this nanocrystal has found important applications in Biology. QDs are coupled to biological molecules for use in ultrasensitive biological detection at the single-dot level. Quantum dots are used there as fluorescent tags capable of tracing specific proteins within cells and in the future it is hoped to develop lighting up DNA or viruses by QDs.

1.3.2 Quantum confinement effect

The band gap (E_g) of a semiconductor is defined as the energy difference between the highest energy valence band states and the lowest energy conduction band states. The excitation of an electron from the valence band to the conduction band leaves a hole in the valence band. The electron and hole can form a bound state through Coulombic interactions. This bound electron-hole pair is called an exciton [44] (in this case a

INTRODUCTION



Wannier exciton). The bound state has energy slightly less than the energy of the band gap.

When the radius of the nanoparticle approaches the size of the exciton Bohr radius, the motion of the electrons and holes become confined in the nanoparticle. The Bohr radius (a_B) of the exciton is given by

$$a_B = \frac{4\pi\epsilon_0\epsilon_\infty\eta^2}{m_0e^2} \left(\frac{1}{m_e^*} + \frac{1}{m_h^*} \right) \quad (2.1)$$

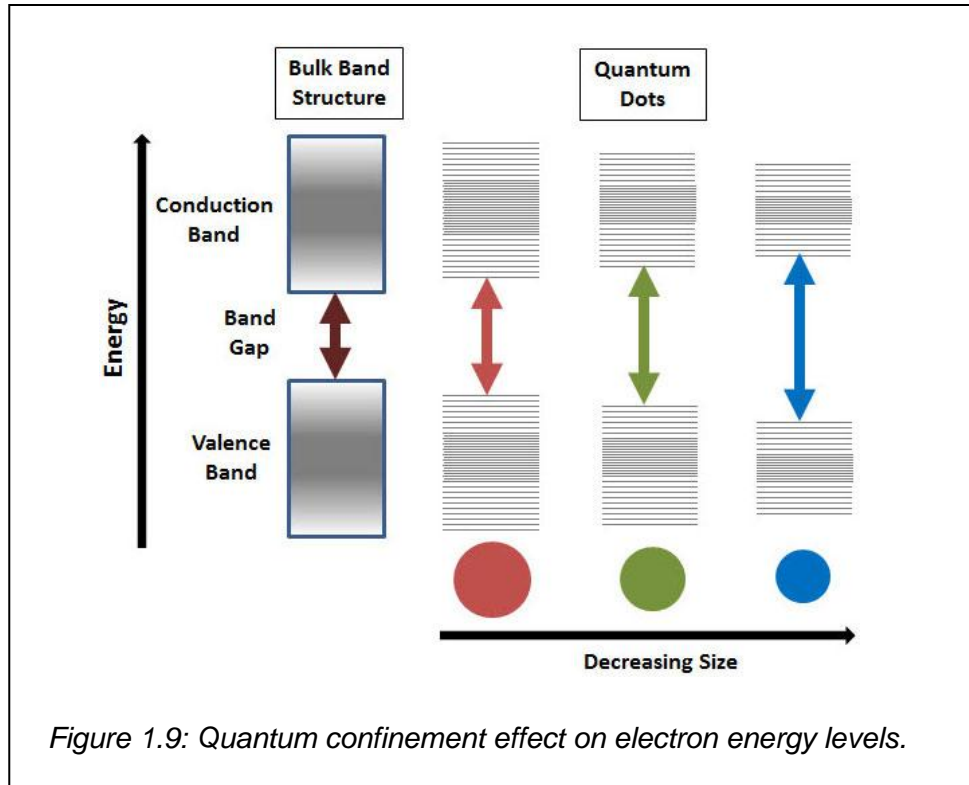
where ϵ_∞ is the high frequency relative dielectric constant of the medium

m_e is the effective mass of the electron (in m_0 units)

m_h is the effective mass of the hole (in m_0 units)

m_0 is the mass of the electron at rest.

This resulting Bohr radius for excitons in semiconductors is much larger than that of hydrogen atom. A created electron-hole pair can only “fit” into a nanoparticle when the



charge carriers are in a state of higher energy. As a consequence of this, the band gap increases with decreasing particle size. In this regime of spatial confinement, the kinetic energy becomes quantized and the energy bands split into discrete levels shown in Fig. 2.3. Regarding this, both the absorption and emission spectra of the material shift to higher energies with decreasing particle size.

One possible way to explain the quantum confinement effect is through the use of the effective mass approximation approach (EMA) [45]. Here, the size dependency of the band gap of the nanoparticle can be derived as:

$$E - E_g = \frac{\pi^2 \eta^2}{2m_o R^2} \left(\frac{1}{m_e^*} + \frac{1}{m_h^*} \right) - \frac{1.8e^2}{4\pi\epsilon_o\epsilon_\infty R} \quad (2.2)$$

where R is the radius of the semiconductor particle and E_g is the band gap of the bulk semiconductor. The first term in the equation above represents the particle in box

INTRODUCTION

quantum localization energy and has a $1/R^2$ dependence. The second term represents the Coulomb energy having a $1/R$ dependence. For large R values, E approaches E_g .

1.3.3 Hot carrier and multiple exciton generation

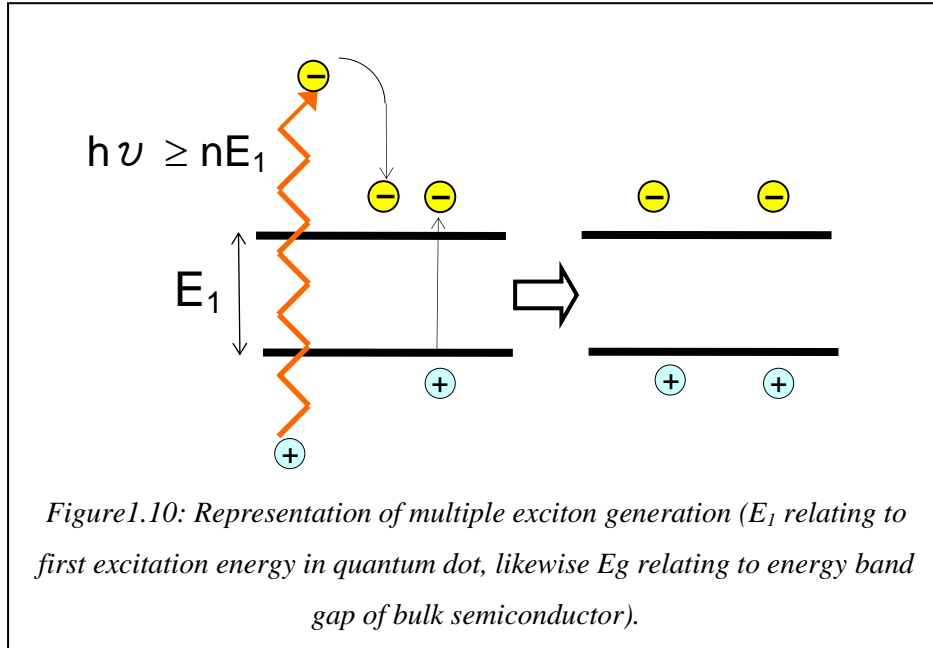
Photoexcitation of a semiconductor with photons having energies above the band gap of semiconductor creates electron and holes with a total excess kinetic energy equal to the difference between the photon energy and band gap. This excess kinetic energy causes the effective temperature of carriers much higher than the lattice temperature, called as hot electrons and hot holes. To enhance the energy conversion efficiency, two fundamental ways to utilize hot carriers has been proposed by Nozik [46], i.e. enhanced photovoltage and enhanced photocurrent. By utilizing hot photogenerated carriers to produce higher photovoltages and photocurrents, the maximum attainable thermodynamic conversion efficiency of solar photon could increase up to about 66 % from 31% for Shockley-Queisser limit [47] of single band gap cells. The former requires the extraction of the hot carriers before they cool through their respective carrier-carrier collisions (called carrier thermalization) and carrier-phonon interactions (phonon emission occurs as the result of the cooling of the carriers and heating of the lattice until carrier and lattice temperatures become equal; the phonons involved in the process are the longitudinal optical phonons). In order to achieve this, the rates of the photogenerated carrier separation, transport and interfacial transfer across the semiconductor interface must all be fast compared with the rate of carrier cooling. The latter requires the energetic hot carriers to produce a second or more electron-hole pairs (multiple exciton generation, MEG) through impact ionization due to strong carrier-carrier interactions, as shown in Fig. 1.10. This is the inverse of an Auger process whereby two electron-hole pairs recombine to produce a single highly energetic electron-hole pair. Thus for enhanced photocurrent, the rate of impact ionization (i.e. inverse Auger effect) should be greater than the rate of Auger process or carrier cooling.

INTRODUCTION

In bulk semiconductor, this MEG is inefficient because of the relatively weak Coulomb interactions, the restrictions imposed by energy and translational momentum conservation, as well as fast energy loss due to phonon emission. Strict selection rules and competing processes in the bulk permit MEG at energies of $n \times E_g$ where E_g is the band gap of bulk semiconductor and $n > 3$; however, efficient MEG is observed only for $n > 5$ as a matter of fact [48]. On the other hand, MEG become efficient in zero-dimensional quantum dots with the lower values of n (typically 2-3) [49] with respect to E_1 (first excitation energy and not E_g any longer in quantum confinement regime) because of wide separation between discrete electronic states inhibiting phonon emission due to phonon bottleneck, stronger Coulomb interactions and relaxation in translational momentum conservation. In phonon bottleneck [50], a large population of hot carriers produces a non equilibrium distribution of phonon (in particular, LO phonon that are the type involved in the electron-phonon interactions at high carrier energies) because the LO phonons cannot equilibrate fast enough with crystal bath; these hot LO phonons can be reabsorbed by the electron plasma to keep it hot. Besides Auger mechanism; electron-hole scattering, deep-level trapping and acoustical-optical photon interactions are other possible mechanisms for breaking the phonon bottleneck.

The first experimental evidence for high efficiency MEG in quantum dot was detected in PbSe QDs [51]. Later, MEG was also observed for QDs of other semiconductor, such as PbTe [52], CdSe [53], InAs [54] including an important photovoltaic material Si. Moreover, MEG in photocurrent was indicated in PbSe QD device structure. However, more recent studies have questioned the efficiency of MEG particularly for CdSe and InAs QDs. Synthesis differences between samples may left some with the QD surfaces that affect the efficiency of MEG. So engineering QDs is the key factor to optimize the potential MEG in solar cell applications.

INTRODUCTION



References

- [1] A. Goetzberger, and V. U. Hoffman, *Photovoltaic Solar Energy Generation* (Springer, Germany, 2005).
- [2] S. Nishimura, N. Abrams, B. A. Lewis, L. I. Halaoui, T. E. Mallouk, K. D. Benkstein, J. van de Lagemaat, and A. J. Frank, *J. Am. Chem. Soc.* **125**, 6306 (2003).
- [3] C. L. Huisman, J. Schoonman, and A. Goossens, *Sol. Energy Mater. Sol. Cells.* **85**, 115 (2005).
- [4] P. R. Somani, C. Dionigi, M. Murgia, D. Palles, P. Nozar, and G. Ruani, *Sol. Energy Mater. Sol. Cells* **87**, 513 (2005).
- [5] W. W. Yu, L. Qu, W. Guo, and X. Peng, *Chem. Mater.* **15**, 2854 (2003).
- [6] B. O'Regan, and M. Gratzel, *Nature* **353**, 737 (1991).
- [7] A. Yella, H. W. Lee, H. N. Tsao, C. Yi, A. K. Chandiran, M. K. Nazeeruddin, E. W. Diau, C. Yeh, S. M. Zakeeruddin, and M. Gratzel, *Science* **334**, 629 (2011).
- [8] R. Vogel, P. Hoyer, and H. Weller, *J. Phys. Chem.* **98**, 3183 (1994).
- [9] J. H. Im, C. R. Lee, J. W. Lee, S. W. Park, and N. G. Park, *Nanoscale* **3**, 4088 (2011).
- [10] S. Tanaka, *Jpn. J. Appl. Phys.* **40**, 97 (2001).
- [11] J. P. Holdren, *Science* **456**, 424 (2008).
- [12] Y. L. Lee, and Y. S. Lo, *Adv. Funct. Mater.* **19**, 604 (2009).
- [13] S. J. Roh, R. S. Mane, S. K. Min, W. J. Lee, and S. H. Lokhande, *Appl. Phys. Lett.* **89**, 253512 (2006).
- [14] J. Chen, J. L. Song, X. W. Sun, W. Q. Deng, C. Y. Jiang, W. Lei, J. H. Huang, and R. S. Liu, *Appl. Phys. Lett.* **94**, 153115 (2009).

INTRODUCTION

- [15] S. Giménez, I. Mora-Seró, L. Macor, N. Guijarro, T. Lana-Villarreal, R. Gómez, L. J. Diguna, Q. Shen, T. Toyoda, and J. Bisquert, *Nanotechnology* **20**, 295204 (2009).
- [16] J. Xu, X. Yang, Q. Yang, T. Wong, S. Lee, W. Zhang, and C. Lee, *J. Mater. Chem.* **22**, 13374 (2012).
- [17] J. Kim, H. Choi, C. Nahm, C. Kim, S. Nam, S. Kang, D. Jung, J. I. Kim, J. Kang, and B. Park, *J. Power Sources* **220**, 108 (2012).
- [18] R. J. Ellingson, M. C. Beard, J. C. Johnson, P. Yu, O. I. Micic, A. J. Nozik, A. Shabaev, and A. L. Efros, *Nano Lett.* **5**, 865 (2005).
- [19] S. Ito, P. Liska, P. Comte, R. Charvet, P. Pechy, U. Bach, L. Schmidt-Mende, S. M. Zakeeruddin, A. Kay, M. K. Nazeeruddin, and M. Gratzel, *Chem. Commun.*, 4351 (2005).
- [20] Y. Liu, X. Sun, Q. Tai, H. Hu, B. Chen, N. Huang, B. Sebo, and X. Zhao, *J. Power Sources* **196**, 475 (2011).
- [21] H. Choi, C. Nahm, J. Kim, J. Moon, S. Nam, C. Kim, D. Jung, and B. Park, *Curr. Appl. Phys.* **12**, 737 (2012).
- [22] S. Waita, B. Aduda, J. Mwabora, G. Niklasson, C. Granqvist, and G. Boschloo, *J. Electroanal. Chem.* **637**, 79 (2009).
- [23] A. E. Goresy, M. Chen, L. Dubrovinsky, P. Gillet, and G. Graup, *Science* **293**, 1467 (2001).
- [24] O. Carp, C. L. Huisman, and A. Reller, *Progress in Solid State Chemistry* **32**, 33 (2004).
- [25] G. Praff, and P. Reynders, *P. Chem. Rev.* **99**, 1963 (1999).
- [26] W. Plieth, *Electrochemistry for Materials Science* (Elsevier, 2008).
- [27] M. Gratzel, *Nature* **414**, 338 (2001).
- [28] N. S. Nalwa, *Encyclopedia of Nanoscience and Nanotechnology* (American

INTRODUCTION

Scientific Publishers, 2004).

- [29] X. Chen, and S. S. Mao, *Chem. Rev.* **107**, 2891 (2007).
- [30] M. R. Hoffmann, S. T. Martin, W. Choi, and D. W. Bahnemann, *Chem. Rev.* **95**, 69 (1995).
- [31] M. S. Sander, M. J. Cote, W. Gu, B. M. Kile, and C. P. Tripp, *Adv. Mater.* **16**, 2052 (2004).
- [32] T. Wen, J. Zhang, T. P. Chou, S. J. Limmer, and G. Cao, *J. Sol-Gel Sci. Tech.* **33**, 193 (2005).
- [33] J. Wang, A. Manivannan, and N. Q. Wu, *Thin Solid Films* **517**, 582 (2008).
- [34] O. Millo, D. Katz, Y. W. Cao, and U. Banin, *Phys. Rev. Lett.* **86**, 5751 (2001).
- [35] A. J. Bard, H. D. Abruna, C. E. Chidsey, L. R. Faulkner, S. D. Feldberg, K. Itaya, M. Majda, O. Melroy, R. W. Murray, M. D. Porter, M. P. Soriaga, and H. S. White, *J. Phys. Chem.* **97**, 7147 (1993).
- [36] J. Manassen, D. Cahen, G. Hodes, and A. Sofer, *Nature* **263**, 97 (1976).
- [37] M. S. Wrighton, *ACS Symp. Ser.* **211**, 59 (1983).
- [38] C. Y. Liu, and A. J. Bard, *J. Phys. Chem.* **93**, 7749 (1989).
- [39] J. J. Hickman, and M. S. Wrighton, *J. Am. Chem. Soc.* **113**, 4440 (1991).
- [40] K. D. Dobson, I. Visoly-Fisher, G. Hodes, and D. Cahen, *Adv. Mater.* **13**, 1495 (2001).
- [41] G. Hodes, and M. Gratzel, *Nouv. J. Chim.* **8**, 509 (1984).
- [42] D. Cahen, G. Hodes, M. Gratzel, J. F. Guillemoles, and I. Riess, *J. Phys. Chem. B* **104**, 2053 (2000).
- [43] A. Hagfeldt, and M. Gratzel, *Chem. Rev.* **95**, 49 (1995).
- [44] C. Kittel, *Introduction to Solid State Physics*, 6th ed. (John Wiley and Sons, New

INTRODUCTION

York, 1986).

- [45] L. E. Brus, *J. Chem. Phys.* **80**, 4403 (1984).
- [46] A. J. Nozik, *Annu. Rev. Rhys. Chem.* **52**, 193 (2001).
- [47] W. Shockley, and H. J. Queisser, *J. Appl. Phys.* **32**, 510 (1961).
- [48] S. Kolodinski, J. H. Werner, T. Wittchen, and H. Queisser, *Appl. Phys. Lett.* **63**, 2405 (1993).
- [49] A. J. Nozik, *Physica E* **14**, 115 (2002).
- [50] R. P. Joshi, and D. K. Ferry, *Phys. Rev. B* **39**, 1180 (1989).
- [51] R. D. Schaller, and V. I. Klimov, *Phys. Rev. Lett.* **92**, 186601 (2004).
- [52] J. E. Murphy, M. C. Beard, A. G. Norman, S. P. Ahrenkiel, J. C. Johnson, P. Yu, O. I. Micic, R. J. Ellingson, and A. J. Nozik, *J. Am. Chem. Soc.* **128**, 3241 (2006).
- [53] R. D. Schaller, M. A. Petruska, and V. I. Klimov, *Appl. Phys. Lett.* **87**, 253102 (2005).
- [54] R. D. Schaller, J. M. Pietryga, and V. I. Klimov, *Nano Lett.* **7**, 3469 (2007).



Experimental procedures

2.1 Sample preparation

2.1.1 Inverse opal titanium dioxide

The inverse opal TiO₂ was prepared by filling the void in an artificial template and subsequently removing the template. Generally speaking, it can be grouped into three steps as follows, as briefly described in Fig. 2.1

(1) Template preparation [1]

1. Conductive fluorine-doped tin oxide (FTO) coated glass of 4.5 cm length and 2.3 cm width was cleaned ultrasonically with detergent, concentrated KOH, distilled water and methanol, consecutively.
2. 10 wt% of monodisperse hydrophobic polystyrene latex from Seradyn Co. was diluted with distilled water to a concentration of 0.1 wt%. The suspension was then dispersed ultrasonically for 30 min.
3. The FTO glass was immersed vertically in 30 ml beaker containing 15 ml latex suspension.
4. The beaker was then kept in an oven at 40°C for 1 to 2 days until the suspension was fully evaporated.

EXPERIMENTAL PROCEDURES

(2) Filling the void in template with TiO₂

1. 2 % TiCl₄ (from WAKO, 99 %) in methanol (from WAKO, 99.8 %) as TiO₂ source was prepared by mixing 2 ml TiCl₄ and 98 ml methanol [2].
2. 2 % TiCl₄ in methanol was vertically dropped on to a 1.3 x 2.3 cm template by using a 10- μ l sized micropipette.
3. The template was then kept in a desiccator (humidity 45-50 %, temperature 24-25%) for 30 min.
4. The template was heated in an oven at 80°C for 10 min.
5. The 2-4 processes were repeated for few times.

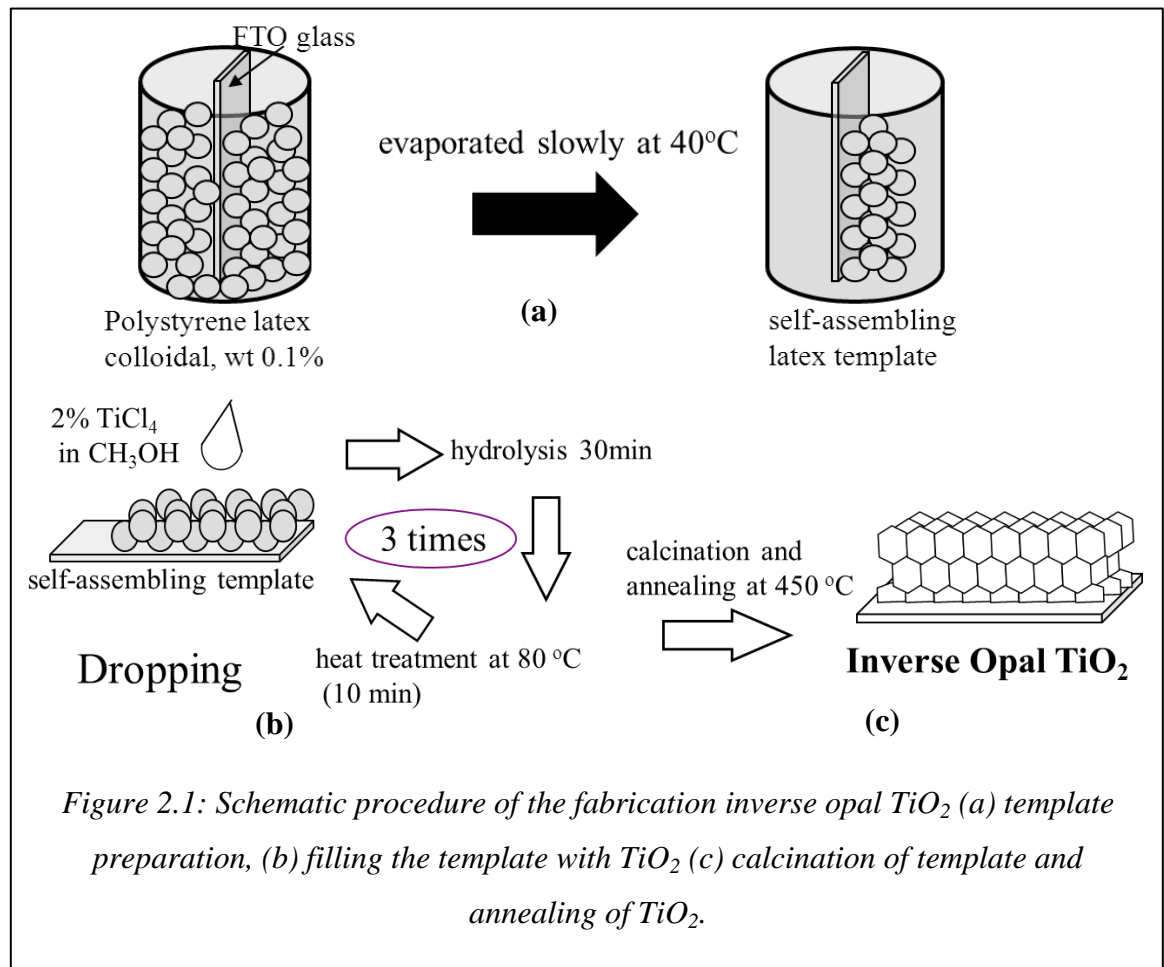


Figure 2.1: Schematic procedure of the fabrication inverse opal TiO₂ (a) template preparation, (b) filling the template with TiO₂ (c) calcination of template and annealing of TiO₂.

EXPERIMENTAL PROCEDURES

In this step, heat treatment time at 80°C is necessary to make a compact structure before the further addition of TiCl₄.

(3) Calcinations of the template and annealing of TiO₂

Calcinations of the template and annealing of TiO₂ were conducted together in which the sample was heated at 450°C with 0.5°C/min heating rate. After 1 hour heating at 450°C, the temperature was cooled down to room temperature within 3 hours.

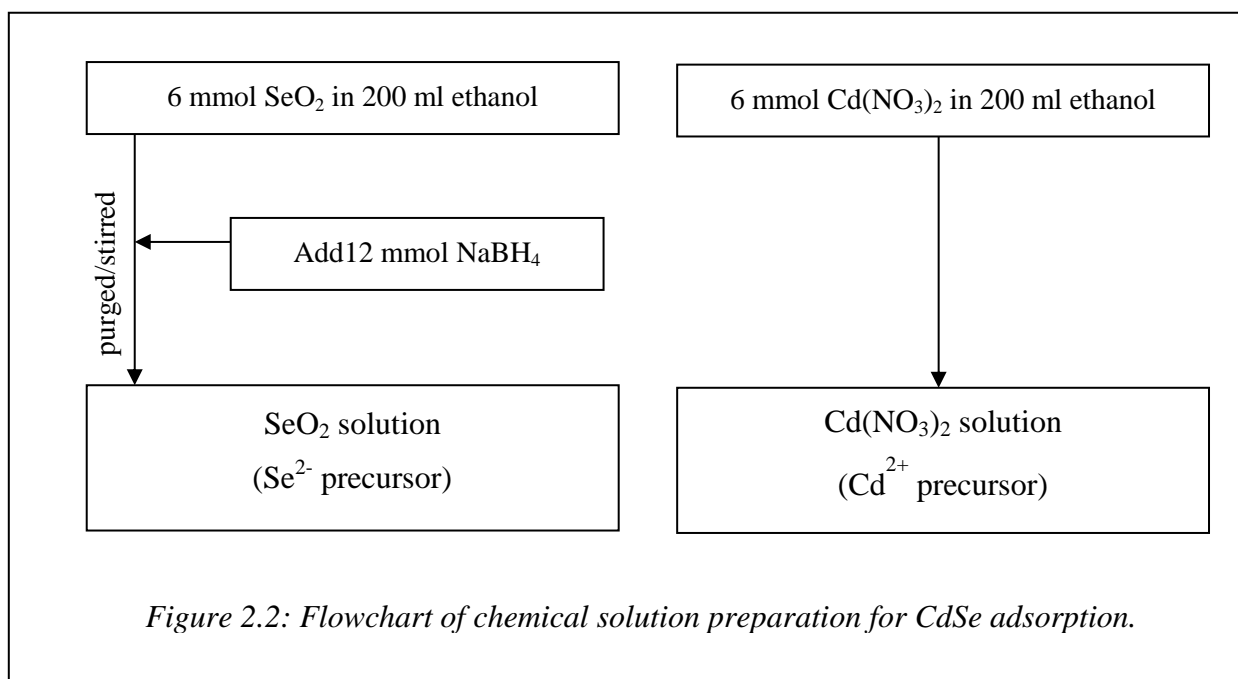
2.1.2 Adsorption of CdSe QDs on inverse opal TiO₂

Figure 2.2 shows a flowchart of chemical solution preparation for CdSe adsorption and figure 2.3 shows the order of TiO₂ is dipped in the solution. All chemicals used in this deposition process are cadmium nitrate tetrahydrate ($\geq 99.0\%$), selenium dioxide ($\geq 97.0\%$), and sodium tetrahydroborate ($\geq 95.0\%$) obtained from WAKO. For this study, CdSe QDs adsorption on inverse opal TiO₂ was conducted by successive ionic layer adsorption and reaction (SILAR) method similar to what H. Lee, et. al. [3] has done. The adsorption procedure is as follows:

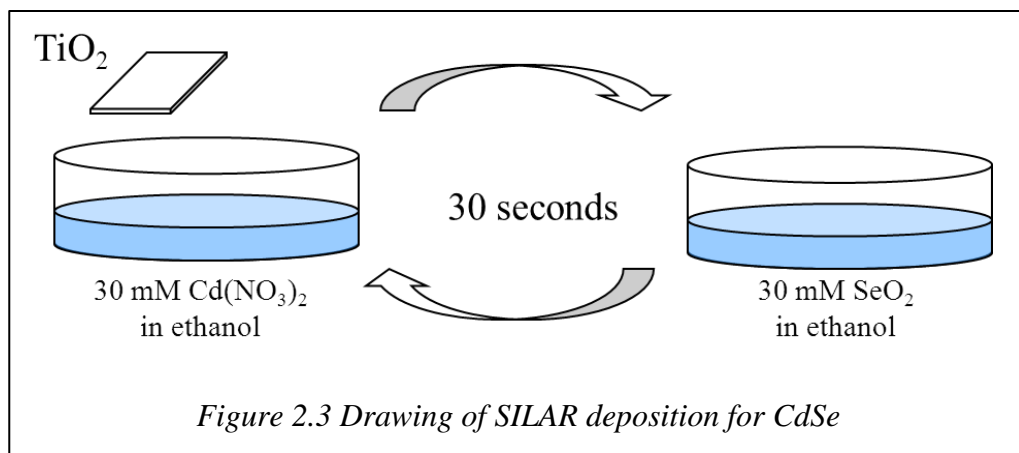
1. Weigh metal nitrates in vials in order to make 30 mM Cd(NO₃)₂ solution later and put those inside the glove box.
2. 0.6657 g of SeO₂ is dissolved in 200 mL ethanol (30 mM), and purged/stirred for about 2 minutes and 0.4539 g of NaBH₄ (60 mM) added into the round-bottom flask containing SeO₂, and purged/stirred for about 1 hour.
3. Pure ethanol in large volume is also prepared and purged for 1 hour separately for making metal nitrate solutions and washing the electrodes used inside glove box.

EXPERIMENTAL PROCEDURES

4. Move the bottom in (2) and (3) inside the glove box, which then was sealed and purged with inert gas (N_2). Evacuation/purging were made the inside atmosphere with a low oxygen level.
5. Inside the glove box, prepare metal nitrate solution designated above in one beaker and selenide solution in another beaker.
6. The TiO_2 -modified electrode was dipped into the metal²⁺ solution, pure ethanol (then dried), the Se^{2-} solution, and then pure ethanol (then dried) successively for 30 seconds for deposition each and longer time for washing and dried. Such an immersion cycle was repeated several times. The electrode became darker as the number of SILAR cycles was increased.



EXPERIMENTAL PROCEDURES

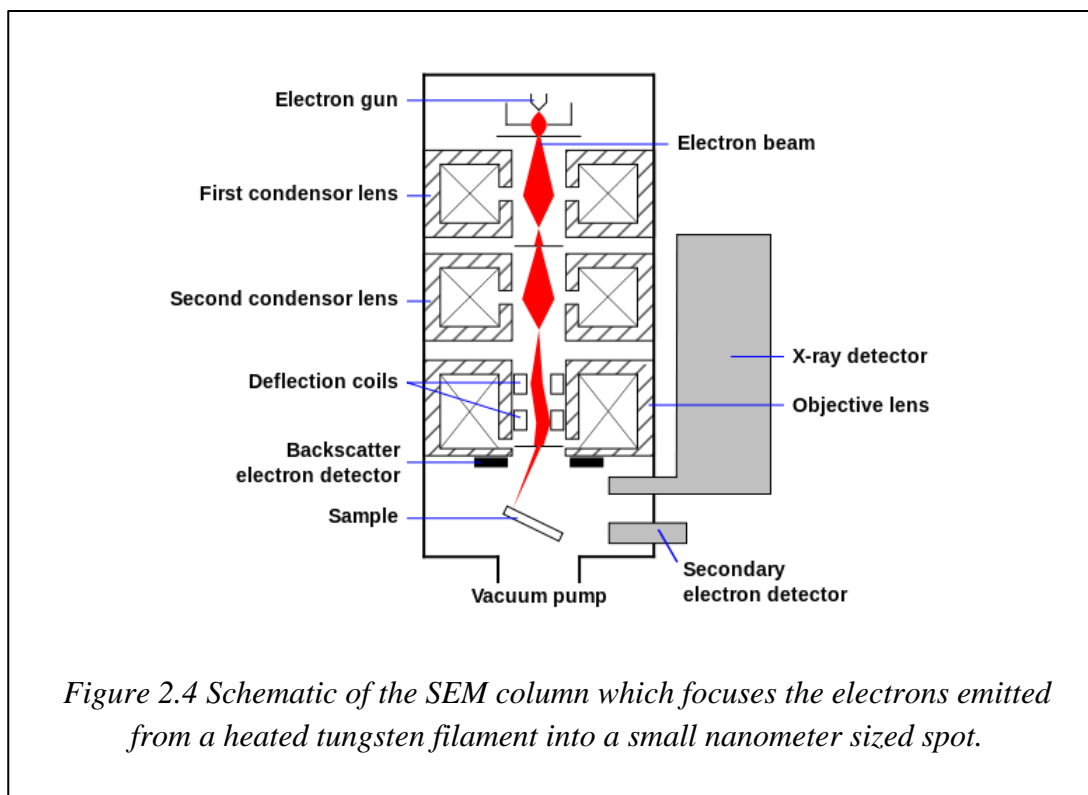


2.2 Characterization

2.2.1 Scanning electron microscopy [4]

Scanning electron microscopy (SEM) is the best known and most widely-used of the surface analytical techniques. The first Scanning Electron Microscope (SEM) debuted in 1942 with the first commercial instruments around 1965. SEM is considered a relatively rapid, inexpensive, and basically non-destructive approach to surface analysis. High resolution images of surface topography, with excellent depth of field are produced using a highly-focused, scanning (primary) electron beam. The primary electrons enter a surface with energy of 0.5 - 30 keV is focused in the microscope column (Fig. 2.4) through a combination of condenser lenses and apertures, and generate many low energy secondary electrons. The intensity of these secondary electrons is largely governed by the surface topography of the sample. An image of the sample surface can thus be constructed by measuring secondary electron intensity as a function of the position of the scanning primary electron beam. High spatial resolution is possible because the primary electron beam can be focused to a very small spot (< 10 nm). High sensitivity to topographic features on the outermost surface (< 5 nm) is achieved when using a primary electron beam with an energy of > 1 keV. In addition to low energy secondary electrons,

EXPERIMENTAL PROCEDURES



backscattered electrons and X-rays are also generated by primary electron bombardment. The intensity of backscattered electrons can be correlated to the atomic number of the element within the sampling volume. Hence, some qualitative elemental information can be obtained. The analysis of characteristic X-rays emitted from the sample gives more quantitative elemental information. Such X-ray analysis can be confined to analytical volumes as small as 1 cubic micron

2.2.2 X-ray diffraction spectrometry [5]

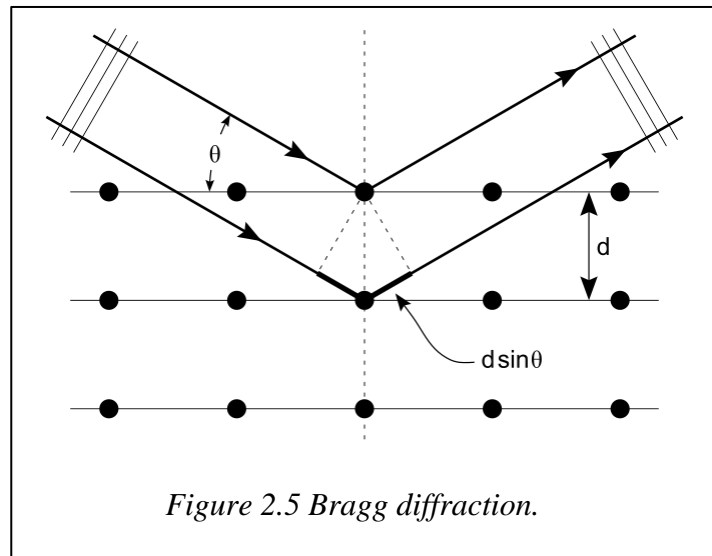
In 1895, the German physicist Roentgen discovered X-rays. Even before this method was understood, people had already begun to use it. Its earliest use was for radiographic method. Later, it was put to use by engineers wanting to study the internal structure of opaque objects. It was not until 1912 that the phenomenon of X-rays

EXPERIMENTAL PROCEDURES

diffraction by crystal was discovered, and this simultaneously proved the wave nature of X-rays and provided a new method for investigating the fine structure of matter.

X-ray diffraction (XRD) is the coherent scattering of X-rays by a crystalline material. This technique can be used to obtain a wide range of structural information. The X-ray diffraction peaks from a polycrystalline solid can be used to determine the crystalline phase of the material, average grain size, residual stress, and preferred crystalline orientation (texture). High-resolution x-ray diffraction can be used to obtain the orientation and quality of single crystals and the composition and relaxation of epitaxial layers. XRD is a non-destructive technique and requires no special sample preparation. In powder diffraction, the sample is sufficiently random orientation of the crystals, and then exposed to monochromatic x-rays. If the orientation of the crystalline particles is truly random with its characteristic interplanar spacing (d), there will be enough correctly oriented particles to satisfy Bragg's law (Eq. 2.1). Different families of planes will satisfy Bragg's law for different values of θ and the intensity of the reflection is measured as the detector is rotated through the angle 2θ .

$$n\lambda = 2d \sin \theta \quad (2.1)$$



EXPERIMENTAL PROCEDURES

where n is an integral number of the wavelength λ . The XRD spectra are most commonly obtained using $\text{CuK}\alpha$ radiation (wavelength, $\lambda = 1.5428\text{\AA}$).

When the size of the individual crystals is less than $0.1\mu\text{m}$ (1000\AA), the term particle size is used [6]. Crystals that have small sizes causes a broadening in the Debye rings. The extent of this broadening is given by the following equation (called the Debye-Scherrer formula):

$$B = \frac{0.9\lambda}{t \cos \theta} \quad (2.2)$$

where

B is the broadening of the diffraction line, measured at half its maximum intensity (radians)

t is the diameter of the crystal particle

λ is the X-ray wavelength

θ is the angle of incidence of the X-ray beam at the maximum of the diffraction beam.

When the particle size exceeds 1000\AA , B is essentially zero.

2.2.3 Photoacoustic spectroscopy

One of the most effective means for studying the properties of matter nondestructively is to observe how photons interact with the material. This is known as optical spectroscopy. This can be done by absorption and reflection spectroscopy. Another usable technique involves the measurement of photoacoustic signals. The term of photoacoustic usually refers to the generation of acoustic waves by modulated optical radiation [7]. In a broader sense, photoacoustic means the generation of acoustic waves or other thermoelastic effects by any type of energetic radiation, including electromagnetic radiation from radio frequency to x ray, electrons, protons, ions and other particles.

EXPERIMENTAL PROCEDURES

Rosencwaig-Gersho Theory

In 1976, Rosencwaig and Gersho derived the analysis of the photoacoustic process in solid. The Rosencwaig-Gersho theory is based on the generally accepted mechanism for the photoacoustic effect in condensed phase. A modulated monochromatic beam of light is incident on the sample surface. The light is absorbed by the sample to a degree dependent upon the optical absorption coefficient of the sample. As a result the sample is periodically heated and cooled at the modulation frequency. The periodic temperature change is transmitted to a boundary layer of gas at the sample surface. The boundary layer of gas expands and contracts with the temperature variation, acting as a small acoustic piston analogous to a vibrating plate. The acoustic signal which is produced in the confined gas is detected by a microphone.

An outline of the Rosencwaig-Gersho derivation is given making reference to Fig. 2.6. A monochromatic beam of light with intensity I_0 is modulated at frequency $\omega/2\pi$. The incident modulated beam has intensity I :

$$I = \frac{1}{2}I_0(1 + \cos \omega t) \quad (2.3)$$

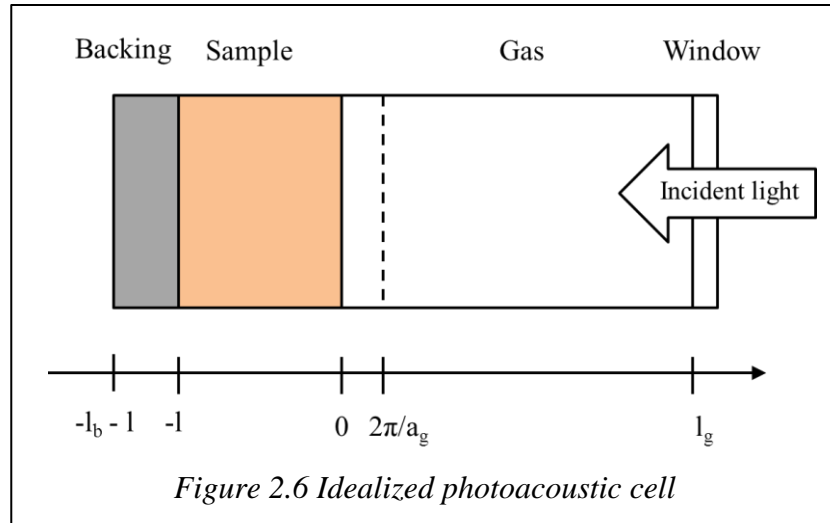
As the light beam is transmitted into the sample, energy is deposited in the sample in a Lambert's law manner:

$$\frac{di}{dx} = -\beta i \quad (2.4)$$

where i is the transmitted intensity and β is the absorption coefficient. Assuming that the absorbed energy is degraded to heat in time, t , shorter than $2\pi/\omega$ and assuming that the absorbed energy is completely degraded to heat, the heat density at depth x in the sample is:

$$I\beta e^{\beta x} = \frac{1}{2}\beta e^{\beta x}(1 + \cos \omega t) \quad (2.5)$$

EXPERIMENTAL PROCEDURES



Thus, for a nonscattering sample the heat density which drives the periodic of the sample depends on the optical absorption coefficient and the modulation frequency.

The temperature fluctuation produced at the sample surface ($x = 0$) depends not only on the heat density but also on the thermal diffusivity of the sample, α_s . The temperature change produced in the acoustic cell is described by the thermal diffusion equations shown below.

$$\frac{\partial^2 \phi}{\partial x^2} = \frac{1}{\alpha_s} \frac{\partial \phi}{\partial t} - \frac{\beta I_0}{2k_s} e^{\beta x} (1 + e^{i\omega t}), \quad -l \leq x \leq 0 \quad (2.6)$$

$$\frac{\partial^2 \phi}{\partial x^2} = \frac{1}{\alpha_b} \frac{\partial \phi}{\partial t}, \quad -l - l_b \leq x \leq -l \quad (2.7)$$

$$\frac{\partial^2 \phi}{\partial x^2} = \frac{1}{\alpha_g} \frac{\partial \phi}{\partial t}, \quad 0 \leq x \leq l_g \quad (2.8)$$

The term used to describe thermal properties are defined as follows:

ϕ is temperature.

α_j is thermal diffusivity of material j .

a_j is thermal diffusion coefficient of material j .

k_j is thermal conductivity of material j

ρ_j is density of material j .

EXPERIMENTAL PROCEDURES

c_j is specific heat of material j .

where

$$\alpha_j = \frac{k_j}{\rho_j c_j} \quad (2.9)$$

and

$$a_j = \left(\frac{\omega}{2\alpha_j} \right)^{1/2} \quad (2.10)$$

The subscript, j , denotes backing (b), gas (g), sample (s), or reference sample (r).

Rosencwaig and Gersho derive a solution to these equations for the time-dependent temperature at the sample surface using appropriate boundary conditions and reasonable simplifying assumptions. The time-dependent temperature at the gas-solid boundary is integrated over the thickness of the gas boundary layer, $2\pi\mu_g$, giving the spatially averaged temperature of the boundary layer.

$$\bar{\phi}(t) = \int_0^{2\pi\mu_g} \phi(x, t) dx = \frac{1}{2\sqrt{2}\pi} \phi_0 e^{i(\omega t - n)} \quad (2.11)$$

Assuming that the gas boundary layer acts as an adiabatic acoustic piston, Rosencwaig and Gersho solve for the pressure change as a function of time. The general solution for the acoustic response function, $\Delta P(t)$, is:

$$\Delta P(t) = Q e^{i(\omega t - n)} \quad (2.12)$$

where

$$Q = \frac{Q I_0 \gamma P_0}{2\sqrt{2} k_s l_g a_g T_0 (\beta^2 - \sigma_s^2)} \left[\frac{(r-1)(b+1)e^{\sigma_s l} - (r+1)(b-1)e^{-\sigma_s l} + 2(b-r)e^{\beta l}}{(g+1)(b+1)e^{\sigma_s l} - (g-1)(b-1)e^{-\sigma_s l}} \right] \quad (2.13)$$

The terms used are defined as follows:

P_0 is ambient pressure

T_0 is ambient temperature

γ is ratio of specific heats for gas.

η is phase delay for production of acoustic signal ($\sim \pi/4$)

EXPERIMENTAL PROCEDURES

where

$$b = \frac{k_b a_b}{k_s a_s} \quad (2.14)$$

$$g = \frac{k_g a_g}{k_s a_s} \quad (2.15)$$

$$r = \frac{(1-i)\beta}{2a_s} \quad (2.16)$$

$$\sigma_s = (1 + i)a_s \quad (2.17)$$

Because this complex function is not easily interpreted, Rosencwaig and Gersho develop six special case depending on the limiting relative magnitudes of sample thickness (l), thermal diffusion length ($\mu_s = 1/a_s$), and optical absorption length ($\mu_\beta = 1/\beta$). Three of these special cases deal with thermally thick sample. Either the thermally thick assumption ($\mu_s \ll l$) or the thermally thin assumption ($\mu_s \gg l$) permit simplification of the general result. The thermally thin limiting condition has much less general analytical applicability because it is difficult to achieve experimentally for many materials. Only the thermal thick limiting case will be considered. The three special cases for thermally thick samples are summarized in Table 2.2. For optically transparent sample the signal amplitude is predominantly due to light absorbed within the first thermal diffusion length and that the magnitude of the complex response function, Q , is proportional to the optical absorption coefficient times this length. Rosencwaig and Gersho suggest that this relationship is also approximately true for optically opaque samples as long as $\mu_\beta > \mu_s$, but that when $\mu_\beta < \mu_s$ the signal originates predominately from the first optical absorption length and Q becomes independent of the optical absorption coefficient. At this point the signal is saturated.

The Rosencwaig-Gersho special cases are useful for understanding the dependence of the photoacoustic response on the optical absorption coefficient; however, for quantitative applications they are as much an oversimplification as the general

EXPERIMENTAL PROCEDURES

Table 2.2 Rosencwaig-Gersho special case for thermally thick samples

Special cases	Photoacoustic signal
Optically transparent $(\mu_s \ll l < \mu_\beta)$	$Q \propto -i\beta\mu_s$
Optically opaque $(\mu_s < \mu_\beta < l)$	$Q \propto -i\beta\mu_s$
Photoacoustically opaque $(\mu_\beta < \mu_s \ll l)$	$Q \propto (1 + i)$

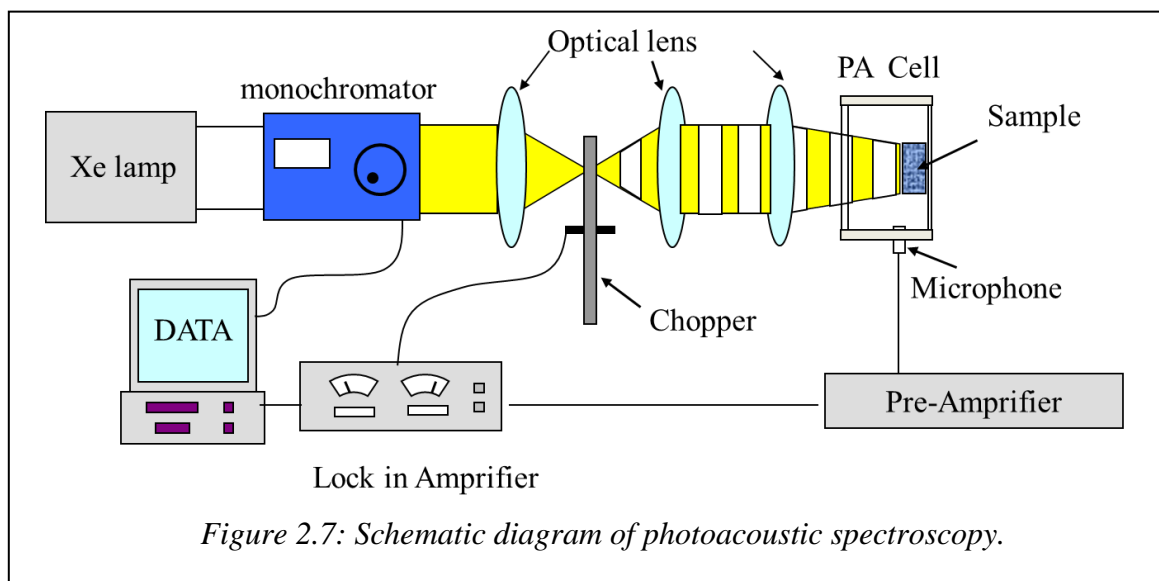


Figure 2.7: Schematic diagram of photoacoustic spectroscopy.

solution is complex. An alternative presentation of their result is useful in quantitative applications.

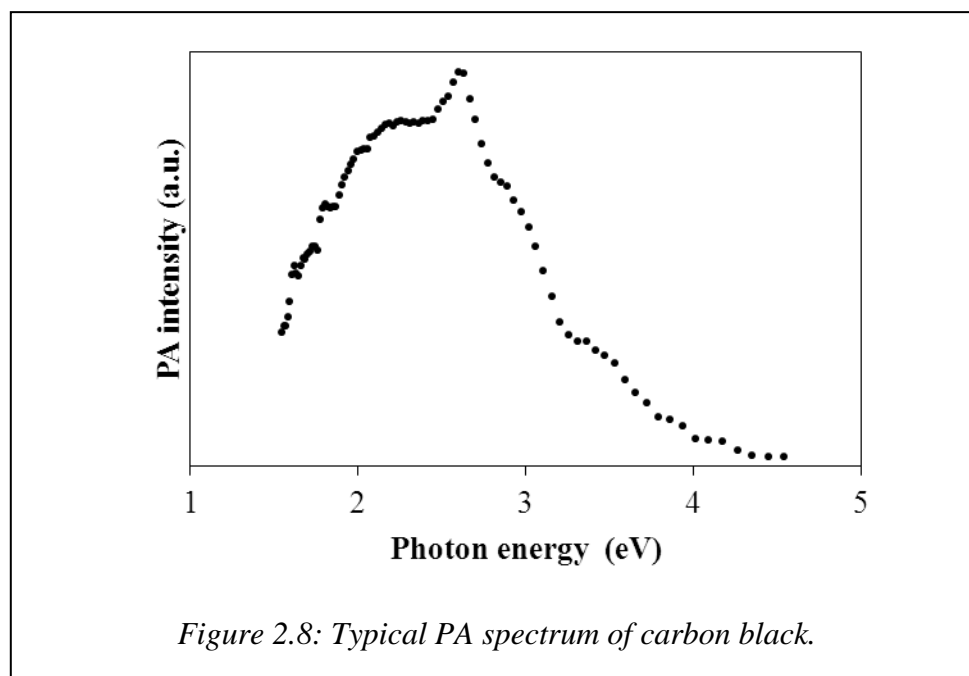
Figure 2.7 shows a system for solid state photoacoustic spectroscopy. A high-powered arc discharge lamp (i.e. Xe lamp) is used as the source of illumination and a scanning grating monochromator is used to achieve the spectral desired. A mechanical chopper modulates the monochromated light. Optical lenses are used for focusing. The PA cell hand-crafted from aluminum is a gas tight cell equipped with a microphone for signal detection. Quartz glass was used for the windows (since it is optically transparent

EXPERIMENTAL PROCEDURES

in the short wavelength region). The sample is placed in the airtight cavity. In the presence of modulated light, the gas inside the cavity (air) is periodically heated. This causes slight changes in pressure inside the cell that is detected as an audible signal. The microphone detects this signal and it is amplified and stored in the computer. The reference sample used for normalization is a black absorber (carbon black sheet) to eliminate the spectral variations of the illumination source. Shown in Fig. 2.8 is a typical spectrum of a carbon black sheet.

2.2.4 Incident photon to current efficiency spectroscopy [8]

The incident photon to current efficiency (IPCE) is the ratio of injected electron numbers to incident photon numbers which indicate the quantum yield for electron injection from the excited sensitizer (in this study: CdSe quantum dots) to the conduction band of the semiconductor (TiO_2) and the collection efficiency of the electron to the



EXPERIMENTAL PROCEDURES

back-contact (FTO). Therefore, the area of the IPCE curve can be directly converted into short circuit current density when considering light harvesting efficiency and light flux.

In order to understand a solar cell's photocurrent response for a specific wavelength, it is necessary to know the number of incident photon at the wavelength. A photodiode with known spectral responsivity was used to calculate the number of photons per wavelength in the light source. This photodiode produced a photocurrent output when exposed to light from the monochromator, as the monochromator performed a wavelength sweep in 6 nm increments from 270 nm to 800 nm. The energy of incident photons E was calculated using the following formula:

$$E = \frac{hc}{\lambda} \quad (2.18)$$

where h is Planck's constant, c is the speed of light, and λ is the wavelength of the photon. The number of photons from the monochromator at a given wavelength can then be calculated as follow:

$$\text{Incident photon numbers at a given wavelength} = \frac{i}{E} \quad (2.19)$$

where i is light intensity at a given wavelength. It is possible to find the incident photon to converted electron ratio of a solar cell. The number of electrons generated per second while under illumination from the monochromator for a given wavelength was found to be:

$$\text{Injected electron numbers} = \frac{\text{Photocurrent}}{q} \quad (2.20)$$

where q is electron charge.

IPCE or incident photon to current efficiency which corresponds to the quantum efficiency is calculated from Eq. 2.18.

$$IPCE(\%) = \frac{\text{Injected electron numbers}}{\text{Incident photon numbers}} \times 100 = \frac{1240 \times I_{sc}}{\lambda \times P} \times 100 \quad (2.21)$$

I_{sc} is the measured short current density (mA), P is the incident light power (mW) and λ is wavelength of incident light (nm).

EXPERIMENTAL PROCEDURES

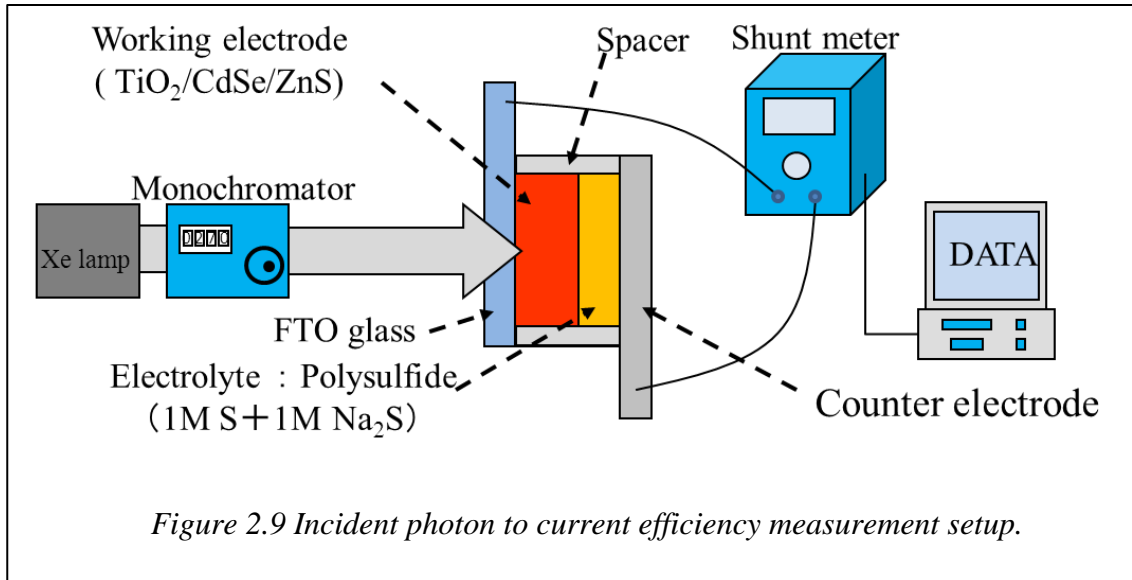


Figure 2.9 shows the schematic diagram of IPCE spectrometer. In IPCE spectroscopy, a xenon lamp with power supply, monochromator and ammeter were used for the IPCE measurement. To measure photocurrent response, an incandescent bulb was used to shine white light through the monochromator. This monochromator use a rotating diffraction grating to produce monochromatic light. The incident light is directly focused on the sample produced a current response, without modulation through chopper. The amplitude of this signal is the photocurrent. The intensity of incident light is calibrated using power meter and the distribution of incident light is obtained by using photoacoustic spectrum of carbon.

2.2.5 Power conversion efficiency measurement [9]

The photovoltaic performances or J - V characteristics of solar cells are characterized using solar simulator. There are four basic parameters to test the performance of the cells. First, the open circuit voltage, V_{oc} , is defined as the voltage between the cell terminals (cathode and anode) when no current flows in the external circuit. V_{oc} is determined from the intercept of the light J - V curve with the voltage axis ($J = 0$). Second, the current density of the illuminated cell with directly connected terminals

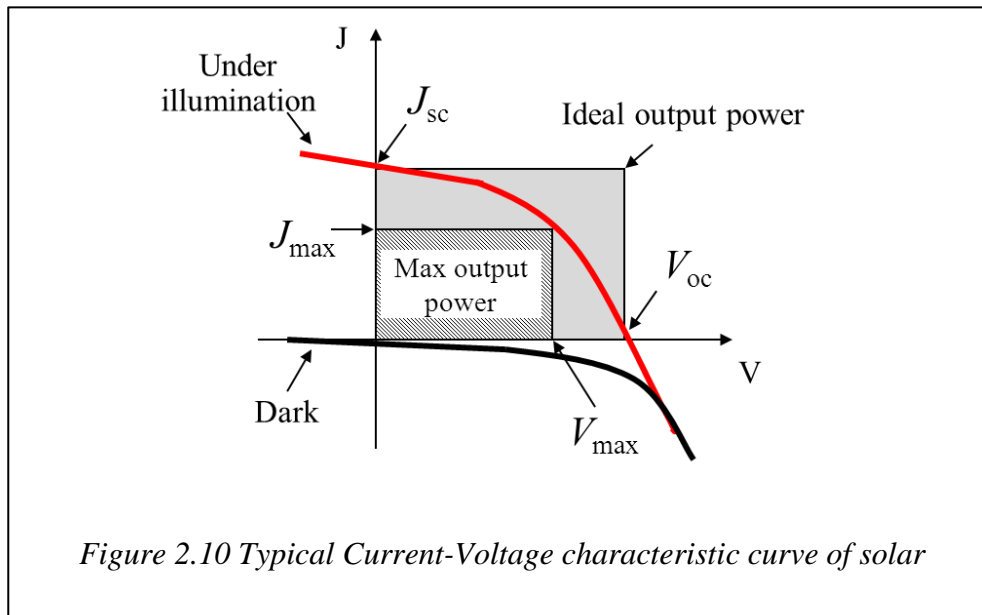
EXPERIMENTAL PROCEDURES

(no external voltage is applied) is called the short circuit current density, J_{sc} . It is the intercept of the light J - V curve with the current density axis ($V = 0$), as shown in Figure 2.10. The third parameter is called the fill factor (FF). It measures the coincidence of the maximum power point P_{max} with the value of multiplying V_{oc} by J_{sc} .

$$FF = \frac{P_{max}}{J_{sc} \times V_{oc}} = \frac{J_{max} \times V_{max}}{J_{sc} \times V_{oc}} \quad (2.20)$$

where V_{max} and J_{max} are the voltage and the current density corresponding to P_{max} .

Fig. 2.10 shows typical current-voltage characteristic curve of solar cell. The fill factor does not depend on the area of the cell and is essentially a measure of quality of the solar cell. FF can be expressed as the ratio between the rectangle defined by the gray area and the rectangle defined by the diagonally striped area depicted in Fig. 2.10. The maximum value of the FF is 100 %, which means that the J - V curve is a perfect rectangular at the first quarter of the J - V plot. The last parameter is the power conversion efficiency, η . It evaluates the ratio between the maximum power generated by the cell to the power of the incident light P_{in} . AM1.5 spectrum (which results in $P_{in} = 100 \text{ mW/cm}^2$)

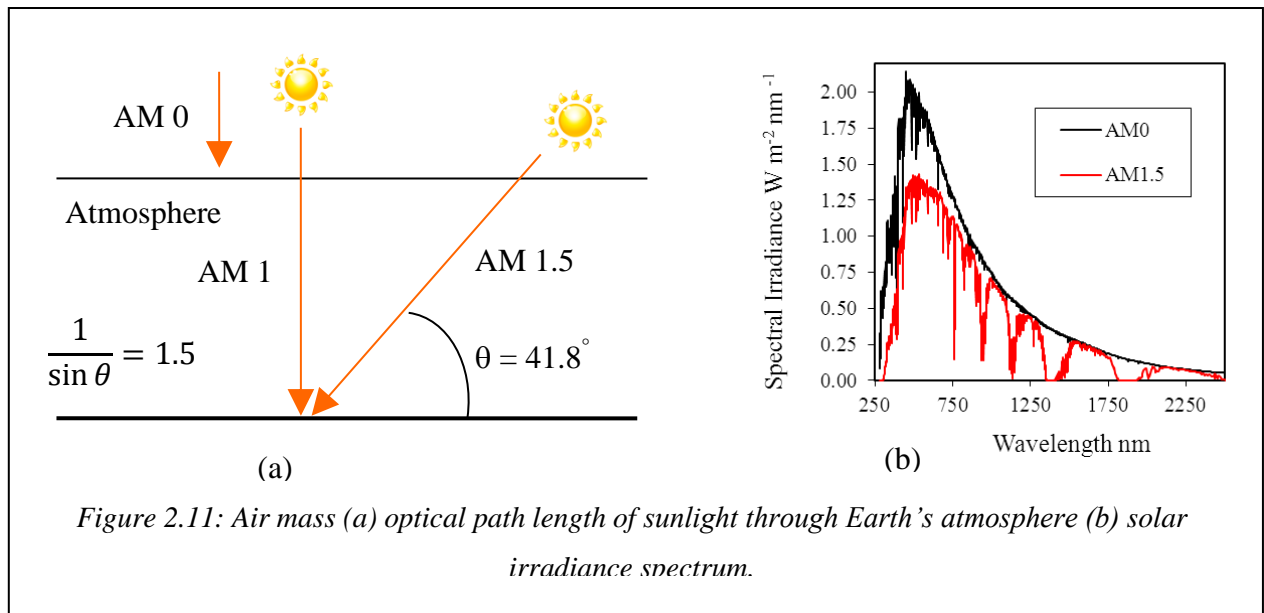


EXPERIMENTAL PROCEDURES

is the typical spectrum under which η is measured. Therefore, the power conversion efficiency is expressed as

$$\eta(\%) = \frac{P_{max}}{P_{in}} = \frac{J_{sc} \times V_{oc} \times FF}{P_{in}} \times 100 \quad (2.21)$$

The most frequently used experimental conditions are the irradiance of 100 mW/cm², which is defined as the standard 1 sun value with spectrum consistent to an air mass (AM) global value of 1.5 at ambient temperature 25°C. AM1.5 is a standard reference solar spectral irradiance after the solar radiation has traveled through the atmosphere with the Sun at an altitude angle of 41.8°, which simulates a longer optical path through the Earth's atmosphere relative to the Sun at zenith above the Earth's atmosphere (AM1), as shown in Fig. 2.11. The use of this standard irradiance value is almost universally used to characterize terrestrial solar panels and particularly convenient because the cell efficiency in percent is then numerically equal to the power output from the cell in mW/cm².



References

- [1] L. J. Diguna, Q. Shen, J. Kobayashi, and T. Toyoda, *Appl. Phys. Lett.* **91**, 023116 (2007).
- [2] V. Vogel, K. Pohl, and H. Weller, *Chem. Phys. Lett.* **174**, 241 (1990).
- [3] H. Lee, H. C. Leventis, S. Moon, P. Chen, S. Ito, S. A. Haque, T. Torres, F. Nuesch, T. Geiger, S. M. Zakeeruddin, M. Gratzel, and K. Nazeeruddin, *Adv. Funct. Mater.* **19**, 2735 (2009).
- [4] J. Goldstein, D. E. Newbury, D. C. Joy, and C. E. Lyman, *Scanning Electron Microscopy and X-ray Microanalysis*, 3rd ed. (Kluwer Academic/Plenum Publishers, New York, 2003).
- [5] C. Hammond, *The basics of crystallography and diffraction* (Oxford University Press, New York, 1997).
- [6] B. D. Cullity, *Elements of X-Ray Diffraction*, 2nd ed. (Addison-Wesley Publishing Co. Inc., 1978).
- [7] A. C. Tam, *Rev. Mod. Phys.* **58**, 381 (1996).
- [8] R. Brendel, *Thin-film Crystalline Silicon Solar Cells* (Wiley-VCH, Weinheim, 2003).
- [9] S. J. Fonash, *Solar cell device physics* (Academic Press, Boston, 2010).

Optical absorption characterization of CdSe QD on TiO₂

3.1 Introduction

Dye-sensitized solar cells (DSSCs) built on titanium dioxide (TiO₂) nanostructure have been receiving significant attention by reason of their high photovoltaic conversion efficiencies, often exceeding 11% [1,2]. DSSCs are relatively inexpensive to fabricate compared with conventional silicon based solar cells. In addition to organic dyes, quantum dots (QDs) of various semiconductors, such as CdS, CdSe and PbS, have also attracted significant interest as solar cell sensitizers. The usage of semiconductor QDs as sensitizers has several benefits in solar cell applications [3-6]. Firstly, by manipulating QDs' size, the energy gap of the QDs can be adjusted to cover a large fraction of the solar spectrum [7]. Secondly, semiconductor QDs have a large extinction coefficient owing to quantum confinement and the large intrinsic dipole moment, which can lead to rapid charge separation [8]. Thirdly, they have the potential for multiple exciton generation (MEG) [9,10], which can potentially increase the efficiency of photovoltaic devices [9-12]. As for present photovoltaic devices, there is a maximum thermodynamic energy conversion efficiency of about 31% calculated by the Shockley-Queisser detailed balance limit [13]. When MEG is incorporated into the calculations, the value of the maximum thermodynamic energy conversion efficiency is able to push up to 44% [14]. Although, the performance of quantum dot-sensitized solar cells (QDSSCs) is still below DSSCs

OPTICAL ABSORPTION CHARACTERIZATION OF CdSe QD ON TiO₂

(the reported maximum conversion efficiency of QDSSCs is ~5% at present), QDSSCs are attracting increasing attention among researchers, and progress is very rapid [15-19]

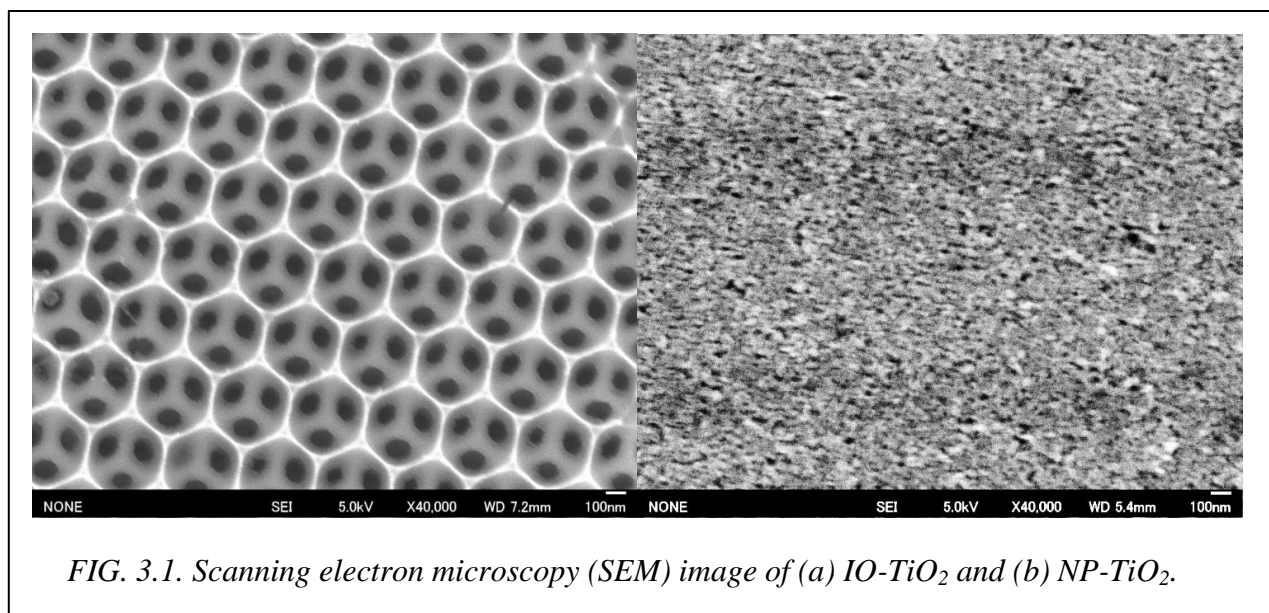
The QDs are grown directly on the surface of a TiO₂ electrode by the chemical reaction of ionic species using either chemical bath deposition (CBD) [3,4] or a successive ionic layer adsorption and reaction (SILAR) method [20,21]. However, CBD on a porous substrate tends to block the pores in the structure. By comparison with CBD, the thin films in the SILAR method are grown ion-by-ion by the absorption and reaction of ions in different solutions that excludes the formation of clusters. The SILAR method involves nucleation and growth mechanisms, and provides high coverage of the electrode leading to a polydisperse QD size distribution. Furthermore, the SILAR method does not require precise control of the concentration of ions, the pH value, nor the temperature [22].

There are several factors that assist to improve the performance of QDSSC; (1) pore structure of TiO₂ electrode for a higher covering of QDs, (2) a surface passivation of TiO₂ to reduce recombination, and (3) improved counter electrode materials. Also, the TiO₂ electrode morphology is important for achieving reliable assembly [6,23]. In DSSCs, the working-electrode should have a high surface area to increase the amount of sensitizer loading in order to enhance light harvesting because of the limitation of the dye adsorption on TiO₂ as single monolayer [24]. However, the recombination process is proportional to the surface area of the electrode. The surface area for QDSSCs may not need to be increased by as much as for DSSCs, because the QD has higher extinction coefficient and the QDs are not limited to a single molecular monolayer as are the dyes. A balance between recombination and light harvesting is needed to maximize the sensitized solar cell performance. To resolve the penetration of redox couples to sensitizers, a method using an inverse opal TiO₂ electrode (IO-TiO₂) has been suggested. IO-TiO₂ has a honeycomb structure with large interconnected pores that leads to better infiltration, despite the smaller surface area compared to nanoparticulate electrodes [25].

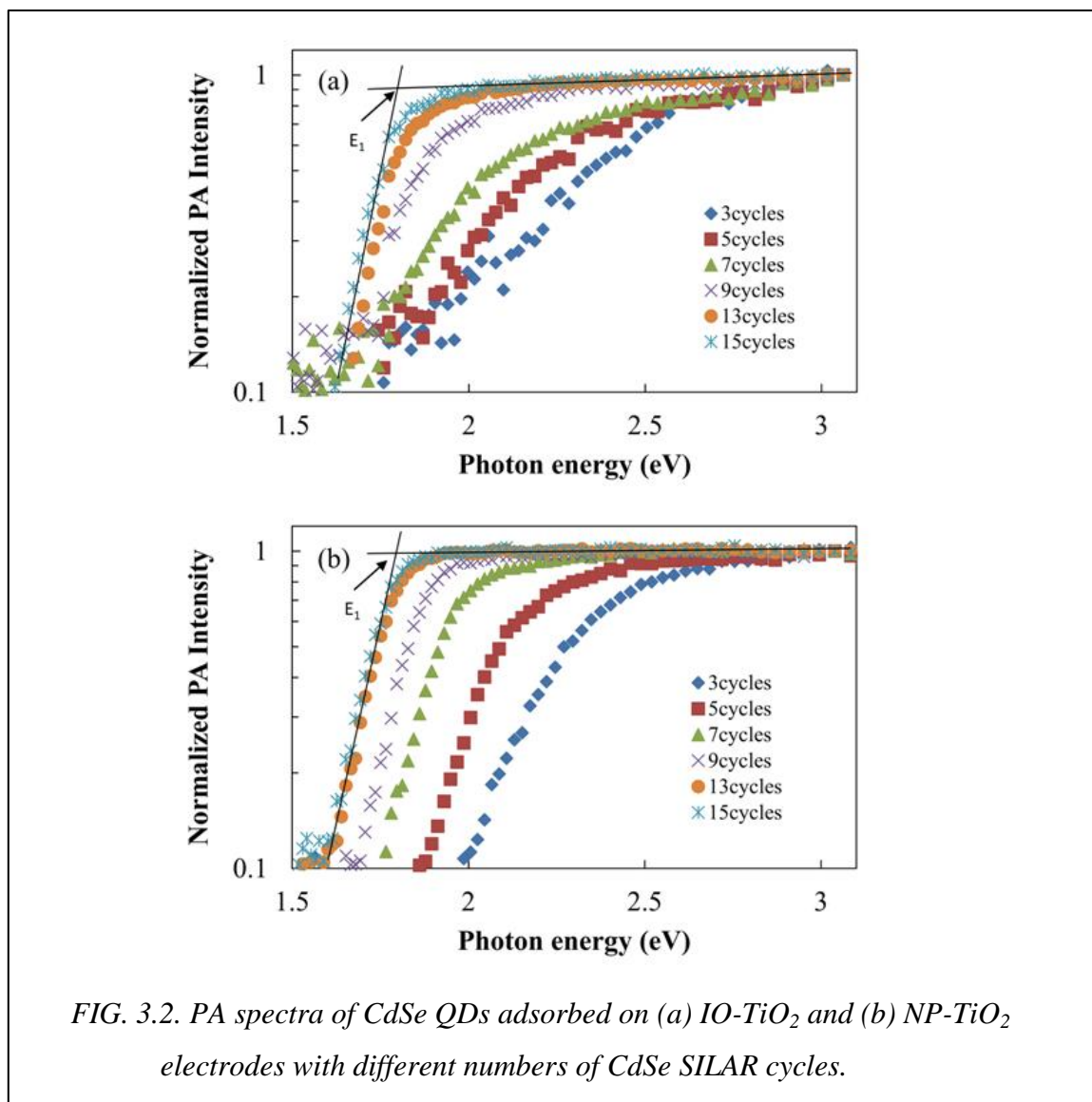
To date, the SILAR process has been applied to the preparation of CdSe QDs [20,21]. Among semiconductors, CdSe is well known as a sensitizer for QDSSCs because of its high light harvesting in the visible region. However, deposition of CdSe QDs by the SILAR method on IO-TiO₂ has not yet been reported. In this study, we investigated the effect of the number of SILAR cycles on the optical absorption properties of CdSe QDs on IO-TiO₂ electrodes. SILAR method was used to adsorb CdSe QDs not only on the IO-TiO₂, but also on a nanoparticulate TiO₂ electrode (NP-TiO₂) for comparison. The optical absorption properties were characterized using a gas-microphone photoacoustic (PA) technique [26]. This is a photothermal detection method that has developed to be useful for examining the optical absorption and thermal properties of several materials by evaluating nonradiative de-excitation processes. PA method is especially useful for optical scattering and opaque samples [19,26]

3.2 Experimental

The preparation method for IO-TiO₂ has been reported in a previous study[27]. Fluorine-doped tin oxide (FTO) covered glass was ultrasonically cleaned in detergent, KOH, distilled water and methanol. An uniform polystyrene (PS) latex suspension (474 nm in diameter) was agitated by ultrasound for 30 min to split aggregated particles. The fabricated opal samples were prepared by dipping the FTO substrate vertically in a 0.1 wt.% monodisperse PS suspension and evaporated leaving a colloidal PS template on the substrate. Hydrolysis process was then performed with a 10- μ l droplet of 2% TiCl₄ in methanol was put into the colloidal surface for 30 min. After that, the sample was then



baked to 80°C under the air. This procedure was repeated three times to make certain the permeation of all voids. Finally, the sample was subsequently baked at 450°C for 1 h under the air to remove the template and anneal the TiO₂. The scanning electron microscopy (SEM) image shown in Fig 3.1 (a) shows IO-TiO₂ electrode in which the honeycomb structure can be observed with a period of 380 nm. The IO-TiO₂ thickness was measured as 3 μm using a contact profilometer (DEKTAK, ULVAC). NP-TiO₂ was fabricated using a method described in a previous report [28]. To fabricate NP-TiO₂, TiO₂ pastes were made by combination of 15 nm TiO₂ nanoparticles (Super Titania, Showa Denko, anatase structure) and polyethylene glycol (molecular weight 500 000) in distilled water. The prepared pastes were applied onto FTO substrates (10 Ω/square; that is unit of sheet resistance) using the doctor blade method, followed by sintering at 450 °C for 30 min. The NP-TiO₂ thickness was found to be 3 μm. A SEM image of the NP-TiO₂ is shown in Fig. 3.1(b). In the case of NP-TiO₂ electrode, we chose 15 nm of NP-TiO₂ because previous study in our group found that the size of the TiO₂ was the optimal condition for QDSSC [28,29]. Then, both conditions were compared.



The CdSe QDs were adsorbed on the TiO₂ electrodes in a nitrogen atmosphere using the SILAR method [20]. The TiO₂ electrode was immersed sequentially into two different solutions for about 30 s each. One solution contained 0.03 M Cd(NO₃)₂ dissolved in ethanol and the other solution consisted of 0.03 M SeO₂ and 0.06 M NaBH₄ in ethanol. Following immersion, the films were rinsed for 1 min using pure ethanol to remove excess precursor, and the electrode was dried before the next dipping. This immersion cycle was repeated several times from 3 to 15 cycles in order to investigate the

effect of the number of SILAR cycles. Subsequently, the samples were coated with ZnS to prevent both photocorrosion and recombination processes between electron and hole on the surface. The SILAR method was used for this passivation coating, which was done by dipping the sample twice each in 0.1 Zn(CH₃COO)₂ and 0.1 M Na₂S for 1 min each immerse [30].

The optical absorption spectra of the TiO₂ electrodes adsorbed with CdSe QDs were measured by gas-microphone photoacoustic (PA) spectroscopy [19,26]. A 300-W xenon arc lamp was utilized as a light source. Monochromatic light was achieved by delivering light through a monochromator. This light was regulated with a mechanical chopper. The modulated light was focused onto the surface of the sample located inside the sealed PA cell. The light absorbed by the sample is changed into heat by a nonradiative relaxation process, which results in a pressure variation of the air inside the cell. The pressure variation is related to the optical absorption of the samples and it is identified as a PA signal by a microphone [26]. In this study, the PA spectrum measurements were performed in the wavelength region between 270 – 830 nm with a modulation frequency of 33 Hz at room temperature. The PA signal was observed by first passing the microphone output through a preamplifier and then pass to a lock-in amplifier. The spectra were calibrated by PA measurements from a carbon black sheet.

3.3 Results and discussion

Figure 3.2 shows the PA spectra of CdSe QDs adsorbed on (a) IO-TiO₂ and (b) NP-TiO₂ electrodes with different numbers of SILAR cycles. The spectra are normalized at 3.0 eV of a photon energy. In this experiment, the samples show light scattering and semi-transparent. Then, the PA method is applied for the light absorption. The PA theory is based on Rosencwaig and Gersho [26]. The PA signal (P) is proportional to optical absorption coefficient (α). The energy band gap determination from shoulder method in

the PA spectra was reported by Rosenwaig [31]. In the case of semiconductors, the shoulder in the PA spectra agree very well with the accepted value. Moreover, Prias-Barragan and et al. [32] reported values of the band gap obtained by PA techniques were good agreement with photoreflectance results. The band gap determined from the shoulder in PA spectra is the reasonable value. This is due to the higher sensitivity of PA signal intensity than conventional transmission measurements. In QDs, the PA shoulder can assume as well as a peak of absorption coefficient. However, the peak cannot obviously observe because of two reasons, that is, the broad shoulder is connected with

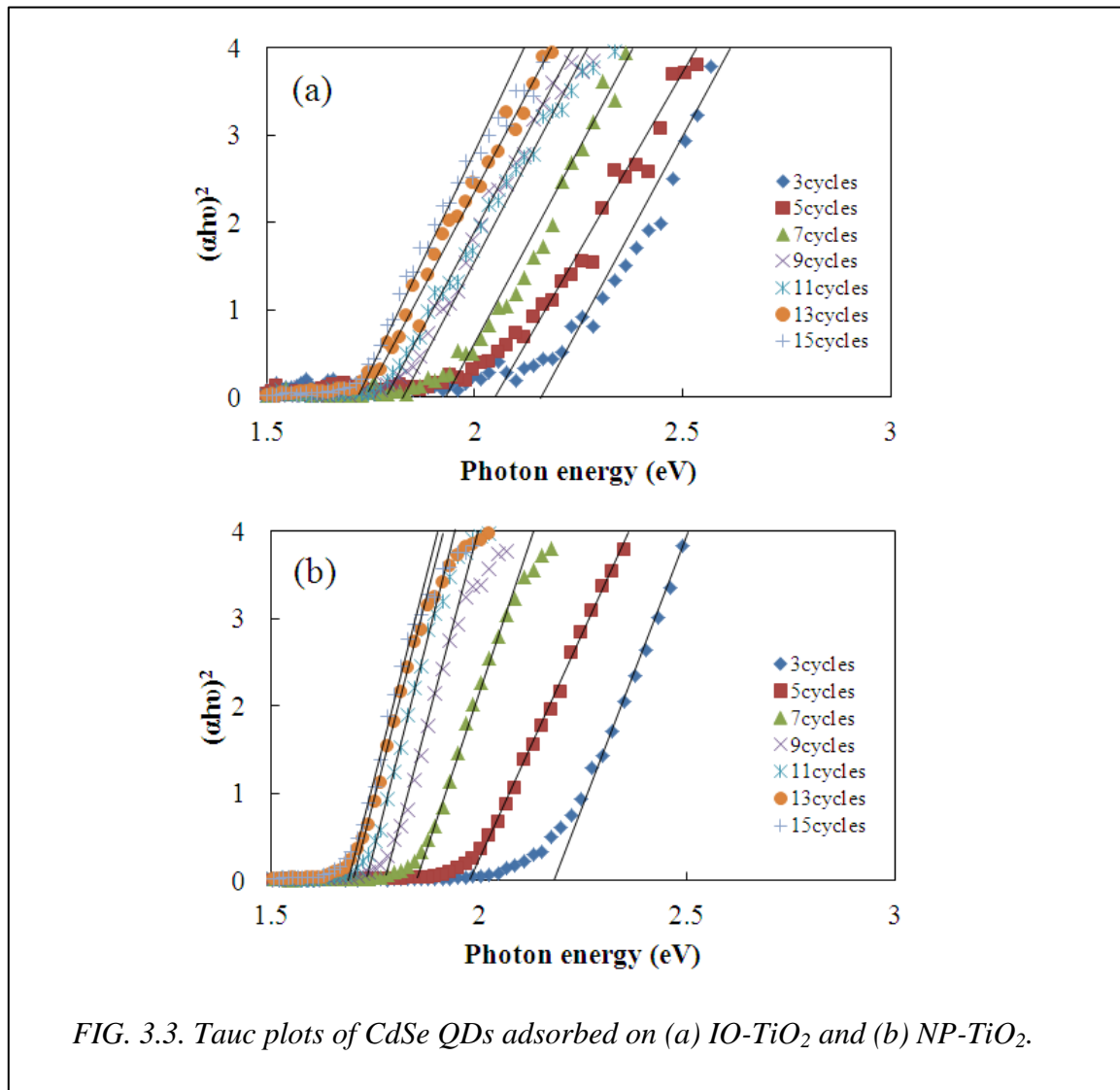
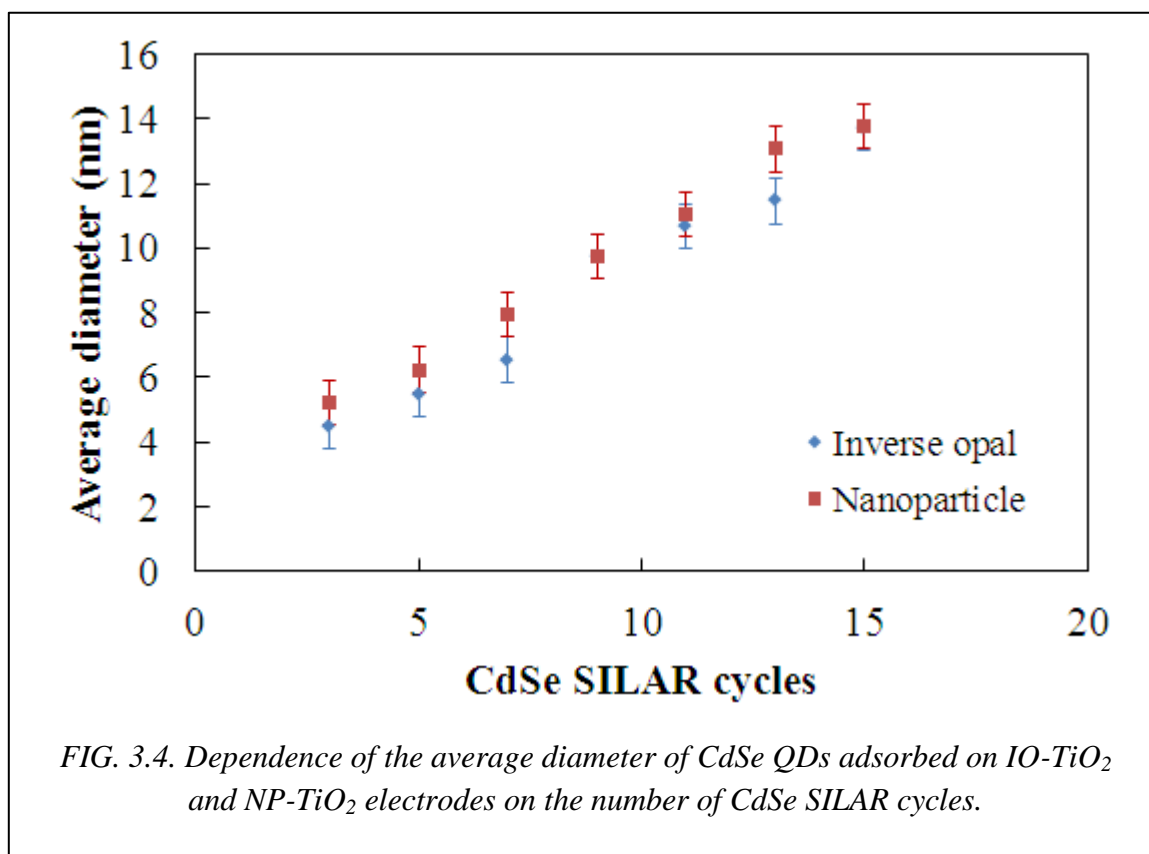


FIG. 3.3. Tauc plots of CdSe QDs adsorbed on (a) IO-TiO₂ and (b) NP-TiO₂.

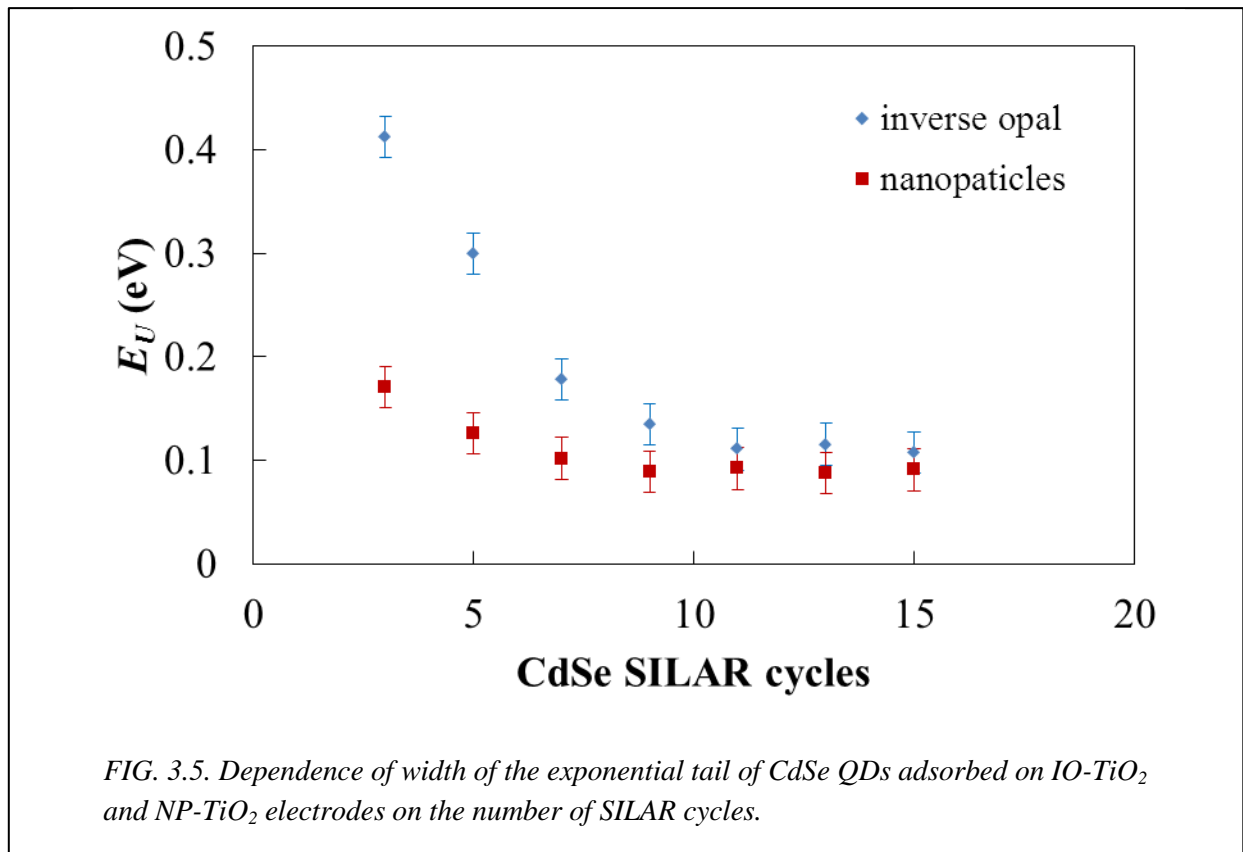
the size distribution of the QDs and acoustic saturation at the strong absorption side of the band gap region. With the increasing number of SILAR cycles, a redshift of the PA shoulder (E_1) can be noticed, indicating the growing of CdSe QDs. E_1 is assumed to be the first excitation energy of the CdSe QDs. Fig. 3.3 show Tauc plots of CdSe QDs adsorbed on (a) IO-TiO₂ and (b) NP-TiO₂, which optical band gap can estimate from the x-intercept of the line gives the optical band edge. The E_g values estimated from Tauc plot are similar to the PA shoulder. The average diameter was estimated by using the effective mass approximation (EMA) [33]. The EMA derives from the crystal potential as a spherical well of infinite depth. The EMA fails for the small crystal size because of the finite potential step at the crystalline surface. Murray et al [34] showed that calculating CdSe QD size using EMA agreed with experimental results, in the case that QD size was



OPTICAL ABSORPTION CHARACTERIZATION OF CdSe QD ON TiO₂

over ~4 nm in diameter. In our results, the calculated diameters were about 4-12 nm, therefore they were in an acceptable range. Figure 3.4 shows the dependence of the average diameter of the QDs adsorbed on the IO-TiO₂ and NP-TiO₂ electrodes on the number of CdSe SILAR cycles. Above 3 cycles, the growth rates of the QDs on each type of electrode are similar (~0.8 nm/cycle), indicating that the growth rate is independent of the electrode morphology, unlike the case for CBD [23]. With the SILAR method [35], the TiO₂ substrate is first immersed in a cationic precursor solution containing Cd²⁺ ions. The Cd²⁺ ions nucleate at active sites on the surface where the ions can be adsorbed. Then, the substrate is immersed in an anionic precursor solution containing Se²⁻ ions. The Se²⁻ ions reach the surface and react with the adsorbed Cd²⁺ ions to form CdSe QDs. For comparison, CdSe with a zinc blende structure has a lattice constant of 0.60 nm, thus Cd-Se spacing is about 0.3 nm [36]. The Se²⁻ ions are adsorbed on the Cd²⁺ in single layers, so the size of the QDs should increase by the Cd-Se spacing in the relevant direction for each SILAR cycle. However, the increase in size with each SILAR cycle is ~0.8 nm, which is greater than the Cd-Se spacing, showing that more than one layer is adsorbed during the 30s immersions in the precursor solutions since the rinsing process does not fully remove the free ions. In the case of the CBD method[23], the CdSe QD diameter increases and shows a saturation with increasing adsorption time, due to normal growth from the solution but with suppression (negative growth or dissolution) of the CdSe QD crystal growth. Suppression of the crystal growth does not occur with the SILAR method. Thus, crystal growth with the SILAR method can be easily controlled by changing the number of deposition cycles. However, the amount of CdSe QDs on NP-TiO₂ is greater than that on IO-TiO₂, which was confirmed by measuring the optical absorbance of the CdSe QDs on IO- TiO₂ and NP-TiO₂. In the photon energy region between 2 and 3 eV, which is higher than the energy of the first excited state of CdSe QDs, the optical absorbance of the CdSe QDs on the IO-TiO₂ is approximately one quarter of that of the CdSe QDs on NP-TiO₂. Furthermore, BET surface area measurements were carried out.

(Brunauer–Emmett–Teller (BET) theory explains the physical adsorption of gas molecules on a solid surface and serves as the basis for an important analysis technique for the measurement of the specific surface area of a material.) The BET surface area of IO-TiO₂ is 44 m²/g, which is half that of NP-TiO₂ (80 m²/g). This indicates that IO-TiO₂ has fewer growth nuclei than NP-TiO₂. The number of growth nuclei on the surface ($N(t)$) can be expressed as a function of time, by $N(t) = N_0[1 - \exp(-At)]$ [35], where A , which depends on the activation energy, is the probability that an active site (a preliminary stage which can develop into a QD) will transform into a growth nucleus, and N_0 , which depends on the surface structure of the TiO₂, is the number of active sites on the surface at the beginning of the QD formation process. The growth nuclei are the initial sites for the growth of QDs, and the number of QDs depends on the number of these nuclei. Both IO-TiO₂ and NP-TiO₂ are immersed in the precursor solution for 30 s. The immersion



time is a control condition for both IO-TiO₂ and NP-TiO₂. There is a possible reason why IO-TiO₂ has fewer growth nuclei than NP-TiO₂. IO-TiO₂ has fewer active sites than NP-TiO₂, so there is less adsorption of Cd²⁺ ions on the surface in the first stage. On the TiO₂ surface, two coordinating O²⁻ anions, which are next to two Ti neighbors, have one degree of coordinative unsaturation, making them able to react and bond with Cd²⁺ ions. These two coordinating O²⁻ anions on the TiO₂ surface behave as an active site for Cd²⁺, and this depends on the morphology, as reported [37]. The surfaces of IO-TiO₂ and NP-TiO₂ exhibit different structural arrangements, with different surface reactivities and numbers of O²⁻ anions. This suggests that the O²⁻ centers exposed on the surface of IO-TiO₂ are quite distant from each other.

In the experiments, the PA intensity is proportional to the optical absorption coefficient of the electrode [26]. The PA intensities plotted semi-logarithmically change linearly below the PA shoulder (absorption edges) in correspondence with the Urbach rule for the optical absorption coefficient (exponential tail). Investigation of these exponential tails can afford data on the band structure, the disorder, defects, impurities, and electron-phonon interactions. An experimental relationship for the dependency of the PA signal intensity of the exponential tail on photon energy ($h\nu$) is defined by

$$P = P_0 \exp\left(\frac{h\nu - h\nu_0}{E_u}\right), \quad (3.1)$$

where h is Planck's constant, and P_0 , ν_0 , E_u are fitting parameters [38]. The width of the exponential tail E_u is an inverse logarithmic slope of absorption below the first excitation energy. We assume that the value of E_u is a reflection of the disorder in the semiconductor crystal [39]. Thus, when the number of defects increases, the width of the exponential tail in the region below the first excitation energy also increases. Figure 3.5 shows the dependence of E_u for CdSe QDs on IO-TiO₂ and NP-TiO₂ on the number of SILAR cycles, which the value of E_u was estimated from logarithmic PA intensity in Fig. 3.2. The value of E_u decreases with the number of SILAR cycles for both IO-TiO₂ and

NP-TiO₂, indicating a decrease in disorder. The value of E_u for CdSe QDs on IO-TiO₂ is higher than that for NP-TiO₂, indicating that the CdSe QDs on IO-TiO₂ have greater disorder than those on NP-TiO₂. The size of the QDs on IO-TiO₂ are similar to those on NP-TiO₂, so the surface to volume ratios are similar to each other, indicating that the disorder in IO-TiO₂ is higher than in NP-TiO₂. Above 9 SILAR cycles on both IO-TiO₂ and NP-TiO₂, E_u approaches a constant value because, as the size of the QDs increases, their surface area decreases due to the increasing boundaries between them.

3.4 Conclusions

We used PA spectroscopy to study the optical absorption of CdSe QDs adsorbed on IO-TiO₂ and NP-TiO₂ electrodes. CdSe QDs were grown directly on IO-TiO₂ and NP-TiO₂ by the SILAR method with from 3 to 15 SILAR cycles. The growth of the CdSe QDs on the electrodes was estimated from the PA spectra. The growth rates of the QDs on IO-TiO₂ and NP-TiO₂ were similar, indicating that this is independent of morphology. However, measurements of the optical absorbance showed there were more CdSe QDs on NP-TiO₂ than on IO-TiO₂, indicating that there were a greater number of active sites on NP-TiO₂ than on IO-TiO₂. The width of the exponential tail, E_u , of CdSe QDs on IO-TiO₂ was higher than that on NP-TiO₂, indicating that the CdSe QDs on IO-TiO₂ had more disorder than NP-TiO₂. Above 9 SILAR cycles in both cases, E_u tended to move towards a constant value because the amount of disorder is dominant.

Reference

- [1] Y. Chiba, A. Islam, Y. Watanabe, R. Koyama, N. Koide and L. Han, *Jpn. J. Appl. Phys.* **45**, L638 (2006).
- [2] M. A. Green, K. Emery, Y. Hishikawa, W. Warta and E. D. Dunlop, *Prog. Photovolt: Res. Appl.* **20**, 12 (2012).
- [3] C. H. Chang and Y. L. Lee, *Appl. Phys. Lett.* **91**, 053503 (2007).
- [4] L. J. Diguna, Q. Shen, J. Kobayashi and T. Toyoda, *Appl. Phys. Lett.* **91**, 023116 (2007).
- [5] H. Lee, H. C. Leventis, S. Moon, P. Chen, S. Ito, S. A. Haque, T. Torres, F. Nuesch, T. Geiger, S. M. Zakeeruddin, M. Grätzel and M. K. Nazeeruddin, *Adv. Funct. Mater.* **19**, 2735 (2009).
- [6] T. Toyoda and Q. Shen, *J. Phys. Chem. Lett.* **3**, 1885 (2012).
- [7] N. Guijarro, Q. Shen, S. Giménez, I. Mora-Seró, J. Bisquert, T. Lana-Villarreal, T. Toyoda and R. Gómez, *J. Phys. Chem. C* **114**, 22352 (2010).
- [8] D. F. Underwood, T. Kippenny and S. J. Rosenthal, *Eur. Phys. J. D* **16**, 241 (2001).
- [9] A. J. Nozik, *Physica E* **14**, 115 (2002).
- [10] V. I. Klimov, *J. Phys. Chem. B* **110**, 16827 (2006).
- [11] R. D. Schaller, M. Sykora, J. M. Pietryga and V. I. Klimov, *Nano Lett.* **6**, 424 (2006).
- [12] A. J. Nozik, *Chem. Phys. Lett.* **3**, 457 (2008).
- [13] W. Shockley and H. J. Queisser, *J. Appl. Phys.* **32**, 510 (1961).
- [14] M. C. Beard, K. P. Knutsen, P. Yu, J. M. Luther, Q. Song, W. Metzger, R. J. Ellingson and A. J. Nozik, *Nano Lett.* **7**, 2506 (2007).
- [15] Q. Niitsoo, S. K. Sarkar, P. Pejoux, S. Rühle, D. Cahen and G. Hodes, *J. Photochem. Photobiol. A* **181**, 306 (2006).

- [16] A. Kongkanand, K. Tvrdy, K. Takechi, M. Kuno and P. V. Kamat, *J. Am. Chem. Soc.* **130**, 4007 (2008).
- [17] Q. Shen, A. Yamada, S. Tamura and T. Toyoda, *Appl. Phys. Lett.* **97**, 123107 (2010).
- [18] V. González-Pedro, X. Xu, I. Mora-Seró and J. Bisquert, *ACS Nano* **4**, 5788 (2010).
- [19] T. Toyoda, K. Oshikane, D. Li, Y. Luo, Q. Meng and Q. Shen, *J. Appl. Phys.* **108**, 114340 (2010).
- [20] H. Lee, M. Wang, P. Chen, D. R. Gamelin, S. M. Zakeeruddin, M. Grätzel and M. K. Nazeeruddin, *Nano Lett.* **9**, 4221 (2009).
- [21] J. J. Li, Y. A. Wang, W. Guo, J. C. Keay, T. D. Mishima, M. B. Johnson and X. Peng, *J. Am. Chem. Soc.* **125**, 12567 (2003).
- [22] L. Yin and C. Ye, *Sci. Adv. Mater.* **3**, 41 (2011).
- [23] T. Toyoda, T. Uehata, R. Suganuma, S. Tamura, A. Sato, K. Yamamoto, Q. Shen and N. Kobayashi, *Jpn. J. Appl. Phys.* **46**, 4616 (2007).
- [24] M. Grätzel, *J. Photochem. Photobiol. C* **4**, 145 (2003).
- [25] P.R. Somani, C. Dionigi, M. Murgia, D. Palles, P. Nozar, G. Ruani, *Sol. Energy Mater. Sol. Cells* **87**, 513 (2005).
- [26] A. Rosencwaig and A. Gersho, *J. Appl. Phys.* **47**, 64 (1976).
- [27] L. J. Diguna, M. Murakami, A. Sato, Y. Kumagai, T. Ishihara, N. Kobayashi, Q. Shen and T. Toyoda, *Jpn. J. Appl. Phys.* **45**, 5563 (2006).
- [28] Q. Shen and T. Toyoda, *Thin Solid Films* **167**, 438 (2003).
- [29] Q. Shen, J. Kobayashi, L. J. Diguna, and T. Toyoda, *J. Appl. Phys.* **103**, 084304 (2008)
- [30] S. M. Yang, C. H. Huang, J. Zhai, Z. S. Wang and L. Liang, *J. Mater. Chem.* **12**, 1459 (2002).
- [31] A. Rosencwaig, *Phys. Today* **28**, 23 (1975).

- [32] J.J. Prías-Barragán, L. Tirado-Mejía, H. Ariza-Calderón, L. Baños, J.J. Perez-Bueno, and M.E. Rodríguez, *J. Cryst. Growth* **286**, 279 (2006).
- [33] A. I. Ekimov, A. L. Efros and A. A. Onushchenko, *Solid State Commun.* **56**, 921 (1985).
- [34] C. B. Murray, D. J. Norris and M. G. Bawendi, *J. Am. Chem. Soc.* **115**, 8706 (1993), V. N. Soloviev, A. Eichhofer, D. Fenske and U. Banin, *J. Am. Chem. Soc.* **122**, 2673 (2000).
- [35] H. M. Pathan and C. D. Lokhande, *Bull. Mater. Sci.* **27**, 85 (2004).
- [36] R. Solanki, J. Huo and J. L. Freeouf, *Appl. Phys. Lett.* **81**, 3864 (2002).
- [37] G. Martra, *Applied Catalysis A: General* **200**, 275 (2000).
- [38] T. H. Keil, *Phys. Rev.* **144**, 582 (1966).
- [39] S. Knief and W. Niessen, *Phys. Rev. B* **59**, 12940 (1999).



Photovoltaic properties of CdSe QD on TiO₂

4.1 Introduction

One of the major renewable energy sources, solar energy has the potential to become an essential component of future global energy production. Dye-sensitized solar cells (DSSCs) based on nanostructured TiO₂ electrodes have been attracting much attention as an alternative to conventional silicon solar cells since the pioneering work on dye-sensitized nanocrystalline TiO₂ by O'Regan and Grätzel [1]. In these cells, the use of dye molecules as photosensitizers, nanostructured TiO₂ as the electron transport layer, and, the I⁻/I₃⁻ redox couple as a hole transport layer dramatically improve the light-harvesting efficiency. Ru-based dyes attached to mesoporous TiO₂ with large surface areas absorb solar energy efficiently. The electrons injected by the optically excited dye into the TiO₂ conduction band diffuse across the semiconductor film layer and reach the back contact. Redox couples diffusing in solution, which are in turn reduced at the counter electrode, regenerate the oxidized dye. To achieve efficient solar energy conversion as well as long-term photostability, some researchers have applied quantum-dot semiconductors as dye substitutes for sensitizers [2]. The use of semiconductor QDs as sensitizers has several advantages in solar cell applications [3]. Firstly, by controlling their size, the energy gap of the QDs can be tuned to cover a large fraction of the solar spectrum [4]. Secondly, semiconductor QDs have a large extinction coefficient due to quantum confinement and the large intrinsic dipole moment, which can lead to rapid

charge separation [5]. Thirdly, they have the potential for multiple exciton generation (MEG) [6], which can potentially increase the efficiency of photovoltaic devices [7]. As for present photovoltaic devices, there is a maximum thermodynamic energy conversion efficiency of about 31% calculated by the Shockley-Queisser detailed balance limit [8]. When MEG is incorporated into the calculations, the value of the maximum thermodynamic energy conversion efficiency can be pushed up to 44% [9]. Although, the efficiency of quantum dot-sensitized solar cells (QDSSCs) is still lower than DSSCs (the reported maximum conversion efficiency of QDSSCs is ~5% at present), QDSSCs are attracting increasing attention among researchers, and progress is very rapid [10].

There are several factors assist to improve the performance of QDSSC; (1) pore structure of TiO₂ electrode for a higher covering of QDs, (2) a surface passivation of TiO₂ to reduce recombination, and (3) improved counter electrode materials. Also, the TiO₂ electrode morphology is important for achieving reliable assembly [11]. In DSSCs, the working-electrode should have a high surface area to increase the amount of sensitizer loading in order to enhance light harvesting because of the limitation of the dye adsorption on TiO₂ as single monolayer [12]. However, the recombination process is proportional to the surface area of the electrode. The surface area for QDSSCs may not need to be increased by as much as for DSSCs, because the QD has higher extinction coefficient and QDs adsorption shows several layers. A balance between recombination and light harvesting is needed to maximize the sensitized solar cell performance. To address the penetration of both sensitizers and redox couples, an approach using an inverse opal TiO₂ electrode (IO-TiO₂) has been proposed. IO-TiO₂ has a honeycomb structure with large interconnected pores that leads to better infiltration, despite the smaller surface area compared to nanoparticulate electrodes [13]. In addition, it also exhibits a photonic band gap, which depends on the filling fraction of TiO₂ in the inverse opal structure. At the wavelength near the photonic band gap, the group velocity of photons becomes anomalously small. This phenomenon can be understood by

considering the bending of the photon dispersion curve (E vs k) in a periodic dielectric [14]. At wavelengths approaching the photonic band gap, light can be described as a standing wave [15]. The peaks of this standing wave are localized in the high dielectric part of the photonic crystal on the red edge of the photonic band gap, whereas they are localized in the low dielectric part of the photonic crystal on the blue edge. Taking note of the sensitizer in the high dielectric part of photonic crystal, it may be possible to significantly enhance solar energy absorption by adjusting the red edge of the photonic band gap to fit with the absorption of the sensitizers used, particularly for quantum dots that originally have large extinction coefficients.

To date, the SILAR process has been applied to the preparation of CdSe QDs [16]. Among semiconductors, CdSe is well known as a sensitizer for QDSSCs because of its high light harvesting in the visible region. However, deposition of CdSe QDs by the SILAR method on IO-TiO₂ has not yet been reported. In this study, we investigated the effect of the number of SILAR cycles on the photovoltaic properties of CdSe QDs on IO-TiO₂ electrodes. SILAR method was used to adsorb CdSe QDs not only on the IO-TiO₂, but also on a nanoparticulate TiO₂ electrode (NP-TiO₂) for comparison. The photovoltaic properties were characterized with a solar simulator.

In this chapter, CdSe QDs are adsorbed in situ on inverse opal TiO₂. Photosensitization of inverse opal TiO₂ with CdSe QDs is studied by characterizing its photocurrent as well as photovoltaic performances as a function of SILAR cycles.

4.2 Experimental

The preparation method for IO-TiO₂ has been reported in a previous study [17]. Fluorine-doped tin oxide (FTO) coated glass was ultrasonically cleaned in detergent, KOH, distilled water and methanol. A monodisperse polystyrene (PS) latex suspension (474 nm in diameter) was agitated by ultrasound for 30 min to break aggregated particles.

PHOTOVOLTAIC PROPERTIES OF CdSe QD ON TiO₂

The synthetic opal samples were assembled by immersing the FTO substrate vertically in a 0.1 wt.% monodisperse PS suspension and evaporated leaving behind a colloidal crystal film on the substrate. A 10- μ l drop of 2% TiCl₄ in methanol was added to the colloidal surface. After hydrolysis for 30 min, the sample was subsequently heated to 80°C in air. This process was repeated several times to ensure the filling of all voids. Finally, the sample was subsequently heated at 450°C for 1 h in air to calcinate the template and anneal the TiO₂. The IO-TiO₂ thickness was measured as 3 μ m using a contact profilometer (DEKTAK, ULVAC). NP-TiO₂ was fabricated using a method described in a previous report [18]. To fabricate NP-TiO₂, TiO₂ pastes were prepared by mixing 15 nm TiO₂ nanoparticles (Super Titania, Showa Denko, anatase structure) and polyethylene glycol (molecular weight 500 000) in pure water. The prepared pastes were applied onto FTO substrates (10 Ω /sq) using the doctor blade method, followed by sintering at 450 °C for 30 min. The NP-TiO₂ thickness was found to be 3 μ m. In the case of NP-TiO₂ electrode, we chose 15 nm of NP-TiO₂ because previous study in our group found that the size of the TiO₂ was the optimal condition for QDSSC [18]. Then, both conditions were compared.

The CdSe QDs were adsorbed on the TiO₂ electrodes in a nitrogen atmosphere using the SILAR method [16]. The TiO₂ electrode was immersed sequentially into two different solutions for about 30 s each. One solution contained 0.03 M Cd(NO₃)₂ dissolved in ethanol and the other solution consisted of 0.03 M SeO₂ and 0.06 M NaBH₄ in ethanol. Following immersion, the films were rinsed for 1 min using pure ethanol to remove excess precursor, and the electrode was dried before the next dipping. This immersion cycle was repeated several times from 3 to 15 cycles in order to investigate the effect of the number of SILAR cycles. Subsequently, the samples were coated with ZnS to prevent both photocorrosion and recombination processes between electron and hole on the surface. The SILAR method was used for this passivation coating, which was done

by dipping the sample twice each in 0.1 Zn(CH₃COO)₂ and 0.1 M Na₂S for 1 min each dip [19].

The incident photon-to-current conversion efficiency (IPCE) and the photovoltaic measurements were performed in a sandwich structure solar cell with a Cu₂S counter electrode [20]. The polysulfide electrolyte (1 M S and 1 M Na₂S solution) was used as the regenerative redox couple [21]. The active area of the cells was 0.24 cm². Their IPCE spectra were measured under the short circuit photocurrent with the same conditions as those used for the PA measurement. The photocurrent was measured using a zero shuntmeter. The photovoltaic characteristics (short circuit current: J_{sc} ; open circuit voltage: V_{oc} ; fill factor: FF ; photovoltaic conversion efficiency: η) were measured using a solar simulator (Pecell Technologies, Inc.) under one sun illumination (AM 1.5, 100 mW/cm²).

4.3 Results and discussion

Figure 4.1 shows IPCE spectra of CdSe QDs adsorbed on TiO₂ electrodes with different CdSe SILAR cycles, (a) IO-TiO₂ and (b) NP-TiO₂. The photosensitization of CdSe QDs on TiO₂ electrodes in the visible region can be clearly observed. Below 9 SILAR cycles, the IPCE spectra of both IO-TiO₂ and NP-TiO₂ cells are enhanced in low photon energy region because a size of CdSe QDs on TiO₂ grows with increasing SILAR cycle. The maximum IPCE of the IO-TiO₂ cell is 36% at 3.2 eV for 13 SILAR cycles and the maximum IPCE of the NP-TiO₂ cell is 71% at 3.2 eV for 9 SILAR cycles. Probable reasons for the lower IPCE in IO-TiO₂ cell are, (1) a fewer adsorption of Cd²⁺ ions, and (2) smaller surface area. As a result, the CdSe QDs adsorbed on IO-TiO₂ are probably fewer amounts than those on NP-TiO₂. Thus, the IPCE of CdSe QDs on IO-TiO₂ is about a half of those on NP-TiO₂. Over 13 cycles, the IPCE value of IO-TiO₂ cell decreases, although there is a decrease in the number of defects as indicated by Fig. 4.1.

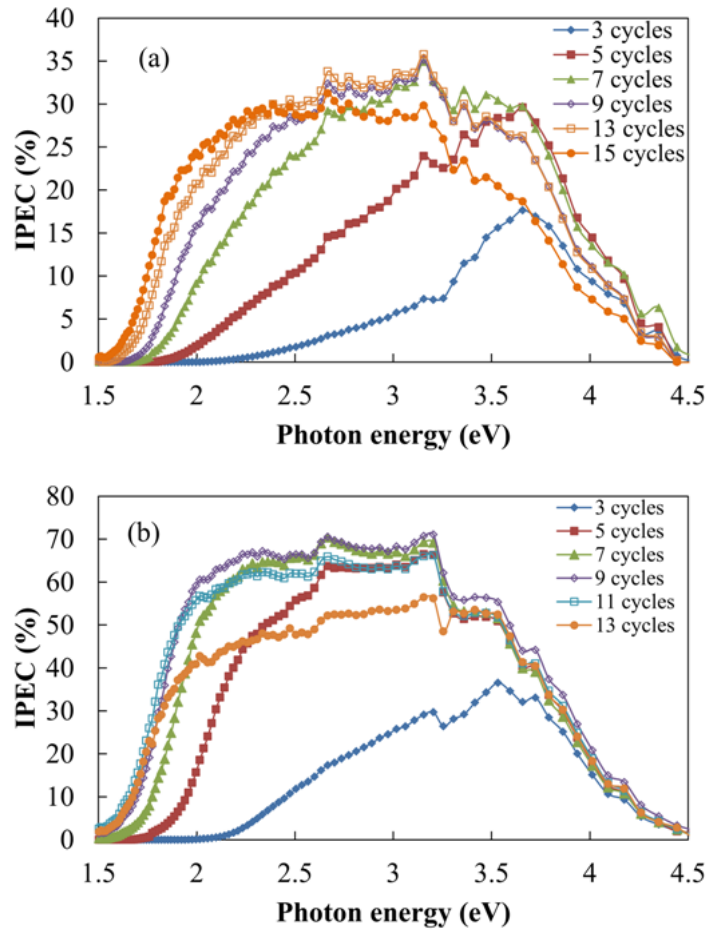
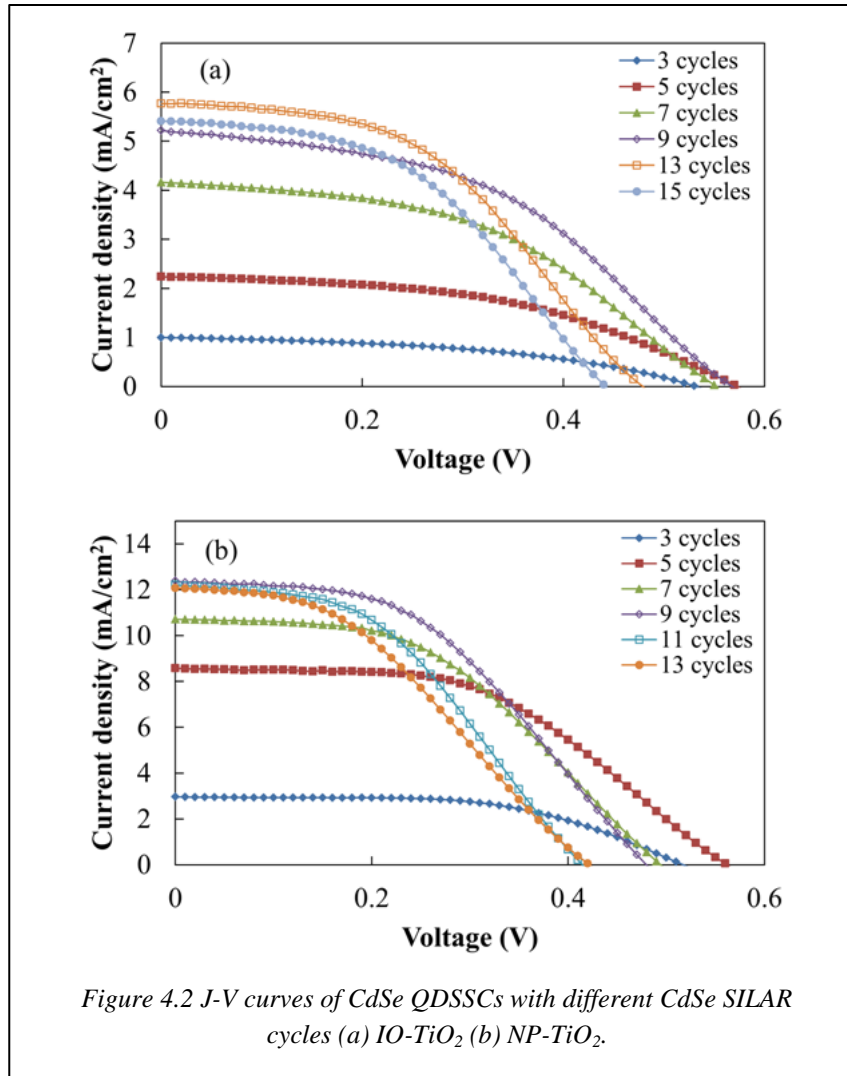


Figure 4.1 IPCE spectra of CdSe QDs adsorbed on IO-TiO₂ (a) and NP-TiO₂ (b) electrodes with different CdSe SILAR cycles.

This may be due to the increased amount of recombination of photoexcited carriers in the increasing interfacial area among the QDs. The recombination mechanism can be the internal recombination at the interface of QDs (e.g., grain boundary recombination), which does not operate for the nearly isolated QDs [22]. The IPCE value of NP-TiO₂ cell decreases when over 9 cycles because the NP-TiO₂ electrode has smaller porous size than the IO-TiO₂ electrode.



The J - V curves of CdSe QDSSCs with a sandwich structure grown for different CdSe SILAR cycles are shown in Fig 4.2. The value of short circuit current (J_{sc}), open circuit voltage (V_{oc}), fill factor (FF), conversion efficiency (η), shunt resistance (R_{sh}), and series resistance (R_s) are summarized in Table 4.1. For IO-TiO₂, J_{sc} attains the maximum value of 5.8 mA/cm² at 13 SILAR cycles and η achieves the maximum value of 1.3% at 9 and 13 SILAR cycles. For NP-TiO₂, J_{sc} and η increase with increasing SILAR cycles, reach the maximum value of 12.4 mA/cm² and 2.7%, respectively at 9 SILAR cycles, and then decrease value with increasing SILAR cycles. These results are different from the case of the CBD method in which J_{sc} of IO-TiO₂ (~9.0 mA/cm²) is similar to NP-TiO₂

PHOTOVOLTAIC PROPERTIES OF CdSe QD ON TiO₂

(~9.3 mA/cm²) and V_{oc} of IO-TiO₂ (~0.71 V) is higher than that of NP-TiO₂ (~0.51 V), as has been reported.⁶ For the SILAR method, the V_{oc} of NP-TiO₂ (~0.57 V) is close to the V_{oc} of IO-TiO₂ (~0.56 V). It is because coverage of growing QDs on TiO₂ surface is a time-dependent function. In this experiment, the SILAR method takes immersion time of 30 seconds that is less than the CBD (~8 hrs). Thus, the CBD has a possibility of more coverage of QDs on TiO₂ surface. Therefore, it is possible that the amount of QDs adsorbed by the CBD is more than SILAR, resulting in higher J_{sc} . The photovoltage in electrochemical QDSSC is limited by the energy difference between the conduction band edge of TiO₂ and the redox potential of polysulfide. The band edge potential can strongly shift as a function of surface pH [23] that relate to a fraction of TiO₂ surface is in direct contact with the electrolyte due to incomplete QD surface coverage. The QDs grown by CBD probably cover more TiO₂ surface than those by the SILAR, resulting higher V_{oc} of QDs on electrode prepared by the CBD. The CBD process tends to block the pores in NP-TiO₂, but IO-TiO₂ has less probability of being blocked pores due to larger voids. The blockages cause electrolyte cannot spread into the voids. The QD surface exposed to the electrolyte is reduced, which results in a limitation of the number of oxidized QDs that can be regenerated by electron capture from the electrolyte. In the case of IO-TiO₂, the voids are larger than those of NP-TiO₂. Accordingly, the electrolyte spreads thoroughly over the large interconnected pores inside IO-TiO₂. The tendency of η is intimately related to J_{sc} and consistent with the IPCE. Lower J_{sc} and η of CdSe QDs on IO-TiO₂ than those on NP-TiO₂ are (1) lower surface area, (2) the lower adsorption of Cd²⁺ ions, and (3) larger amount of surface states.

To further understand these results, J - V parameter analysis was performed using an equivalent circuit model. The equivalent circuit of a solar cell is shown in Figure 4.3. The equivalent circuit mainly considered the photoanode of QDSSC as the electrolyte and the counter electrode were the same for all the samples in the present study.

PHOTOVOLTAIC PROPERTIES OF CdSe QD ON TiO₂

According to Kirchhoff's law, the relation between output current density and voltage can be written as:

$$J = J_{ph} - J_0 \left[\exp \left(q \frac{V + JR_s}{nkT} \right) - 1 \right] - \frac{V + JR_s}{R_{sh}} \quad (4.1)$$

where J and V are the output current density (mA/cm²) and voltage (V), respectively. J_{ph} is the photo current density (mA/cm²). R_s and R_{sh} are series and shunt resistances (kΩ cm²), respectively. J_0 and n are the inverse saturation current density (mA/cm²) and ideality factor of diode D . T is the temperature, k is the Boltzmann constant, and q is the charge of electron. By fitting experimental J - V curves with Equation 4.1, five parameters (i.e., J_{ph} , J_0 , n , R_s and R_{sh}) can be extracted. In order to yield fitting results, an estimation of J - V parameters [24] and a successive large perturbation method [25] were used. J - V curve measurement range was extended below 0 V and to negative values [24]. When the voltage was near 0 V, the diode current density ($J_D = J_0 \left[\exp \left(q \frac{V + JR_s}{nkT} \right) - 1 \right]$) was approximately 0 [24]. Moreover, R_s was usually much smaller than R_{sh} . Thus, Equation 4.1 can be simplified as:

$$J = J_{ph} - \frac{V + JR_s}{R_{sh}} \quad (4.2)$$

$$J = \frac{J_{ph}R_{sh} - V}{R_{sh} + R_s} \approx J_{ph} - \frac{V}{R_{sh}} \quad (4.3)$$

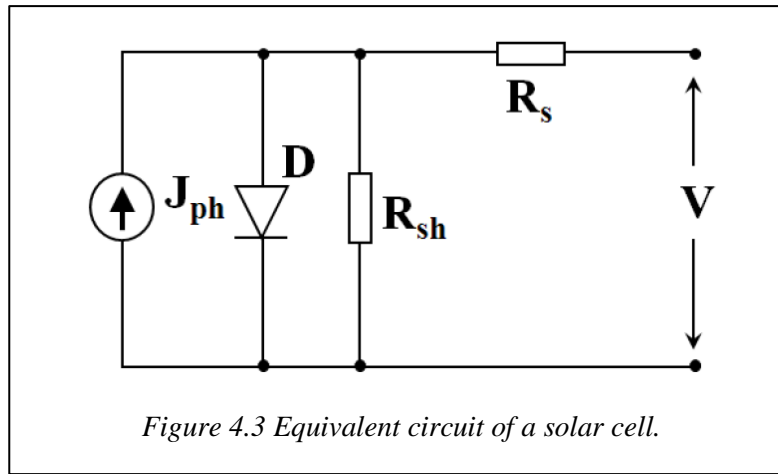
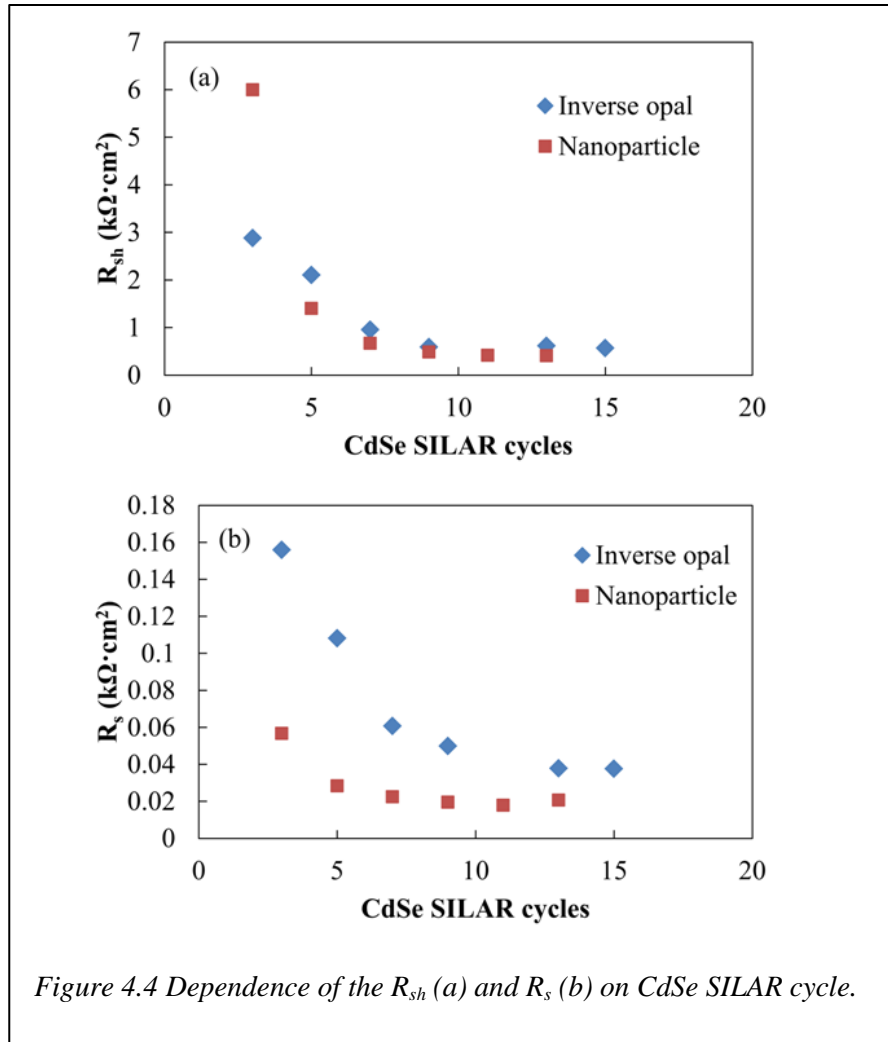


Figure 4.3 Equivalent circuit of a solar cell.

PHOTOVOLTAIC PROPERTIES OF CdSe QD ON TiO₂

It is a linear relationship between J and V . Thus, an estimation of R_{sh} can be obtained by fitting the J - V curve near 0 V (i.e., from the slope) [24]. Similarly, an estimation of R_s can be obtained by fitting the J - V curve near $J = 0$ mA/cm².

The dependence of the R_{sh} (a) and R_s (b) on the CdSe SILAR cycle is shown in Fig. 4.4. R_{sh} and R_s estimated from variations in the slopes of the J - V curve near the short and open circuit conditions, respectively. R_{sh} decreases up to 7 SILAR cycles and then becomes constant for more SILAR cycles. The R_{sh} is the charge transfer resistance of the recombination processes. The charge recombination processes between electrons in CdSe QDs and S_n^{2-} in electrolyte is considerably blocked by the ZnS passivation independently of the CdSe SILAR cycles. Thus, the value of R_{sh} mainly depends on the recombination processes between TiO₂ and QDs, TiO₂ and electrolyte, and among QDs. At 3 SILAR cycles, the R_{sh} of QDs on IO-TiO₂ is lower value than that on NP-TiO₂, thus the IO-TiO₂ has more recombination processes than the NP-TiO₂. As a result, the charge recombination between electrons in the TiO₂ and holes in the CdSe QDs probably occurs. Between 3 and 7 SILAR cycles, the increase in electron injection from the QDs is larger than the increase in recombination between the TiO₂ and the QDs, which causes the values of J_{sc} and η to rise. This observation also suggests that there are the increasing back electron transfer processes between 3 to 7 SILAR cycles both TiO₂ since R_{sh} relates to the back electron transfer across the TiO₂/QDs/electrolyte junction. The value of R_s also decreases up to 7 SILAR cycles and then becomes constant for more SILAR cycles. The R_s is the sum of the sheet resistance of the FTO, the charge transfer resistance at the counter-electrode/electrolyte interface, the redox species diffusion, and the charge transfer resistance in TiO₂ film [26]. In this study, the R_s depends on the charge transfer resistance in TiO₂ film adsorbed with CdSe QDs, and the other resistances are assumed constant for different SILAR cycles. The increasing amount of CdSe QDs on TiO₂ causes the increasing electron injected into TiO₂ then the electron concentration in TiO₂ is boosted, resulting in a decrease of the charge transfer resistance in TiO₂ and R_s . The



increasing number of cycles, it increases the chance of a recombination of carriers increases with the increasing interfacial area among the QDs. The R_s of QDs on IO-TiO₂ is larger than that on NP-TiO₂. A possible reason for the different R_s , the QDs on IO-TiO₂ has fewer amounts than the QDs on NP-TiO₂, which a result in the QDs on IO-TiO₂ has fewer injected electrons than the QDs on NP-TiO₂. As discussed the PA result in chapter 3, the QD surface state per volume on IO-TiO₂ is larger than that on NP-TiO₂, which decreases the electron injection from them to the TiO₂ electrode.

PHOTOVOLTAIC PROPERTIES OF CdSe QD ON TiO₂

Table 4.1. Photovoltaic properties of CdSe QDs adsorbed on TiO₂ electrodes with different CdSe SILAR cycles.

CdSe SILAR cycle	J_{sc} (mA/cm ²)	V_{oc} (V)	FF	η (%)	R_s (k Ω ·cm ²)	R_{sh} (k Ω ·cm ²)
Inverse opal TiO ₂						
3	1.0	0.53	0.45	0.22	0.16	2.8
5	2.2	0.57	0.47	0.60	0.11	2.1
7	4.2	0.55	0.46	1.1	0.061	0.95
9	5.2	0.57	0.45	1.3	0.050	0.59
13	5.8	0.48	0.46	1.3	0.038	0.62
15	5.4	0.44	0.46	1.1	0.038	0.57
Nanoparticulate TiO ₂						
3	3.0	0.52	0.56	0.86	0.057	6.0
5	8.6	0.56	0.50	2.4	0.028	1.4
7	10.7	0.49	0.46	2.5	0.022	0.67
9	12.4	0.48	0.46	2.7	0.019	0.48
11	12.2	0.41	0.44	2.2	0.018	0.42
13	12.1	0.42	0.39	2.0	0.021	0.41

4.4 Conclusions

The maximum photovoltaic conversion efficiency, η_{max} , of CdSe QDs on IO-TiO₂ was 1.3% and the η_{max} of CdSe QDs on NP-TiO₂ was 2.7% at 9 SILAR cycles. Lower J_{sc} and η of CdSe QDs on IO-TiO₂ than those on NP-TiO₂ were the lower adsorption of Cd²⁺ ions, larger amount of surface states per volume, and lower TiO₂ surface area. The shunt resistance, R_{sh} , decreased with the charge recombination

increased. The R_s of QDs on IO-TiO₂ was larger than that on NP-TiO₂ because the QDs on IO-TiO₂ had fewer injected electrons than the QDs on NP-TiO₂.

Reference

- [1] B. O'Regan and M. Gratzel, *Nature* **737**, 353 (1991).
- [2] L. M. Peter, D. J. Riley, E. J. Tull and K. G. V. Wijayanta, *Chem. Commun.* **2002**, 1030 (2002).
- [3] C. H. Chang and Y. L. Lee, *Appl. Phys. Lett.* **91**, 053503 (2007).
- [4] N. Guijarro, Q. Shen, S. Giménez, I. Mora-Seró, J. Bisquert, T. Lana-Villarreal, T. Toyoda and R. Gómez, *J. Phys. Chem. C* **114**, 22352 (2010).
- [5] D. F. Underwood, T. Kippenny and S. J. Rosenthal, *Eur. Phys. J. D* **16**, 241 (2001).
- [6] A. J. Nozik, *Physica E* **14**, 16827 (2002).
- [7] V. I. Klimov, *J. Phys. Chem. B* **110**, 16827 (2006).
- [8] W. Shockley and H. J. Queisser, *J. Appl. Phys.* **32**, 510 (1961).
- [9] M. C. Beard, K. P. Knutsen, P. Yu, J. M. Luther, Q. Song, W. Metzger, R. J. Ellingson and A. J. Nozik, *Nano Lett.* **7**, 2506 (2007).
- [10] V. González-Pedro, X. Xu, I. Mora-Seró and J. Bisquert, *ACS Nano*, vol. 4, p. 5788, 2010.
- [11] T. Toyoda and Q. Shen, *J. Phys. Chem. Lett.* **3**, 1885 (2012).
- [12] M. Grätzel, *J. Photochem. Photobiol. C* **4**, 145 (2003).
- [13] R. R. Somani, C. Dionigi, M. Murgia, D. Palles, P. Nozar and G. Ruani, *Sol. Energy Mater. Sol Cells* **87**, 513 (2005).

PHOTOVOLTAIC PROPERTIES OF CdSe QD ON TiO₂

- [14] K. Sakoda, M. Sasada, T. Fukushima, A. Yamanaka, N. Kawai and K. Inoue, *J. Opt. Soc. Am. B* **16**, 361 (1999).
- [15] S. Nishimura, N. Abrams, B. A. Lewis, L. I. Halaoui, T. E. Mallouk and K. D. Benkstein, *J. Am. Chem. Soc.* **125**, 6306 (2003).
- [16] H. Lee, M. Wang, P. Chen, D. R. Gamelin, S. M. Zakeeruddin, M. Gratzel and M. K. Nazeeruddin, *Nano Lett.* **9**, 4221 (2009).
- [17] L. J. Diguna, M. Murakami, A. Sato, Y. Kumagai, T. Ishihara, N. Kobayashi, Q. Shen and T. Toyoda, *Jpn. J. Appl. Phys.* **45**, 5563 (2006).
- [18] Q. Shen and T. Toyoda, *Thin Solid Films* **167**, 438 (2003).
- [19] S. M. Yang, C. H. Huang, J. Zhai, Z. S. Wang and L. Liang, *J. Mater. Chem.* **12**, 1459 (2002).
- [20] T. Toyoda, K. Oshikane, D. Li, Y. Luo, Q. Meng and Q. Shen, *J. Appl. Phys.* (108), 114340 (2010).
- [21] Q. Niitsoo, S. K. Sarkar, P. Pejoux, S. Rühle, D. Cahen and G. Hodes, *J. Photochem. Photobiol. A* **181**, 306 (2006).
- [22] I. Mora-Seró, S. Giménez, F. Fabregat-Santiago, R. Gómez, Q. Shen, T. Toyoda and J. Bisquert, *Acc. Chem. Res.* **42**, 1848 (2009).
- [23] Z.-S. Wang and G. Zhou, *J. Phys. Chem. C* **113**, 15417 (2009).
- [24] T. Hanmin, Z. Xiaobo, W. Shikui, W. Xiangyan, T. Zhipeng, L. Bin, W. Ying, Y. Tao and Z. Zhigang, *Sol. Energy* **83**, 715 (2009).
- [25] J. Cai, N. Satoh, M. Yanadida and L. Han, *Rev. Sci. Instrum.* **80**, 115111 (2009).
- [26] Q. Wang, S. Ito, M. Grätzel, F. Fabregat-Santiago, I. Mora-Seró, J. Bisquert, T. Bessho and H. Imai, *J. Phys. Chem. B* **110**, 25210 (2006).



Summary

Inverse opal TiO_2 has been successfully synthesized by a simple method. The anatase structured and ordered porous in TiO_2 inverse opal were confirmed by X-ray diffraction pattern and SEM images. CdSe have been successfully adsorbed on inverse opal TiO_2 and nanoparticulate TiO_2 by successive ionic layer adsorption and reaction (SILAR) method confirmed by wall thickening of inverse opal structure in FE-SEM images as increasing SILAR cycle. This CdSe growth has been also caused the red-shift in optical absorption (PA) spectra, where the higher energy of first excitation energy for each SILAR cycle relative to the band gap of bulk CdSe shows the occurrence of quantum confinement effect. The CdSe QD diameter on the electrodes was estimated from the first excitation energy. The growth rates of the QDs on inverse opal TiO_2 and nanoparticulate TiO_2 were similar, indicating that this is independent of morphology. However, measurements of the optical absorbance showed there were more CdSe QDs on nanoparticulate TiO_2 than on inverse opal TiO_2 , indicating that there were a greater number of active sites on nanoparticulate TiO_2 than on inverse opal TiO_2 . The width of the absorption edge, ΔE , of CdSe QDs on inverse opal TiO_2 was higher than that on nanoparticulate TiO_2 , indicating that the CdSe QDs on inverse opal TiO_2 had more disorder than nanoparticulate TiO_2 .

The increased values in incident-photon to current efficiency (IPCE) spectra as increasing SILAR cycle indicates the larger fraction of electron injection from CdSe QDs into TiO_2 conduction band. This result shows the photosensitization of inverse opal TiO_2

SUMMARY

and nanoparticulate TiO₂ with CdSe QDs. The optimum in IPCE value and photovoltaic properties for certain SILAR cycle describes the appropriate condition for electron injection at CdSe/TiO₂ interfaces and hole injection at CdSe/electrolyte interfaces. The latter has been affected by the changing of the porous size in inverse opal TiO₂ as well as nanoparticulate TiO₂ with increasing SILAR cycle (in other word, the penetration of the electrolyte across the matrix). The cause of lower IPCE in inverse opal TiO₂ cell (comparison with nanoparticulate TiO₂) are a fewer adsorption of Cd²⁺ ions, and smaller surface area. As a result, the CdSe QDs adsorbed on inverse opal TiO₂ are probably fewer amounts than those on nanoparticulate TiO₂. Thus, the IPCE of CdSe QDs on inverse opal TiO₂ is about a half of those on nanoparticulate TiO₂.

Inverse opal TiO₂ and nanoparticulate TiO₂ electrodes with CdSe QDs adsorption have been applied in solar application resulting in efficient QD-sensitized solar cells. CdSe QD-sensitized inverse opal TiO₂ has slightly higher open circuit voltage compared to that of nanoparticulate TiO₂ due to its macroporous structure making it potential in sensitized solar cell application. The maximum photovoltaic conversion efficiency, η_{\max} , of CdSe QDs on inverse opal TiO₂ of about 1.3% and the η_{\max} of CdSe QDs on nanoparticulate TiO₂ of about 2.7% have been attained, under solar illumination of 100 mW/cm². In addition, *J-V* parameter analysis was performed using an equivalent circuit model to find shunt resistance and series resistance. The shunt resistance, R_{sh} , decreased with the charge recombination increased. The series resistance, R_{s} , of QDs on inverse opal TiO₂ was larger than that on nanoparticulate TiO₂ because the QDs on inverse opal TiO₂ had fewer injected electrons than the QDs on nanoparticulate TiO₂.

Appendix 1

PbS/CdS quantum dot sensitized solar cell

Quantum dot-sensitized solar cells (QDSCs) are interesting photovoltaic devices because quantum dots (QDs) show some benefits, such as quantum high extinction coefficient, quantum confinement effect and so on [1,2]. Particularly, the multiple exciton generation (MEG) of QD solar cells can theoretically give about 44% of conversion efficiency, higher than Shockley–Queisser efficiency limit [3]. At present, some kinds of QDs have been used to fabricate QDSCs, such as CdS, CdSe and so on. Semiconductor with low bulk band gap, such as PbS with $E_g = 0.41$ eV [4], has received attention since it can allow the absorption band extending to near infrared region of the solar spectrum. Recently, the use of PbS [5] colloidal quantum dots in Schottky solar cells has exhibited the potential of these materials for solar conversion energy, obtaining high photocurrents [5]. However, bulk PbS shows some problems for use as sensitizer; (1) the maximum theoretical efficiency is below 33%, reported for an absorber with a band gap of 0.4 eV [6], (2) the conduction band edge is lower energy level compared to TiO_2 [7], (3) PbS is not stable with redox couples as iodine or polysulfide [8]. The first and second problem can be solved by controlling the PbS QD size where the quantum confinement is reached. The conduction band edge is shifted up, allowing the electron inject to TiO_2 [9]. The instability of PbS in polysulfide can be solved by a CdS coating layer on PbS QDs by successive ionic layer adsorption and reaction method.

In the present study, PbS and CdS QDs have been deposited by the SILAR method onto TiO_2 substrates. Several configurations of PbS and CdS have been

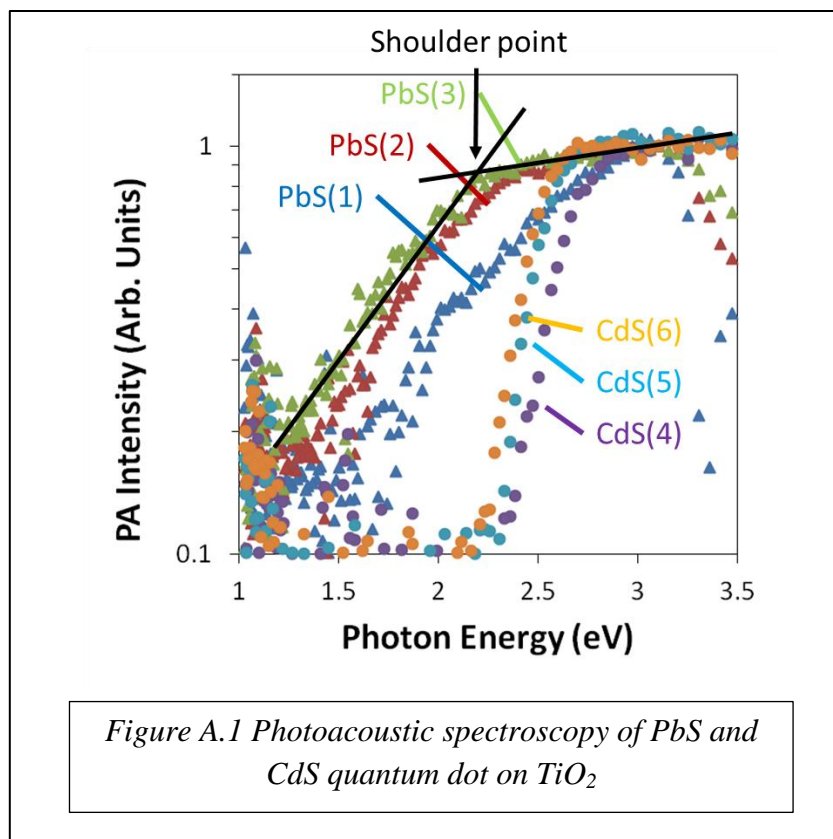


Figure A.1 Photoacoustic spectroscopy of PbS and CdS quantum dot on TiO₂

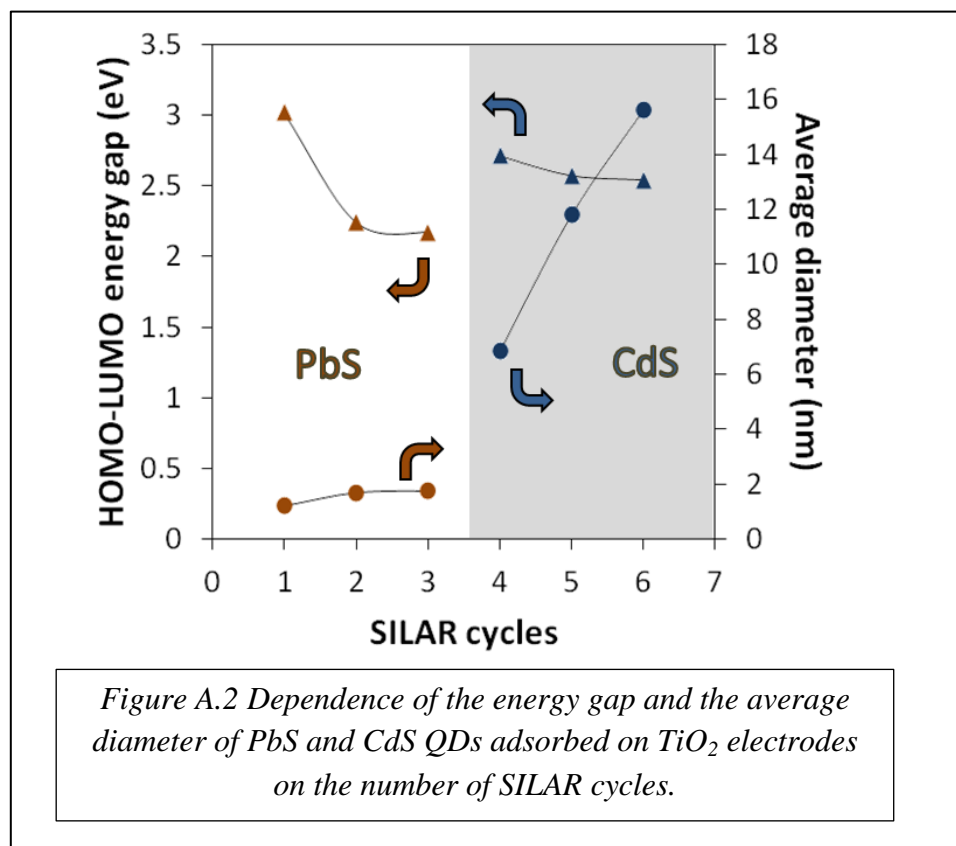
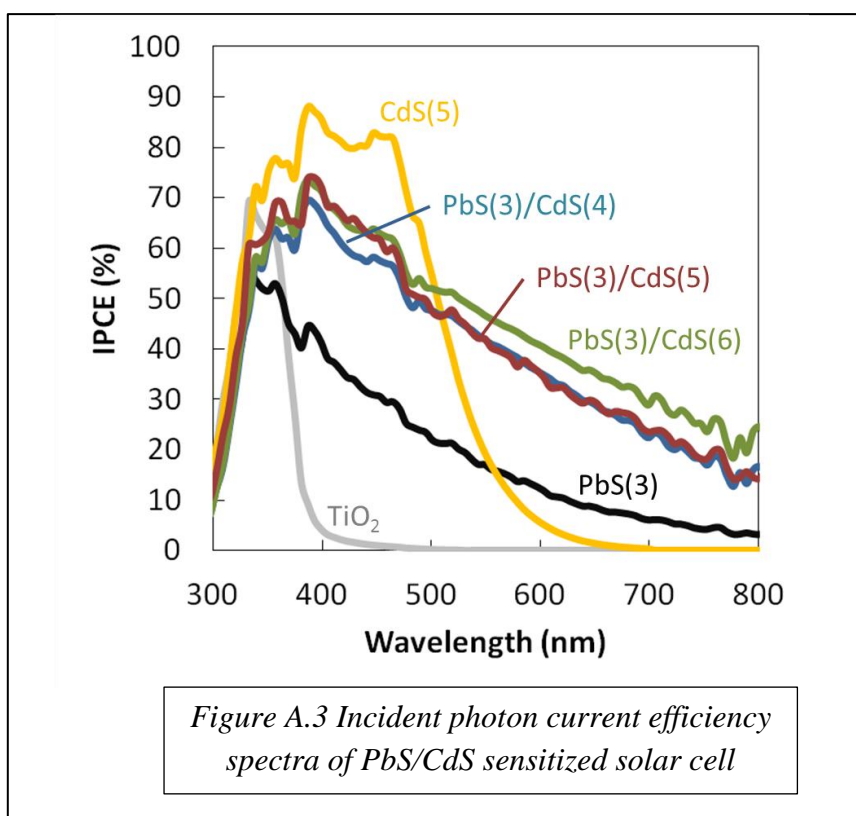


Figure A.2 Dependence of the energy gap and the average diameter of PbS and CdS QDs adsorbed on TiO₂ electrodes on the number of SILAR cycles.

PbS/CdS QUANTUM DOT SENSITIZED SOLAR CELL

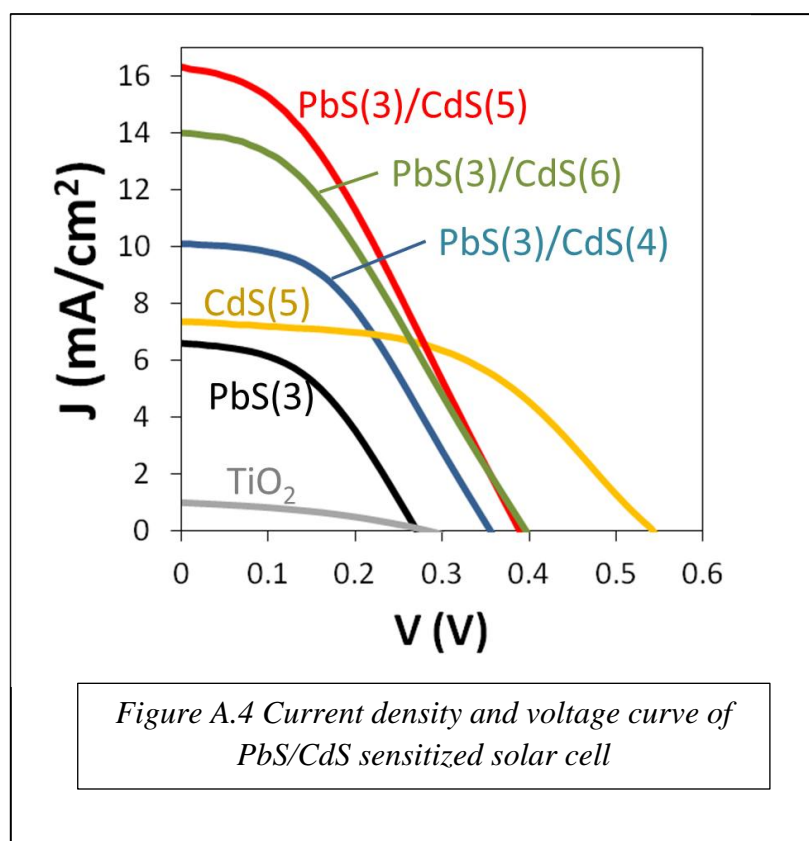
investigated, including only PbS, only CdS, and PbS/CdS system. The samples are labeled as PbS(X)/CdS(Y), where X and Y refer to the numbers of PbS and CdS SILAR cycles, respectively. All samples were coated with ZnS layer by SILAR two cycles.

The effect of the number of SILAR cycles on the optical absorption properties of PbS and CdS QD-sensitized TiO₂ is shown by the photoacoustic spectra (Figure A.1). Increasing of the number of cycles leads to shift of the absorption edge toward lower photon energy. A significant shift (from ~2.5 to ~2.1 eV) is observed for shoulder point of the PbS electrodes, corresponding to samples PbS(1) and PbS(3), respectively. Also, the size of QD is calculated by effective mass approximation method. The QD size increases with the number of SILAR cycles. Enhanced absorption in the NIR region should increase the amount of photocurrent J_{sc} . Consequently, a significant broadening of the IPCE spectrum is observed; see below.



PbS/CdS QUANTUM DOT SENSITIZED SOLAR CELL

The current density-voltage (J-V) curves measured at one sun of illumination are shown in Figure A.4. The photovoltaic properties of the PbS, CdS, and PbS/CdS cells are reported in Figure A.5. PbS(3) and CdS(5) QDSCs reveals low photocurrents. The CdS(5) sample is considered by a high open circuit voltage ($V_{oc} = 0.54$ V). Conversely, the PbS(3) sample presents a very low $V_{oc} = 0.27$ V. In contrast, the co-sensitized sample combining PbS and CdS show an intermediary V_{oc} between those for PbS and CdS QDSCs. Nevertheless, an increase in J_{sc} is observed, conducting to an improvement in efficiency. The photocurrent improvement is due to the broadening of the light absorption region into the red and NIR, as resulting from the IPCE spectra. After investigating the solar cell parameters obtained for the different configurations described in Figure A.5, some characteristic tendency can be revealed. V_{oc} increases with the number of CdS SILAR cycles and decreases with the number of PbS SILAR cycles. The photocurrent

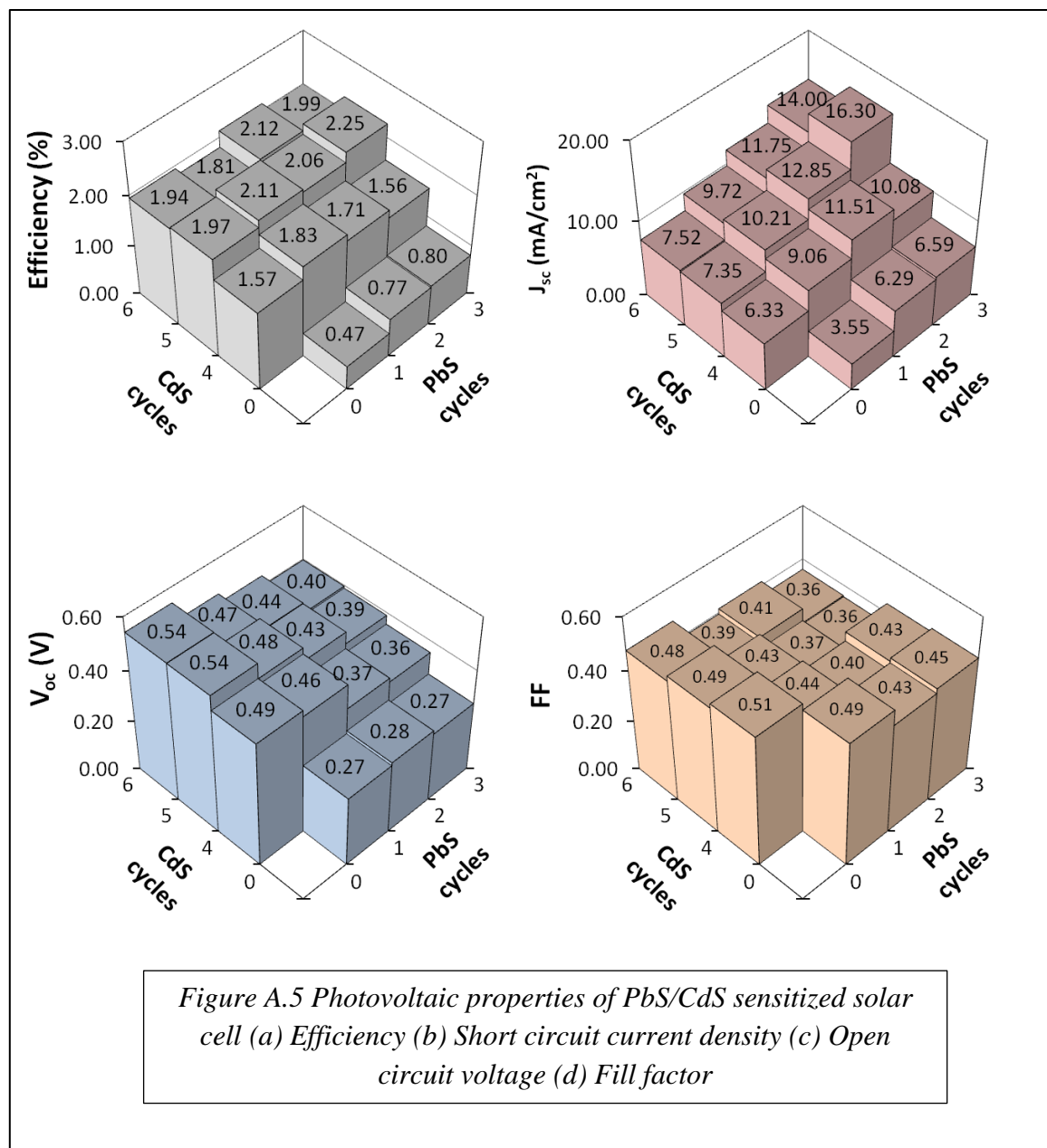


PbS/CdS QUANTUM DOT SENSITIZED SOLAR CELL

remarkably increases for PbS/CdS configuration. Finally, the FF is around 0.4. The slight differences observed in the FF can be ascribed to the different photocurrent. Cells with lower photocurrents exhibit higher FF because the voltage drop in the series resistance is lower.

The efficient QDSCs based on metal sulfide semiconductors. The PbS/CdS configuration has been revealed to improve the solar cell performance further than the efficiencies of the single sensitizer. PbS cell significantly increases the obtained photocurrents with the CdS coating. The strategy of co-absorbers leads to significant development in sensitized solar cell.

PbS/CdS QUANTUM DOT SENSITIZED SOLAR CELL



PbS/CdS QUANTUM DOT SENSITIZED SOLAR CELL

Table A.1. Photovoltaic properties of PbS and CdS QDs adsorbed on TiO₂ electrodes with different SILAR cycles.

PbS SILAR cycles	CdS SILAR cycles	J_{sc} (mA/cm ²)	V_{oc} (V)	FF	η (%)
-	4	6.33	0.49	0.51	1.57
	5	7.35	0.54	0.49	1.97
	6	7.52	0.54	0.48	1.94
1	-	3.55	0.27	0.49	0.47
	4	9.06	0.46	0.44	1.83
	5	10.21	0.48	0.43	2.11
	6	9.72	0.47	0.39	1.81
2	-	6.29	0.28	0.43	0.77
	4	11.51	0.37	0.40	1.71
	5	12.85	0.43	0.37	2.06
	6	11.75	0.44	0.41	2.12
3	-	6.59	0.27	0.45	0.80
	4	10.08	0.36	0.43	1.56
	5	16.30	0.39	0.36	2.25
	6	14.00	0.40	0.36	1.99

References

- [1] A.J. Nozik, *Physica E* **14**, 115 (2002).
- [2] I.J. Kramer, E.H. Sargent, *ACS Nano* **5**, 8506 (2011).
- [3] M.C. Hanna, A.J. Nozik, *J. Appl. Phys.* **100**, 074510 (2011).
- [4] C. Ratanatawanate, C. Xiong, K. Balkus, *ACS Nano* **2**, 1682 (2008).
- [5] J.M. Luther, M. Law, M.C. Beard, Q. Song, M.O. Reese, J.R. Ellingson, A.J. Nozik, *Nano Lett.* **8**, 3488 (2008)
- [6] S.M. Sze, *Physics of Semiconductor devices*, 2nd ed.; John Wiley and Sons: New York, 1981.
- [7] B.R. Hyun, Y.W. Zhong, A.C. Bartnik, L. Sun, H.D. Abruna, F.W. Wise, J.D. Goodreau, J.R. Matthews, T.M. Leslie, N.F. Borrelli, *ACS Nano* **2**, 2206 (2008).
- [8] H. Lee, H.C. Leventis, S.J. Moon, P. Chen, S. Ito, S.A. Haque, T. Torres, F. Nuesch, T. Geiger, S.M. Zakeeruddin, M. Grätzel, M.K. Nazeeruddin, *Adv. Funct. Matter.* **19**, 2735 (2009).
- [9] A.G. Pattantyus-Abraham, I.J. Kramer, A.R. Barkhouse, X. Wang, G. Konstantatos, R. Debnath, L. Levina, I. Raabe, M.K. Nazeeruddin, M. Grätzel, E.H. Sargent, *ACS Nano* **4**, 3374 (2010).

Publications and conference visits

This thesis is based on the following publications:

- *Optical absorption of CdSe quantum dots on electrodes with different morphology, W. Yindeesuk, Q. Shen, S. Hayase and T. Toyoda, AIP Advance* **3**, 102115 (2013).

The work in this thesis was presented at the following international conferences:

- *The 33rd Symposium on Ultrasonic Electronics: 'Photoacoustic characterization of CdSe quantum dots adsorbed on different morphologies of nanostructured TiO₂ for photovoltaic applications'*, November 2012, Japan. Poster presentation.
- *2013 JSAP-MRS Joint Symposia 'Photoacoustic Method Applied to Characterization of CdSe Quantum Dots on Different TiO₂ Morphologies'*, September 2013, Japan. Poster presentation.
- *The 12th Asia Pacific Physics Conference 'Optical Absorption Characterization of CdSe Quantum Dots on Different TiO₂ Morphologies'*, July 2013, Japan. Poster presentation.
- *The 60th Spring Meeting, 2013 'Optical and Photovoltaic Properties of CdSe Quantum Dot Sensitized Solar Cells Prepared with Different Cycles of Successive Ionic Layer Adsorption and Reaction'*, March 2013, Japan. Poster presentation.
- *The International Conference on Photonics Solutions 'Effect of Successive Ionic Layer Adsorption and Reaction Cycle on CdSe Quantum Dot Sensitized Solar Cells'*, May 2013, Thailand. Oral presentation.

Previous publications

- *Observation of optical transition energy in ZnSe/tris(8-hydroxyquinoline) aluminum (Alq₃)/ZnSe single quantum wells by photoreflectance spectroscopy*, J. Nukeaw, K. Upprakhot, S. Rahong, B. Tonhoo and W. Yindeesuk. Physica E **21** (2004) 1070.
- *Electroreflectance and photocurrent measurement of ZnSe/Alq₃/TPD heterostructure on Si-substrate*, W. Pecharapa, A. Keawprajak, N. Kayunkid, S. Rahong, W. Yindeesuk and J. Nukeaw. Mater. Sci. & Eng. B **123** (2005) 163.
- *Growth and Characterization of Novel Optoelectronic Materials Based on II-VI Inorganic/Organic Heterostructures*, W. Pecharapa, A. Keawprajak, N. Kayunkid, S. Rahong, W. Yindeesuk and J. Nukeaw. ScienceAsia **32** (2006) 223.
- *Temperature Dependent Photoluminescence of ZnSe/Alq₃ Hybrid Heterostructure*, W. Pecharapa, P. Potirak and W. Yindeesuk. Advanced Materials Research **55** (2008) 493.

Acknowledgments

I would like to take this opportunity to express my thanks to those who helped me with various aspects of conducting research and the writing of this thesis. First and foremost, Prof. Taro Toyoda for his academic advice and guidance, patience and support throughout the whole research works and the writing of this thesis, and Assoc. Prof. Qing Shen, for her guidance and assistance throughout the course of my doctoral research. She always gave me the freedom to explore interesting new ideas and was there with encouragement and good suggestions. Her kind assistance, patience and help have motivated me greatly.

I wish to express my sincere thanks to all members of Shen's Group for their valuable assistance and insightful discussions. I am particularly grateful for the help from Mr. Daiki Tai, Mr. Masaya Akimoto, and Mr Yu Kuwano. I also wish to thank my remaining group members: Mr. Shingo Miyamoto, Mr. Maeda Naotaka, Mr. Makoto Noguchi, Mr. Osada, Mr. Oshima, Mr. Kuga Yuki, Miss. Tomoka Ota and Miss. Yuki Mori for creating such an enjoyable atmosphere.

Finally, I would like to thank my family. Thanks for your endless support and warmhearted caring. You are always there for me whenever I need you.

Biography

Witoon Yindeesuk was born in Chonburi, Thailand on April 15, 1979. He earned his Bachelor of Science in Applied Physics from King Mongkut's Institute of Technology Ladkrabang, Bangkok, Thailand in March 2002. In 2005, he completed his Masters in Applied Physics from King Mongkut's Institute of Technology Ladkrabang, Bangkok, Thailand. After that, he was a lecturer in Faculty of Science, King Mongkut's Institute of Technology Ladkrabang. In October 2010, he received a scholarship from the Japanese Ministry of Education, Culture, Sports, Science and Technology (MONBUKAGAKUSHO) scholarship. Since then, Mr. Yindeesuk has prepared his Ph.D. thesis under the guidance of Prof. Taro Toyoda and Assoc. Prof. Qing Shen at the Department of Engineering Science, Graduate School of Informatics and Engineering, the University of Electro-Communications.

Mr. Yindeesuk' research interests are material science research, nanoscience and technology including synthesis and characterization. In addition, he is also interested in alternative energy technologies, especially solar energy.